Fakultät für Medizin

Nuklearmedizinische Klinik und Poliklinik

Real-time Investigation of Underlying Physiology behind PET Tracer Uptake based on Positron Imaging of a Microfluidic Chip and a Window Chamber

Zhen Liu

Vollständiger Abdruck der von der Fakultät für Medizin der Technischen Universität München zur Erlangung des akademischen Grades eines

Doctor of Philosophy (Ph.D.)

genehmigten Dissertation.

Vorsitzender: Prof. Dr. Claus Zimmer

Betreuerin: Prof. Dr. Sibylle Ziegler

Prüfer der Dissertation:

1. Prof. Dr. Gabriele Multhoff

2. Prof. Dr. Gil Westmeyer

Die Dissertation wurde am 07.06.2016 bei der Fakultät für Medizin der Technischen Universität München eingereicht und durch die Fakultät für Medizin am 17.08.2016 angenommen.

Real-time Investigation of the Underlying Physiology behind PET Tracer Uptake based on Positron Imaging of a Microfluidic Chip and a Window Chamber

Zhen Liu

München 2016

Abstract

Tumor metabolism and tumor microenvironment are two frontiers of current tumor research. This thesis developed two imaging systems, a continuously infused microfluidic radioassay (CIMR) system and a multimodal intravital molecular imaging (MIMI) system, to imaging tumor cellular metabolism *in vitro* and tumor microenvironment *in vivo*, respectively. Both imaging systems provide high-quality spatiotemporal measurements of radioactive tracers for positron emission tomography (PET), which is achieved using a positron camera based on a single-particle counting silicon pixel detector Timepix with high sensitivity and spatial resolution.

Measuring the cellular pharmacokinetics is difficult. Conventional uptake measurements or microfluidic radioassay systems need to load, unload and purge tracer from the cell culture during the measurements and it is difficult to provide dynamic information. The CIMR system provides a method for continuous in-culture measurement of cellular uptake by simultaneous imaging of a medium chamber and a cell chamber. Medium diluted with a radioactive tracer flows through the medium chamber and cell chamber continuously at a constant low speed. Positrons emitted from the cells and from the tracer in the medium are measured using the positron camera. To test the feasibility of the CIMR system, the influence of glucose concentration on ^{18}F-FDG uptake kinetics was investigated. Human tumor cell lines SkBr3 and Capan-1 were incubated with media of 3 different glucose concentrations and then measured with ^{18}F-FDG on the CIMR system. The relative uptake ratios obtained from CIMR measurements correlated with those from the conventional uptake experiments. The relative standard deviations of relative uptake ratios of CIMR are substantially lower than the conventional uptake experiments. A cellular two compartment model was applied to estimate the cellular pharmacokinetics on CIMR data. The estimated pharmacokinetic parameters were compared to the expressions of glucose transporter-1 (GLUT1) and hexokinase-II (HK2) measured by quantitative real-time polymerase chain reaction (qPCR). For SkBr3, the estimated pharmacokinetic parameters can be fitted with the mRNA expressions using a fixed K_m with the determinant coefficient (R^2=0.73 for $k_1$and R^2=0.97 for k_3). However, for Capan-1, it is not

possible to fit the estimated cellular kinetics with the corresponding mRNA levels using a fixed K_m.

Tumor microenvironment is reflected by several physiological features such as microvasculature, pH, oxygen partial pressure (pO_2), and metabolism. Multimodal molecular imaging with PET and MRI provides advanced *in vivo* methods to capture multiple physiological properties of the tumor microenvironment. However, the interpretation of multimodal imaging to underlying tumor microenvironment is challenging due to the discrepancies between macroscopic and microscopic images of multimodal imaging, as well as *in vivo* and *in vitro* images. The proposed MIMI system provides an advanced platform to bridge these discrepancies and allow multiple in-depth investigations on the same intact tumor tissue. The MIMI system set up a dorsal skin window chamber for a rat tumor model, which is compatible with multimodal imaging and enables co-registration of images with different resolutions. High-resolution positron imaging, magnetic resonance imaging (MRI), fluorescence imaging and luminescence sensor imaging were included in this MIMI system. The fiducial markers of the window chamber were adapted to the multi-imaging modalities and allowed precise physical co-registration of various images. This system offered a tool for the regional investigation and longitudinal observation of underlying physiology in intact tumor tissue.

Zusammenfassung

Der Tumormetabolismus und die Tumormikroumgebung stellen zwei neue Herausforderungen der aktuellen onkologischen Forschung dar. Im Rahmen dieser Doktorarbeit wurden zwei Bildgebungssysteme entwickelt, ein kontinuierlich perfundiertes microfluidisches System zur Messung von Radioaktivität (CIMR) und ein multimodales intravitales Bildgebungssystem zur molekularen Bildgebung (MIMI), um den zellulären Metabolismus in vitro und den Tumormetabolismus in vivo darzustellen. Beide Bildgebungssysteme ermöglichen hochqualitative räumlich-zeitlich aufgelöste Messungen radioaktiver Tracer für die Positronenemissionstomographie (PET) durch eine Positronenkamera, welche auf einem Silikonpartikeldetektor Timepix basiert, der einzelne Partikel mit hoher Sensitivität und räumlicher Auflösung quantifiziert.

Die Messung von zellulärer Pharmakokinetik stellt sich schwierig dar. Konventionelle Aufnahmemessungen bzw. mikrofluidische Radioaktivmessungen müssen beladen, entladen und Tracer aus der Zellkultur entnommen werden. Dynamische Messungen stellen sich in diesem Kontext indes als sehr herausfordernd dar. Das CIMR System ist eine Methode zur kontinuierlichen Messungen der zellulären Aufnahme von Zellen in Kultur durch simultane Bildgebung einer Kammer mit Zellkulturmedium und einer Kammer mit Zellen. Medium, welches mit radioaktivem Tracer versetzt wurde, fließt durch die Kammer mit Zellkulturmedium und die Kammer mit Zellen mit einer konstanten, niedrigen Geschwindigkeit. Positronen, welche von den Zellen und von dem Tracer im Zellkulturmedium emittiert werden, wurden mit der Positronenkamera gemessen. Um die Leistungsfähigkeit des CIMR Systems zu testen, wurde der Einfluss der Glukosekonzentration auf die ^{18}F-FDG-Kinetik untersucht. Die humanen Tumorzelllinien SkBr3 und Capan-1 wurden mit Medium in drei unterschiedlichen Glukosekonzentrationen inkubiert und anschließend mit ^{18}F-FDG im CIMR System gemessen. Das relative Aufnahmeverhältnis, welches aus den CIMR Messungen gewonnen wurde, korrelierte wesentlich mit jenem, welches aus einem konventionellem Aufnahmeexperiment erhoben wurde. Die relativen Standardabweichungen der relativen Aufnahmeverhältnisse der CIMR Messungen sind wesentlich geringer als jene der konventionellen Aufnahmeversuche. Ein zelluläres Zwei-Kompartiment-Modell wurde angewandt, um die zelluläre Pharmakokinetik der CIMR Daten abzuschätzen. Die abgeschätzten pharmakokinetischen Parameter wurden mit den Genexpressionsdaten von Glukosetransportern-1 (GLUT-1) und Hexokinase-II (HK2), welche mittels quantitativer Echt-Zeit-Polymerasekettenreaktionsmessungen (qPCR) erhoben

wurden, verglichen. Die hochqualitativen dynamischen Messungen erlauben die Abschätzung der zellulären Pharmakokinetik mit hoher Sensitivität.

Die Tumormikroumgebung zeichnet sich durch einige physiologische Besonderheiten, wie z.B. Mikovaskularisierung, pH, Sauerstoffpartialdruck (pO_2) und Metabolismus aus. Multimodale Bildgebung mit PET und MRT stellen fortgeschrittene in vivo Methoden dar um mehrere physiologische Eigenschaften der Tumormikroumgebung zu erfassen. Dennoch stellt sich die Interpretation der multimodalen Bildgebung auf Grund der zugrundeliegenden Tumormikroumgebung als Herausforderung dar, basierend auf den Unterschieden zwischen makroskopischen und mikroskopischen Bildern der multimodalen Bildgebung, so wie auch bei in vivo als auch in vitro Bildern. Das vorgestellt MIMI System ist eine fortgeschrittene Plattform, welche es ermöglicht diese Diskrepanz zu überbrücken und multiple, detaillierte Untersuchungen eines gleichen, intakten Tumors erlaubt. Das MIMI System besteht aus einer dorsalen Hautfensterkammer, welche mit multimodaler Bildgebung kompatibel ist und die Ko-Registration von Bildern mit unterschiedlicher Auflösung ermöglicht. Hoch-aufgelöste Positronenbildgebung, Magnetresonanztomographie (MRI), Fluoreszenzbildgebung und Luminiszenzbildgebung wurden in dieses MIMI System integriert. Die Orientierungspunkte der Fensterkammer wurden den Multimodalen Bildgebungsmodalitäten angepasst und ließen eine physikalische präzise Ko-Registrierung verschiedener Bilder zu. Dieses System stellt ein Werkzeug zur regionalen Untersuchung und zur longitudinalen Beobachtung der zugrundeliegenden Physiologie von intaktem Tumorgewebe dar.

Contents

1. Introduction

1.1. Overview of tumor biology

Tumor originally meant any form of swelling, neoplastic or not. Current terminology, however, both medical and non-medical, uses tumor as a synonym of neoplasm [*1*]. Tumor is an abnormal growth of tissue, and can be described as clonally derived (although not exclusively) growing masses of excessively replicating cells with no real mechanism of regulation [*2*]. Generally, a tumor can be sorted as a benign neoplasia or a malignant neoplasia. The latter refers to cancer, which is characterized by uncontrolled cell division and the ability of these cells to invade other tissues, either by a direct growth into adjacent tissues (invasion) or by a migration of cells to distant tissues (metastasis) [*3*]. Tumor progression can be defined with grading, denoting increased lack of differentiation of the tumor cells from grade I to grade IV. The tumor progression can also be classified with tumor stages in clinic, according to the dissemination of the tumor. A tumor stage is decided by the size of a primary tumor, dissemination of lymph node and number of metastasis [*4*].

It is now widely accepted that a tumor is derived from normal cells. The transformation of normal cells into highly malignant derivatives is a multistep process of genetic alterations [*5,6*]. Six hallmarks of alterations in tumor cell physiology was proposed and summarized by Hanahan and Weinberg in 2000: self-sufficiency in growth signals, insensitivity to growth-inhibitory (anti-growth) signals, evasion of programmed cell death (apoptosis), limitless replicative potential, sustained angiogenesis, and tissue invasion and metastasis [*7*]. And two emerging hallmarks were added to this list in 2011: reprogramming of energy metabolism and evading immune destruction [*8*]. Besides the genetic alterations, the dimension of *in vivo* complexity (i.e., tumor microenvironment) draws more attention in these years. Tumors have increasingly been recognized as organs whose complexity approaches and may even exceed that of normal healthy tissues [*8*]. Tumor cells and the non-transformed cell types such as endothelial cells, fibroblasts, and immune cells interact together to form their 'joint tissue', and modulate the tumor microenvironment. It is characterized, inter alia, by oxygen depletion (hypoxia, anoxia), glucose and energy deprivation, high lactate levels, glucose and bicarbonate deprivation, energy impoverishment, significant interstitial fluid flow, etc [*9*]. As the tumor cells co-evolve with their microenvironment, heterogeneity of cancer cells is observed in a single tumor tissue. From this perspective, some of the phenotypic, genetic and epigenetic diversities observed at the cell population level are likely to be natural consequences of tumor-microenvironment interactions [*10,11*]. During the tumorigenesis and progression, several characteristics of the tumor

microenvironment can be profiled: (1) an abnormality of tumor microvessels during angiogenesis; (2) transformed energy metabolism according to the tumor cell proliferation and local microenvironment changes; (3) local pH changes in hypoxic and necrosis region; (4) the occurrence of hypoxic region owing to the imbalance between supply and consumption of oxygen as the tumor grows; (5) evading of immune destruction; (6) heterogeneity of tumor microenvironment.

Angiogenesis plays a significant role during tumor progression [*12*], as it is recognized that no solid tumor can grow beyond size of approximately 1 mm^3 without sufficient vascular supply [*13*]. Tumor angiogenesis develops from an existing vasculature, through endothelial cell sprouting, proliferation, and fusion. Moreover, it is proved that various types of cells also contribute to the process, including endothelial cells [*14*], circulating endothelial precursor cells [*9*], local mesenchymal cells [*14*], tumor cells [*15,16*], and even mononuclear cells [*13*]. However, tumor's microvessels show severe structural and functional abnormality compared to that of normal tissue [*9*]. More specially, tumors express an individual microvascular architecture, which is often dilated, tortuous, elongated, and saccular [*9*]. Parameters defining the microvascular unit, such as intervascular distance, interbranching distances, and branching angles show tumor-type-dependent significant differences as demonstrated [*17*]. The irregularities of tumor microvessels around a tumor are non-homogenous, highly and poorly vascularized areas can be located directly to each other, although the vascular density in central tumor areas is nearly as high as in the surrounding normal tissues [*14*]. Tumor microvasculature significantly influences the tumor physiology as it is crucial for the nutrient and oxygen supply and waste removal, such as oxygenation and glucose metabolism.

During the tumorigenesis and progression, the energy metabolism is adapted toward glycolysis even in the presence of sufficient oxygen, leading to an augmented glucose uptake in tumors. This aerobic glycolysis of the tumor is known as the 'Warburg effect' [*18*], a metabolic pathway that has lower energy generation efficiency than an aerobic respiration. Although the aerobic glycolysis is an inefficient way to generate adenosine 5´-triphosphate (ATP), it is conducive to the fast proliferation of tumor cells in adaption to the vast bio-synthesis needs of carbon bones [*19*]. The increased glycolysis is realized via the overexpression of the glucose transporters (GLUTs) and related enzymes (such as hexokinase), and/or enzyme activities changes. The aerobic glycolysis converts glucose into pyruvate. Then, the majority of the pyruvate turn into the lactate production rather than the oxidative phosphorylation. The lactate accumulates in the tumor and leading to tumor acidity [*20*]. The lactate production and uptake are facilitated by lactate transporters-monocarboxylate cotransporters (MCTs) [*20*]. In several tumor types, the production and utilization of lactate can occur simultaneously in the tumor microenvironment [*21,22*]. The lactate accumulation has been proven to be positively correlated with tumor

progression and metastasis, implicating a poor overall survival of patients [*23,24*]. Tumor metabolism involves complex interactions. It is not only affected by the metabolites, ions, the vascular network and signaling cascades, but also affected by the oxygenation states of the tumor microenvironment [*20*].

Advanced solid tumor is characterized with a lack of oxygen (knows as a hypoxia), where the oxygen partial pressure (pO_2) is lower than the surrounding normal tissues [*25*]. The low oxygen supply arises from the structural and function abnormalities of the tumor micro-vasculature network [*9*]. Although both normal and most tumor cells die due to the impairment in cell proliferation, small population of tumor cells can survive by triggering adaptions in proteome and genome [*26*], and further increase the malignance of the tumor progression. Transcription factor hypoxia induced factor -1 (HIF-1) is a key regulator. HIF-1 regulates more than 100 genes for erythropoiesis, angiogenesis, glucose metabolism switch, cell proliferation and apoptosis, facilitating the adaption and survival of tumor cells in hypoxia condition [*27*]. Immunohistochemical analyses have demonstrated an increased HIF-1α levels with increase of the tumor malignance [*28*]. Hypoxic regions play an active role in tumor malignancy, and have become an independent prognostic factor for poor clinical prognosis [*29*]. Hypoxic tumor tissue displays increased resistance to radiation and drugs [*30,31*], increased invasive clones [*32*], and a very low overall survival rate of the patients with hypoxic tumors [*31*].

Intratumor heterogeneity is observed during tumor progression [*33,34*]. This is mainly due to the local selection pressure of the tumor microenvironment. The local pressure, local pH and pO_2, mainly derive from the vasculature network, and in turn affect tumor cells' metabolism, genome and proteome. Hypoxic regions within tumors contribute to tumor heterogeneity in at least three ways [*35*]. First, the adaption of tumor cells contribute to mutator phenotypes and might enhance tumor evolution to more aggressive phenotypes [*32*]. Second, hypoxic environments can directly regulate the epigenetic state of tumor cells. The anaerobic glycolytic metabolism from hypoxia region generates and exports lactic acid, which in turn acidifies the hypoxic region [*36*]. The low oxygen and low pH pressure in hypoxia region trigger tumor cell cycle arrest and quiescence [*26,36*], thus increasing the phenotypic heterogeneity. Third, the low vascularization of hypoxia regions reduces the local concentrations of drugs, which favors the selection of drug resistant clones [*37*]. Moreover, the heterogeneity is another factor for therapy and drug resistance [*38*].

1.2. Molecular Imaging

1.2.1. Overview of molecular imaging

Molecular imaging originates from the field of nuclear medicine and radio-pharmacy for better understanding the molecules' information inside the living organisms in a noninvasive manner [*39*]. Molecular imaging implies the integration of various imaging techniques, basic cell/molecular biology, chemistry, medicine, pharmacology, medical physics, biomathematics, and bioinformatics into a new imaging paradigm [*40*]. The entire molecular imaging research chain is driven by molecular targets [*41*]. It usually exploits specific molecular probes as well as intrinsic tissue characteristics as the source of image contrast, and enables the visualization of the cellular function and the follow-up of the molecular process in living organisms without disturbing them [*42*].

A typical process of molecular imaging includes [*43*]: (1) finding a molecular target depending on a given biological question; (2) selecting a signal providing molecular probe (probe) or a radiotracer (tracer) to trace the molecular target. The probes or tracers can be small molecules, peptides, aptamers, engineered proteins or even nanoparticles. The relation between the tracer and target could be direct-labeling, analogs, interaction; (3) introducing a probe or tracer into the living subjects (*in vitro* or *in vivo*) and detecting the signal with appropriate imaging modality. The *in vitro* tests provide better understanding of the probe's properties and its interaction with cells. The *in vivo* tests allow imaging the bio-distribution of the probe in both spatial and temporal dimensions, which are useful for pharmacokinetics studies. The administration routes and probe injection masses have to be optimized to achieve the desired signal with a high signal-to-background ratio; (4) processing imaging analysis and applying pharmacokinetic modeling for visualization and quantification. Various algorithms have to be developed for the image reconstruction and model building; (5) exploring and validating the physiological/pathological features underlying the imaging; (6) translating the molecular imaging strategy into the clinical application.

With the development of imaging techniques, a variety of molecular imaging modalities are available, with three prerequisites [*44*]: (1) high sensitivity enough to monitor interactions at a molecular level; (2) sufficiently high spatial resolution to image mouse models of human disease; and (3) available target-specific molecular probes. A thorough summary of the imaging modalities and systems are well reviewed and shown in table 1 (with some modifications) [*40,42,44,45*]. The imaging modalities include positron emission tomography (PET), single photon emission computed tomography (SPECT), fluorescence molecular tomography (FMT),

magnetic resonance imaging (MRI), intravital microscopy (IVM), bioluminescence imaging (BLI), Ultrasound imaging, fluorescence reflectance imaging (FRI), X-ray computed tomography (CT), positron imaging and other emerging new molecular imaging methods. These imaging modalities have differences in spatial and temporal imaging resolution, imaging depth, and imaging agents, and are oriented toward a variety of illnesses.

Table 1.1 Overview of imaging systems [*42,44*]

Technique	**Resolution**	**Depth**	**Time**	**Imaging agents**	**Target***	**Primary animal use**
MR	10-100 μm	No limit	Minutes-hours	Gadolinium, dysprosium, iron oxide particles	A, P, M	Versatile imaging modality with high soft-tissue contrast
CT	50 μm	No limit	Minutes	Iodine	A, P	Lung and bone imaging
Ultrasound	50 μm	Millimeters	Minutes	Microbubbles	A, P	Vascular and interventional imaging
PET	1-2 mm	No limit	Minutes	^{18}F, ^{11}C, ^{15}O	P, M	Versatile imaging modality with many different tracers
SPECT	1-2 mm	No limit	Minutes	^{99m}Tc, ^{111}In chelates	P, M	Commonly used to image labeled antibodies, peptides and so on
FRI	2-3 mm	< 1 cm	Seconds-minutes	Photoproteins (GFP), NIR fluorochromes	P, M	Rapid screening of molecular events in surface-based tumors
FMT	1 mm	< 10 cm	Seconds-minutes	NIR fluorochromes	P, M	Quantitative imaging of targeted or 'smart' fluorochrome reporters in deep tumors
BLI	Several millimeters	Centimeters	Minutes	Luciferins	M	Gene expression, cell and bacterial tracking

IVM	1 µm	< 400 - 800 µm	Seconds-minutes	Photoproteins (GFP), Fluorochromes	P, M	All of the above at higher resolutions but at limited depths and coverage
PI	200-500 µm	< 1 mm	Seconds-minutes	^{18}F, ^{99m}Tc	M	Tumor metabolism and angiogenesis [*46*]

*Primary area that a given imaging modality interrogates: A, anatomical; M, molecular; P, physiological.

BLI, bioluminescence imaging; CT, X-ray computed tomography; FMT, fluorescence-mediated molecular tomography; FRI, fluorescence reflectance imaging; GFP, green fluorescent protein; NIR; near-infrared; MR, magnetic resonance; PET, positron emission tomography; SPECT, single-photon emission computed tomography; IVM, intravital microscopy, PI, Positron imaging.

1.2.2. Positron imaging

The positron is the antiparticle counterpart of the electron, having the same mass as the electron but carries a positive charge. Positron particle was first proposed in theory by Paul Adrien Maurice Dirac [*47*] in 1928, and then proved in experiment by Carl David Anderson [*48*,*49*] in 1932. When a positron collides with an electron, annihilation occurs, producing two photons which are emitted simultaneously in opposite directions (i.e., gamma ray). Based on detection of these pairs of photons emitted indirectly by a positron-emitting radionuclide, PET was developed. PET has a very high sensitivity for a three-dimensional imaging of functional processes in the body with a very small mass amount of tracer, however, the resolution of the imaging is still limited (~1 mm). This is mainly because the gamma ray is detected instead of the direct detection of the positron signal. A much finer resolution may be achieved by using direct positron signal, and the information about beta particles labeled molecules may also be directly imaged. As positrons annihilate once they collide with electrons, positron imaging is mainly applied with a contact imaging method. Conventionally, autoradiography is utilized to detect both the positron and gamma signals via direct contact and exposure to a phosphor film, then reading out the phosphor films. This is applied for *in vitro* imaging of radioactive slides immediately after scarification of the animal with tracer inside. For the quantitative detection of beta particles indirectly, a scintillation solution is added to the tracer and the scintillation is detected. Another indirect way available for detection of the beta particles is based on the phenomenon called Cerenkov radiation, in which the visible light emission generated by a charged particles traveling through an optically transparent material is specially detected [*50*]. Cerenkov radiation also allows *in vivo* optical imaging of positron emitting radiotracers [*51*].

With the development of digital autoradiography [*52*], various digital detectors like position sensitive avalanche photodiode (PSAPD) [*53*], complementary metal oxide semiconductor (CMOS) [*54*] and charged-coupled detector (CCD) with scintillator [*55*] have appeared, making direct detection of positrons possible. Recently, a positron camera with the hybrid silicon pixel device Timepix (CRYTUR, spol. s r.o.) was jointly developed by Crytur, spol. s r. o. and our group. The details of the basic performance for direct positron measurement with this detector were reported in [*56,57*]. The development of the detector provides an alternative way to perform autoradiography, which is based on direct contact imaging [*58*]. Direct contact detection perfectly fits with microfluidics, which minimizes and integrates all the operation and detection on a single microfluidic chip [*59*] (see 1.3.2). The feasibility of this idea has been proved by pioneering studies: For example, Vu et al. [*60*] developed a positron imaging system integrating a beta camera and a microfluidic chip, which is capable of positron imaging of cellular ^{18}F-FDG uptake on a microfluidic chip. Dooraghi et al. [*61*] further developed this detection system using a PSAPD detector. This system called Betabox and is successfully applied in real time metabolism detection and drug screening [*62*].

Not only applied in *in vitro* study, the direct positron imaging is also applicable for *in vivo* imaging, with the aid of a tissue preparation technique called window chamber model (see 1.3.3). A pioneering study was performed by Zhonglin Liu et al. [*46*]. They combined a PSAPD detector with a mouse dorsal skin window chamber model for imaging, which enabled direct positron and electron imaging of tumor microenvironment. In the following, our group also designed a multimodality imaging compatible window chamber system enabling direct positron imaging [*63*].

1.2.3. Intravital imaging

Intravital imaging can reveal cellular responses over time and space and can be conducted under conditions closely approximating those of a natural environment [*64*]. Intravital imaging is mainly denoted as intravital microscopy (IVM), imaging of live animals at microscopic resolution. Since 1800, IVM has been applied as a tool to study the morphology of microvessels and tissues in living animals [*65*]. Nowadays, IVM is largely based on the detection of fluorescence [*66*] and primarily used to study the location, motility, adhesion, and interactions of individual cells in three physical dimensions over time [*64*]. The emergences of optical frequency domain imaging (OFDI) [*67*], phosphorescence lifetime imaging (PLI) [*68*], spinning disk confocal imaging [*69*] and multiphoton (MP) imaging [*70*] open up the field of IVM to imaging in a larger number of channels, at greater depths, for more extended periods of time, over larger tissue areas, and at vastly improved subcellular resolutions [*64*]. For example,

Dewhirst et al. [*71*] applied fluorescence microscopy and PLI on a rat window chamber model for visualize the location and number of arterioles and their pO_2 values, Rofstad et al. [*72*] developed first-pass imaging method with fluorescence video microscopy for studying blood flow in tumors and normal tissues in mouse dorsal window chamber model.

Imaging modalities with larger imaging dimension, like ultrasound [*73*], MRI [*74*], positron imaging [*46*], bioluminescence [*70*] and implantable biosensors [*75*], can also be applied to broaden the scope of the intravital imaging. Furthermore, multi-modalities imaging is applied for intravital imaging. Multimodal imaging with window chamber explored by Gaustad et al. [*74*] disclosed a method of combining dynamic contrast-enhanced MRI (DCE-MRI) with fluorescence microscopy to establish the correlation between DCE-MRI-derived parameters with tumor vascularity. Confocal laser scanning microscopy (CLSM) and DCE-MRI showed complementary information for tumor microvascular structure and permeability study [*76*].

1.3. Linking of molecular imaging and tumor biology

Molecular imaging attempts to characterize and quantify biological processes at the cellular and subcellular level in intact living subjects in non-harmful manner [*77*], and is closely related to the pharmacokinetics. It has not only been widely applied in imaging live subjects to characterize fundamental biological processes [*40*], but also in molecular oncology investigations, including tumor and host response, tumor invasion and metastasis, matrix remodeling and angiogenesis, cell death, clinical detection of epithelial neoplasia and intra-operative imaging [*42*]. However, it is challenging to figure out the underlying physiological/pathological features with molecular images obtained. In general, image acquisition, processing, computation, and *in vitro* immunohistochemical validation have to working together to link the molecular imaging with the underlying tumor physiological features. A common computing platform is therefore the key to assemble and fuse different imaging techniques for screening, detection, characterization (*in vivo* pathology) and real-time treatment of early-stage cancers [*42*].

Molecular imaging uses probes to help image particular targets and pathways [*41*]. A selection of appropriate tracer related to the biology question is crucial, as the entire molecular imaging research chain is driven by molecular targets [*41*]. A tracer, either a direct radiolabeled version of a naturally occurring compound, an analog of a natural compound, or an unique radiolabeled compound, is designed to provide information about a particular physiological function of interest, such as blood flow, a metabolic process, a transport step, a binding process, etc [*43*]. Usually, the naturally occurring compound has a very complex biochemical fate, making the model describing the tissue radioactivity data of a directly radiolabeled compound quite complex.

A well-designed analog can dramatically simplify the modeling and improve the sensitivity of the model to the parameter of interest. An analog is a compound whose chemical properties are slightly different from its natural compound [*43*].

The selection of tracer ^{18}F-FDG (2-deoxy-2-(^{18}F)fluoro-D-glucose) [*78,79*], an analog of glucose, for glycolysis analysis is a typical example. ^{18}F-FDG PET is widely used for *in vivo* tumor imaging based on the increased glycolysis in tumor cells known as Warburg effect [*80,81*]. The uptake of ^{18}F-FDG is considered as a biomarker of tumor malignancy and of prognostic value for therapy management. ^{18}F-FDG has similar transport and glycolysis kinetics to glucose. Both ^{18}F-FDG and glucose enter cells by the same transport enzyme, and can be phosphorylated by the enzyme hexokinase. After being transported into the cells, glucose is phosphorylated into glucose-6-phosphate and further metabolized through the glycolysis pathway, while phosphorylation of ^{18}F-FDG into the ^{18}F-FDG-6-phosphate is trapped in cells and cannot be further metabolized (^{18}F-FDG-6-phosphate is not a substrate for the next enzyme in the glycolytic pathway) [*82*]. When investigating the mechanism of ^{18}F-FDG for tumor diagnosis and therapy response, the uptake of ^{18}F-FDG is usually interpreted with regard to the expression of GLUTs and HKs of the pathway. Among the two families of proteins, glucose transporter-1 (GLUT1) and hexokinase-II (HK2) are mostly investigated [*83-86*]. GLUT1 expression is usually considered to be associated with malignant tumor stages [*87*]. ^{18}F-FDG uptake was shown to be more influenced by GLUT1 than other subtypes of GLUTs in many tumor tissues such as breast cancer [*88*], pancreatic tumor [*84,89*] and cervical cancer [*90*]. HK2 directly mediates glycolysis and promotes tumor growth [*91*] and it has been found to be the predominant isoform of HKs in many tumors [*83,92*]. The overexpression of HK2 has been reported to increase ^{18}F-FDG uptake in cancer cells [*93*]. The overexpression of GLUT1 and HK2 is also related to the tumor proliferation and stages, showing resistance to drug treatment and poor prognosis [*94,95*]. The GLUT1 and HK2 have been employed as therapeutic target for drug development associated with cancer metabolism [*96,97*]. On the other side, the expression of GLUT1 and HK2 varies among different types of cancer cells [*86*] and tumors possess special abilities to adjust the expression of GLUT1 and/or HK2 to maintain their energy supply and homeostasis[*93,98*]. Furthermore, among the two families of proteins, other subtypes of glucose transporter [*84,90,96,99-101*] and hexokinase [*83,91,100*] are also significantly overexpressed in most of tumor tissues. For example, GLUT3 is often overexpressed in brain tumor and lung cancer. GLUT2 is found overexpressed in HCC. GLUT12 is found to be overexpressed in breast cancer. Many studies show that these subtypes are also correlated with the ^{18}F-FDG uptake [*102,103*]. Hence, it is very difficult to investigate the adaption of their functions under various metabolic conditions [*104,105*].

1.3.1. Kinetic modeling

Pharmacokinetics (PK), refers to a time-dependent concentrations of a substance in a living system [*106*]. It describes the absorption, distribution, chemical changes (metabolism) and excretion of a specific drug (such as a radiotracer) and its metabolites after administration into the body [*43*,*107*]. Pharmacodynamics (PD), different from pharmacokinetics, refers to the pharmacological effect of a drug to a living system. It describes the pharmacological effect (e.g., death of tumor cells in response to a chemotherapeutic agent), from a drug concentration on the target site [*108*]. Here the pharmacokinetic modeling is introduced in detail.

Overview of modeling

The purpose of a mathematical model is to define the relationship between the measurable data and the physiological parameters that affect the uptake and metabolism of the tracer [*43*]. A kinetic model describes the bio-distribution and kinetics of the imaging signal measured under suitable imaging conditions, taking into account the radiopharmaceuticals of a particular radiotracer [*43*].

Factors relating to the development of a kinetic model include physics, pharmaceutics, and mathematical assumptions. When an appropriate tracer is applied and suitable imaging conditions are performed, the tissue radioactivity signal is affected by the local tissue physiology (such as perfusion and metabolism) and the input function (the time-course radioactivity in the plasma). As such, a model is applied to describe the relationship between tissue radioactivity and the controlling factors. A model could predict the tissue radioactivity concentration along the time, or more usefully, be used to estimate physiological parameters by inverting its equations. The method to invert the model equations and solve for physiological parameters is called model-based modeling [*43*].

The typical process of modeling can be described as five main steps [*43*]: (1) providing a priori information based on the characteristics of the tracer to specify a complete model; (2) performing initial modeling studies to define an identifiable model; (3) performing validation studies to refine the model, verify its assumptions, and test the accuracy of its estimates; (4) drawing a practical model; (5) further optimizing the practical model and analyzing errors to get a model-based method, which is both practical and reliable, producing accurate physiological measurements.

Depending on the modeling target and the complexity, modeling could be roughly classified into three groups: Stochastic (non-compartmental) models, compartmental models and distributed models. Stochastic models require minimal assumptions concerning the underlying physiology of the tracer's uptake and metabolism [*109*]. There are no specific compartments needed to be

explicated for tracer molecules. Certain physiological parameters, such as volume of distribution and mean transit time could be extracted [*43*]. The compartmental models define some of the details of the underlying physiology, but do not consider concentration gradients [*43*]. Here, compartments are defined as volumes with homogeneous tracer distribution and tracer's kinetics into and out of each compartment are assessed by the models. Compartmental models are especially useful for tracer kinetic analysis in PET imaging, where the time-concentration curve of the tracer in blood and urine is measureable [*43*]. The distributed models are the most complex models, which not only specify the possible physical locations and biochemical forms of the tracer, but also include the concentration gradients within different physiological domains [*43*]. They are mainly used for diffusion [*110*] and capillary-tissue exchange studies [*111*], where the tracer's precise distribution is concerned.

To compromise the complexity of the physiological and limitations of realistic measurement conditions, assumptions have to be properly made. Here, some of the general assumptions or facts for PET tracer models are listed (to note, the assumptions are not always true, and in some cases may be violated) [*112*]. First, modeling generally assumes that tracer levels are appropriate. As the tracer is presented in the tissue at negligible mass concentrations, little or no change in the saturation of relevant enzymes or receptors occurs. Second, the physiological processes and molecular interactions are not influenced by the PET measurement. Third, constant state (steady state) assumption states that the physiological processes and molecular interactions are in a constant state during the PET measurement.

Moreover, the tracer is crucial for establishing a model. Since the kinetic parameters of an analog are still different from the natural compound, the relationship between the radioactive analog and the native compound has to be determined. The relationship between ^{18}F-FDG and glucose is described by the lumped constant [*113-115*]. The uptake and distribution of the tracer are not only affected by the physiological process under study, but also affected by other factors. Take ^{18}F-FDG for example, in an *in vivo* situation, regional radioactivity concentration data along the time is also affected by regional blood flow (perfusion), tracer clearance from blood, tracer metabolism, and regional uptake of any radioactive metabolites.

Compartmental modeling

Kinetic models have been developed in order to simplify the description of the processes during the interaction between a tracer and an organism. Compartmental modeling is the most commonly used method for mathematical describing the uptake, distribution and the clearance of radioactive tracers throughout the body [*116-118*], and gives the best approximation to reality.

Here, compartments are defined via a boundary setting, in which boundary can be either a physical (for example, a cell membrane, a blood vessel wall, brain blood barrier) or chemical state (i.e., bound and unbound receptor) according to the properties of the tracer and the physiological process it involves. These boundaries partition the measured tracer activity concentration in tissue into distinct compartments. The compartments are typically numbered for mathematical notion. In a compartmental model, all molecules of a tracer will be specified at any given time to be in one of many compartments. Besides, the possible transformations of the tracer among the compartments are defined with the model. This fractional rate of changes in tracer concentration among compartments is called rate constants, with the symbol *k*, the units is min^{-1}.

Compartmental modeling has some assumptions for simplification in mathematics (not always true, and under some situations maybe violated) [*43*]. First assumption is called instantaneous mixing assumption, which states that the concentration in different compartments is homogeneous. There are no concentration gradients within a single compartment. Hence, all molecules in a given compartment have equal probability of exchange into other compartments. Second, the underlying physiological processes are in steady state. Last, to generate the equations of a model, the amount of tracer moving from compartment A to compartment B per unit of time must be defined.

In a PET measurement, after the injection of a tracer into the blood stream, both the tissue tracer concentration and the blood concentration are measured over time [*43*]. For a tracer distribution process, the transport and binding rates of the tracer will be determined by the regional concentration differences. In the PET measurement, a region of interest or pixel can be analyzed independently. Thus, the model can be applied to a specific region or pixel to determine local physiological parameters. The physiological interpretation of the source and destination compartments define the meaning of the rate constants for movement of tracer between them. In PET, a two-tissue-compartment model is widely used for ^{18}F-FDG PET measurement analysis [*119*].

1.3.2. Microfluidic radioassay

Microfluidics is the science and technology of systems that process or manipulate small (10^{-9} to 10^{-8} liters) amounts of fluids, using channels with dimensions of tens to hundreds of micrometers [*59*]. Several terms are similar to the microfluidics by different researchers from different fields or/and during the different stages of the development, such as microelectromechanical systems (MEMS) [*120*], micro total analytical systems (μ-TASs) [*121*] and lab-on-a-chip. The microfluidics was originally developed with the needs from the fields of molecular analysis,

biodefence, molecular biology and microelectronics [*59*]. Microfluidics with advantages of low cost for samples and reagents, in-situ and real-time analysis has been widely applied in analytical chemistry, chemical synthesis, cell biology, molecular biology and pharmaceutics. Typically, a microfluidic system composes of a microfluidic chip, a fluids operation component (pump, valves, tubing etc.) and a detecting unit. A microfluidic chip can be made from a variety of materials, such as silicon, Mylar, paper, Teflon, polydimethylsiloxane (PDMS) and polycarbonates. The fabrication methods for a microfluidic chip is developed fast, from early silicon technology which takes months for fabricating one microfluidic chip to an evolutional soft lithography technology with PDMS which takes about one or two days [*122,123*]. Nowadays, a variety of prototypes and commercial microfluidic chips are supplied by many companies [*124-126*]. Inside a microfluidic chip, several components may be involved: microchannel, micro chamber, micro valves and mixers [*127*], microreserviors, microelectrodes, microdetection components, and microports and connectors [*128*].

The fluids in the microchannel have some special characteristics and properties, such as laminar flow, electro-osmotic flow (EOF) [*129*] and optical waveguide [*130*]. A laminar flow works occurs during the mixing of two fluid streams instead of turbulence on a microfluidic channel. Two fluid streams would not mix to each other in the microchannel but flow in parallel, and only the molecular diffusion works for the mixing. The EOF occurring in the microchannel would drive the fluids moving a plug rather than with parabolic-flow profile in macroscopic scale, which is useful for electrophoretic separations of deoxyribonucleic acid (DNA) in microchannel [*131*]. Another specific phenomenon shown in the microchannel is the optical waveguides, which derives a laminar liquid comprising a high index of refraction flowing between two streams of low-index ‘cladding’ in the microchannel [*130*]. This characteristic enables a new detection methods for refraction waveguides detection based on the microfluidics [*132*].

Microfluidics is a minimized technique, so that a variety of detection methods can be integrated for detection. The detection methods in microfluidics are mainly classified into two types: optical methods and electrochemical methods. In detail, optical methods include absorbance detection, fluorescence detection, chemiluminescence and bioluminescence detection, Raman spectroscopy detection, refractive index detection, thermal lens microscopy detection, and surface plasmon resonance detection [*133*]. Electrochemical methods [*134*] include amperometry, potentiometry, conductometry and electric impedance [*135,136*]. Other detection methods, such as mass spectrometry, magnetic resonance spectroscopy, and acoustical methods, are also available. There is a huge amount of insightful review papers every year, showing that radiometric detection has not been studied much.

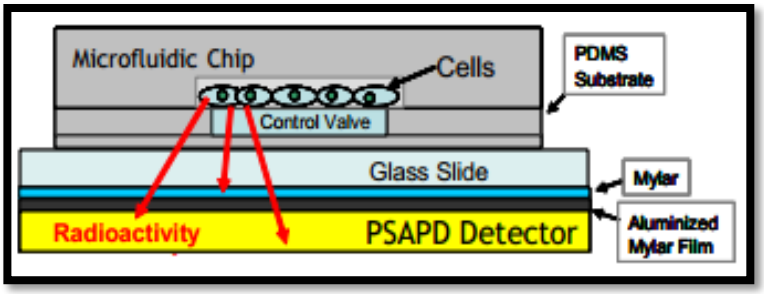

Figure 1.1 Schematic diagram of the cross section of a typical microfluidic chip and the PSAPD detector. Image reprinted from Vu et al. [*137*]

With the development of small planar radiometric detectors like PSAPD [*53,137*] and Medipix2 silicon pixel detector [*54*], radiometric detection in connection with microfluidic was become available. The minimized radiometric detection shows some advantages in applications like kinase activity radioassay [*138*], imaging of the glycolysis in cells [*60,139*] and drug intervention study [*62*]. In general, microfluidic chip based radiometric imaging systems could be termed as micro radioassay system [*60*] or Betabox [*61*]. Typically, the system contains a microfluidic chip, a syringe pump and a radiometric imaging detector. As the detector is located directly beneath the microfluidic chip, the micro radioassay of cells are detected *in situ* (see Figure 1.1). Vu et al.[*60*] applied ^{18}F-FDG to imaging the glycolysis in 4 different melanoma cells lines on chip, supplying a new way to perform conventional well-type ^{18}F-FDG uptake with on-chip cell culture detection. Advantages are smaller cell population (hundreds) and parallel samples detected in the same batch time. In parallel, kinetic modeling experiments were performed and kinetic strategies of positron imaging were studied [*139*]. And this system was further advanced via better microfluidic chip design for metabolic response study with drug intervention [*62*]. In these applications, the pooled radioactivity is removed via washing steps, and imaging of the cells is performed after the wash steps, such that only the retention radioactivity inside the cells is detected. Fang et al. applied a solid-state beta-particle camera imbedded directly below the microfluidic device for real-time quantitative detection of the signal from a kinase activity radioassay [*138*]. This method was an adaption of the conventional kinase activity radioassay, with an obvious reduction of the chemical agent and radioactivity costs, and much less sample requirement. Only thousands of cells were needed for on chip cell culture and for the whole micro radioassay, while the traditional test tube-based needed cell number of 10^7.

1.3.3. Window chamber

Window chamber is an effective tissue observation apparatus for intravital imaging [*140*]. It sets up observable tissue microenvironment between or behind a fixed transparent window on an

intact animal, providing a window into the underlying tissue, which enables in-depth longitudinal observation of tissue physiologies. The development of the tissue can therefore be monitored over the course of several days to weeks within a realistic *in vivo* model with proper imaging techniques. First reported in 1928 by Sandison [*141*], the window chamber originally was utilized to investigate angiogenesis in the normal environment of a rabbit's ear. In 1939, window chambers were first reported in the context of investigating cancer by Ide et al. [*142*]. Since then, various chambers have been developed and implanted with the aim to investigate microcirculation [*143*], angiogenesis [*144*], hypoxia [*72,145*], molecular dynamics [*68,71,146*] and therapeutic interactions [*147*]. Based on tissue preparations, window chamber can be generally classified into two categories: acute window chamber and chronic window chamber. Acute window chamber, including hamster cheek pouch, mesentery, liver or pancreas chamber, allows the observation of orthotopic tumors. However, it does not support repeated or long-term observations. Chronic window chamber allows continuous noninvasive, long-term monitoring of tissue pathologies. Typical examples are ear chamber, dorsal skinfold chamber, percutaneous one-sided window chamber [*148*], abdomen window chamber, cranial chamber [*143*], hamster-cheek-pouch-window and spine cord chamber.

The dorsal skinfold window chamber has been most commonly used to investigate basic cancer biology and tumor development in rodent models. This technique involves surgically implanting a pair of window plates to support a transparent window. The dorsal skin of a mouse is folded up into the frame, and one side of the skin is removed in a circular region of ~ 1 cm in diameter. Furthermore, a round coverslip is placed over the opening, thereby enabling imaging. During window implantation, tumor cells (typically 3-10 mm in diameter and 100-500 µm thick [*68,140*]) can be injected into the underlying skin tissue. Over the course of several days, the tumor will grow in the window, enabling longitudinal imaging of tumor initiation and growth. Quantitative image analysis can then be used to quantify the presence of reporter genes, optical probes, hemodynamics and other parameters in both normal and tumor tissue. There are also some disadvantages of this technique that are important to be considered. In particular, the dorsal window chamber requires a tumor to grow subcutaneously rather than orthotopically. The window chamber is also confined such that tumors cannot grow larger than approximately 7-8 mm in diameter without overgrowing the window chamber. Moreover, the window cannot be maintained for longer than ~2 weeks before either the tumor grows too large or the window begins to deteriorate. However, this technique is uniquely suited for applications requiring longitudinal, high-resolution imaging of dynamic processes. *In vivo* tissue morphological and metabolic characteristics can be obtained from intravital imaging on window chamber in the studies about tissue pathologies, such as tumor hypoxia [*149*], tumor cell-induced angiogenesis [*150*], impact of longitudinal oxygen gradients on tumor hypoxia [*68*], molecular dynamics

[*151*], dynamic interaction of biomaterials with their surrounding host tissue [*152*] and therapeutic activity of anticancer drug [*153*].

1.4. Goals of the study and overview of this thesis

1.4.1. Goals of the study

Objective 1: Develop and establish a microfluidic radioassay system for real-time investigation of PET tracer pharmacokinetic in tumor cells.

To investigate the physiological interaction of the PET tracer with cells is valuable for the interpretation of molecular imaging and for the characterization of the specific PET tracer and pharmaceuticals.
Typically, the investigation of cellular tracer uptake is based on the discontinuous measurements at specific time intervals [*154*]. Although the uptake is essentially a kinetic and continuous process, it is impossible to obtain the real time tracer uptake profile with this method. Recently, a portable *in vitro* molecular imaging system called micro radioassay or Beta-Box [*60-62*] was developed, which integrated a β-particle imaging camera with a microchip, and provided a potential way to monitor cellular uptake process in real time, as the detector could monitor cells *in situ*. However, to minimize background noise due to residual tracer in the extracellular solution, a washing step is necessary for this system. The imaging was performed only after washing just like the typical method. The information about tracer uptake is therefore also "static".
The first aim of this thesis is to develop and establish a microfluidic radioassay system named continuously infused microfluidic radioassay system for real-time investigation of PET tracer pharmacokinetic on tumor cells.

Objective 2: Develop and establish a multimodal intravital molecular imaging system to explore tracer uptake of tumor in vivo
Living organisms are extremely complex functional systems. This complexity is a great barrier to the identification of interactions between tracers and the exploration of their biological functions. Multimodality imaging has become an attractive strategy for in vivo studies to harness the strengths of different imaging methods. Window chamber models sets up observable tissue microenvironment between or behind a fixed transparent window on an intact animal, which enables in-depth observation of tissue physiologies.

The second aim of this thesis is to develop and establish a high-resolution multimodal intravital imaging system based on dorsal skin window chamber tumor model.

1.4.2. Overview of this thesis

The thesis is organized in 8 chapters.

Chapter 1 gives an overview of tumor biology, molecular imaging, and the linking of these two subjects by briefly introducing the basics of techniques and the state of the art of the methodologies. It is a background knowledge preparation for the introduction of this thesis. The aim of the study is addressed in the last section.

Chapter 2, 3 and 4 present a continuously infused microfluidic radioassay (CIMR) system that enables positron imaging of cellular tracer uptake in real time. Chapter 2, 3 and 4 introduce the materials and methods, results and discussion separately. In this system, constantly infused PET tracer medium flows over a reference micro-chamber and a micro-chamber with attached cells simultaneously; Positron imaging of both micro-chambers is monitored in real time. With extraction of real-time radioactivity signal of tracer medium and integrated signal with cells, the cellular real time tracer kinetics was extracted. PET tracer ^{18}F-FDG was applied for establishment and validation of the method. The system detection ability was validated with the comparison of conventional tracer uptake experiment. Furthermore, the cellular ^{18}F-FDG uptake kinetics was assessed with an adapted cellular two compartmental modeling. For an initial validation, the kinetic modeling parameters denoting the ^{18}F-FDG uptake related transporters and enzymes were compared with the messenger ribonucleic acid (mRNA) expression of the correlated GLUT1 and enzyme of HK2.

Chapter 5, 6, 7 present a multimodal intravital molecular imaging (MIMI) system based on a multimodal compatible dorsal skin window chamber tumor model. Chapter 5, 6 and 7 introduce the materials and methods, results and discussion separately.
First, a dorsal skin window chamber with fiducial markers was designed and fabricated, which adapts to several imaging modalities including positron camera, MRI, fluorescence imaging and mini optical sensor. Second, a rat dorsal skin tumor model was established via window chamber implantation and tumor transplantation into the window area. Third, imaging protocol for each imaging modality was established, considering of co-registration among different imaging modalities. Several adapting tools enabling mounting to the multimodal window chamber were developed to aid co-registration among different imaging modalities. Co-registration of imaging from different imaging modalities was successfully attained. Last, the physiological feature

related to the PET tracer imaging on the tumor microenvironment was explored with this system, and the initial study proved the feasibility of the system.

Chapter 8 addresses the innovation of the two imaging systems and methods, summarises the major development and contributions of this thesis.

1. https://en.wikipedia.org/wiki/Neoplasm#cite_note-titlePancreas_Cancer:_Glossary_of_Terms-9.
2. Willis RA. *Pathology of tumours*: Butterworth & Co. (Publishers) Ltd 1968.
3. Bignold LP. Chapter 2 - Theories and Definitions of Tumors. *Principles of Tumors*. Boston: Academic Press; 2015:33-62.
4. Bignold LP. Chapter 3 - Incidences, Mortality, and Classifications of Tumors. *Principles of Tumors*. Boston: Academic Press; 2015:63-88.
5. Balmain A, Barrett JC, Moses H, Renan MJ. How many mutations are required for tumorigenesis? implications from human cancer data. *Mol Carcinog.* 1993;7:139-146.
6. Yokota J. Tumor progression and metastasis. *Carcinogenesis.* 2000;21:497-503.
7. Hanahan D, Weinberg RA. The Hallmarks of Cancer. *Cell.* 2000;100:57-70.
8. Hanahan D, Weinberg Robert A. Hallmarks of Cancer: The Next Generation. *Cell.* 2011;144:646-674.
9. Vaupel P. Tumor microenvironmental physiology and its implications for radiation oncology. *Semin Radiat Oncol.* 2004;14:198-206.
10. Merlo LMF, Pepper JW, Reid BJ, Maley CC. Cancer as an evolutionary and ecological process. *Nat Rev Cancer.* 2006;6:924-935.
11. Polyak K, Haviv I, Campbell IG. Co-evolution of tumor cells and their microenvironment. *Trends Genet.* 2009;25:30-38.
12. Risau W. Mechanisms of angiogenesis. *Nature.* 1997;386:671-674.
13. Folkman J. Tumor angiogenesis. *Adv Cancer Res.* 1985;43:175-203.
14. Molls M, Vaupel P, Brown JM. *Blood Perfusion and Microenvironment of Human Tumors: Implications for Clinical Radiooncology*: Springer; 1998.
15. Sivridis E, Giatromanolaki A, Koukourakis MI. The vascular network of tumours--what is it not for? *J Pathol.* 2003;201:173-180.
16. Ribatti D, Vacca A, Dammacco F. New non-angiogenesis dependent pathways for tumour growth. *Eur J Cancer.* 2003;39:1835-1841.
17. Malkusch W, Konerding MA, Klapthor B, Bruch J. A simple and accurate method for 3-D measurements in microcorrosion casts illustrated with tumour vascularization. *Anal Cell Pathol.* 1995;9:69-81.
18. Warburg O. On the origin of cancer cells. *Science.* 1956;123:309-314.
19. Vander Heiden MG, Cantley LC, Thompson CB. Understanding the Warburg Effect: The Metabolic Requirements of Cell Proliferation. *Science.* 2009;324:1029-1033.
20. Kennedy KM, Dewhirst MW. Tumor metabolism of lactate: the influence and therapeutic potential for MCT and CD147 regulation. *Future Oncol.* 2010;6:127-148.
21. Wang Q, Morris ME. The role of monocarboxylate transporter 2 and 4 in the transport of gamma-hydroxybutyric acid in mammalian cells. *Drug Metab Dispos.* 2007;35:1393-1399.
22. Sonveaux P, Vegran F, Schroeder T, et al. Targeting lactate-fueled respiration selectively kills hypoxic tumor cells in mice. *J Clin Invest.* 2008;118:3930-3942.
23. Walenta S, Mueller-Klieser WF. Lactate: mirror and motor of tumor malignancy. *Semin Radiat Oncol.* 2004;14:267-274.
24. Schwickert G, Walenta S, Sundfor K, Rofstad EK, Mueller-Klieser W. Correlation of high lactate levels in human cervical cancer with incidence of metastasis. *Cancer Res.* 1995;55:4757-4759.
25. Carreau A, El Hafny-Rahbi B, Matejuk A, Grillon C, Kieda C. Why is the partial oxygen pressure of human tissues a crucial parameter? Small molecules and hypoxia. *J Cell Mol Med.* 2011;15:1239-1253.
26. Vaupel P, Mayer A, Höckel M. Tumor Hypoxia and Malignant Progression. *Methods Enzymol.* 2004;381:335-354.
27. Ke Q, Costa M. Hypoxia-inducible factor-1 (HIF-1). *Mol Pharmacol.* 2006;70:1469-1480.
28. Semenza GL. Targeting HIF-1 for cancer therapy. *Nat Rev Cancer.* 2003;3:721-732.

29. Vaupel P, Mayer A. Hypoxia in cancer: significance and impact on clinical outcome. *Cancer Metastasis Rev.* 2007;26:225-239.
30. Rofstad EK, Sundfør K, Lyng H, Tropé CG. Hypoxia-induced treatment failure in advanced squamous cell carcinoma of the uterine cervix is primarily due to hypoxia-induced radiation resistance rather than hypoxia-induced metastasis. *Brit J Cancer.* 2000;83:354-359.
31. Kim JJ, Tannock IF. Repopulation of cancer cells during therapy: an important cause of treatment failure. *Nat Rev Cancer.* 2005;5:516-525.
32. Lunt S, Chaudary N, Hill R. The tumor microenvironment and metastatic disease. *Clin Exp Metastas.* 2009;26:19-34.
33. Tixier F, Hatt M, Valla C, et al. Visual versus quantitative assessment of intratumor 18F-FDG PET uptake heterogeneity: prognostic value in non-small cell lung cancer. *J Nucl Med.* 2014;55:1235-1241.
34. Tixier F, Le Rest CC, Hatt M, et al. Intratumor Heterogeneity Characterized by Textural Features on Baseline 18F-FDG PET Images Predicts Response to Concomitant Radiochemotherapy in Esophageal Cancer. *J Nucl Med.* 2011.
35. Tian T, Olson S, Whitacre JM, Harding A. The origins of cancer robustness and evolvability. *Integr Biol* 2011;3:17-30.
36. Gatenby RA, Gillies RJ. Why do cancers have high aerobic glycolysis? *Nat Rev Cancer.* 2004;4:891-899.
37. Dalton WS, Durie BGM, Alberts DS, Gerlach JH, Cress AE. Characterization of a New Drug-resistant Human Myeloma Cell Line That Expresses P-Glycoprotein. *Cancer Res.* 1986;46:5125-5130.
38. Junttila MR, de Sauvage FJ. Influence of tumour micro-environment heterogeneity on therapeutic response. *Nature.* 2013;501:346-354.
39. Sanjiv Sam G. Molecular imaging of cancer with positron emission tomography. *Nat Rev Cancer.* 2002;2:683-693.
40. Massoud TF, Gambhir SS. Molecular imaging in living subjects: seeing fundamental biological processes in a new light. *Genes Dev.* 2003;17:545-580.
41. Weissleder R, Gambhir SS. *Molecular imaging: principles and practice*: PMPH-USA; 2010.
42. Weissleder R, Pittet MJ. Imaging in the era of molecular oncology. *Nature.* 2008;452:580-589.
43. Bailey DL, Townsend DW, Valk PE, Maisey MN. *Positron emission tomography*: Springer; 2005.
44. Rudin M, Weissleder R. Molecular imaging in drug discovery and development. *Nat Rev Drug Discov.* 2003;2:123-131.
45. Weissleder R. Scaling down imaging: molecular mapping of cancer in mice. *Nat Rev Cancer.* 2002;2:11-18.
46. Liu Z, Chen L, Barber C, et al. Direct positron and electron imaging of tumor metabolism and angiogenesis in a mouse window chamber model. *JNM Meeting Abstracts.* 2012;53:1146.
47. Dirac PAM. The Quantum Theory of the Electron. *Proc R Soc A.* 1928;117:610-624.
48. Anderson CD. The apparent existence of easily deflectable positives. *Science.* 1932;76:238-239.
49. Anderson CD. The Positive Electron. *Phys Rev.* 1933;43:491-494.
50. Jennifer SC, Richard T, Sebastian O, et al. Cerenkov radiation imaging as a method for quantitative measurements of beta particles in a microfluidic chip. *Phys Med Biol.* 2009;54:6757.
51. Antonello ES, Daniela DA, Laura C, Mario M, Andrea S, Federico B. Cerenkov radiation allows *in vivo* optical imaging of positron emitting radiotracers. *Phys Med Biol.* 2010;55:483.
52. Bertolucci E, Conti M, Mettivier G, Montesi MC, Russo P. BETAview: a digital β-imaging system for dynamic studies of biological phenomena. *Nucl Instr Meth Phys Res A.* 2002;478:109-113.
53. Vu NT, Chung YH, Yu ZTF, et al. Direct Detection of Beta Particles on a Microfluidic Chip using Position Sensitive APDs. Paper presented at: Nuclear Science Symposium Conference Record, 2006. IEEE; Oct. 29 2006-Nov. 1 2006, 2006.
54. Lauria A, Mettivier G, Montesi MC, et al. Experimental study for an intraoperative probe for 18F imaging with a silicon pixel detector. *Nucl Instr Meth Phys Res A.* 2007;576:198-203.

55. Chen L, Gobar LS, Knowles NG, Liu Z, Gmitro AF, Barrett HH. Direct Imaging of Radionuclide-Produced Electrons and Positrons with an Ultrathin Phosphor. *J Nucl Med.* 2008;49:1141-1145.
56. Wang Q, Tous J, Liu Z, Ziegler S, Shi K. Evaluation of Timepix silicon detector for the detection of 18F positrons. *J Instrument.* 2014;9:C05067.
57. Wang Q, Liu Z, Ziegler SI, Shi K. Enhancing spatial resolution of (18)F positron imaging with the Timepix detector by classification of primary fired pixels using support vector machine. *Phys Med Biol.* 2015;60:5261-5278.
58. Russo P, Lauria A, Mettivier G, et al. 18 F-FDG positron autoradiography with a particle counting silicon pixel detector. *Phys Med Biol.* 2008;53:6227.
59. Whitesides GM. The origins and the future of microfluidics. *Nature.* 2006;442:368-373.
60. Vu NT, Yu ZTF, Comin-Anduix B, et al. A β-Camera Integrated with a Microfluidic Chip for Radioassays Based on Real-Time Imaging of Glycolysis in Small Cell Populations. *J Nucl Med.* 2011;52:815-821.
61. Dooraghi AA, Vu NT, Silverman RW, et al. Betabox: a beta particle imaging system based on a position sensitive avalanche photodiode. *Phys Med Biol.* 2013;58:3739-3753.
62. Wang J, Hwang K, Braas D, et al. Fast metabolic response to drug intervention through analysis on a miniaturized, highly integrated molecular imaging system. *J Nucl Med.* 2013;54:1820-1824.
63. Shi K, Liu Z, Ziegler SI, Schwaiger M, Shi K, Liu Z, Ziegler SI, Schwaiger MShi K, Liu Z, Ziegler SI, Schwaiger Ms; US 20140121493 A1, assignee. System and Apparatus for Multimodality-compatible High-quality Intravital Radionuclide Imaging, 2014.
64. Pittet Mikael J, Weissleder R. Intravital Imaging. *Cell.* 2011;147:983-991.
65. Hoole S. *The Select Works of Antony van Leeuwenhoek, Containing His Microscopical Discoveries in Many of the Works of Nature*: London: Black-Horse Court, Fleet-Street; 1800.
66. Vajkoczy P, Ullrich A, Menger MD. Intravital fluorescence videomicroscopy to study tumor angiogenesis and microcirculation. *Neoplasia.* 2000;2:53-61.
67. Vakoc BJ, Lanning RM, Tyrrell JA, et al. Three-dimensional microscopy of the tumor microenvironment in vivo using optical frequency domain imaging. *Nat Med.* 2009;15:1219-1223.
68. Dewhirst MW, Ong ET, Braun RD, et al. Quantification of longitudinal tissue pO2 gradients in window chamber tumours: impact on tumour hypoxia. *Brit J Cancer.* 1999;79:1717-1722.
69. Egeblad M, Ewald AJ, Askautrud HA, et al. Visualizing stromal cell dynamics in different tumor microenvironments by spinning disk confocal microscopy. *Dis Model Mech.* 2008;1:155-167; discussion 165.
70. Beerling E, Ritsma L, Vrisekoop N, Derksen PWB, van Rheenen J. Intravital microscopy: new insights into metastasis of tumors. *J Cell Sci.* 2011;124:299-310.
71. Cárdenas-Navia LI, Mace D, Richardson RA, Wilson DF, Shan S, Dewhirst MW. The Pervasive Presence of Fluctuating Oxygenation in Tumors. *Cancer Res.* 2008;68:5812-5819.
72. Øye KS, Gulati G, Graff BA, Gaustad J-V, Brurberg KG, Rofstad EK. A novel method for mapping the heterogeneity in blood supply to normal and malignant tissues in the mouse dorsal window chamber. *Microvasc Res.* 2008;75:179-187.
73. Olafsson R, Bauer DR, Montilla LG, Witte RS. Real-time, contrast enhanced photoacoustic imaging of cancer in a mouse window chamber. *Opt Express.* 2010;18:18625-18632.
74. Gaustad JV, Brurberg KG, Simonsen TG, Mollatt CS, Rofstad EK. Tumor vascularity assessed by magnetic resonance imaging and intravital microscopy imaging. *Neoplasia.* 2008;10:354-362.
75. Gough DA, Kumosa LS, Routh TL, Lin JT, Lucisano JY. Function of an Implanted Tissue Glucose Sensor for More than 1 Year in Animals. *Sci Transl Med.* 2010;2:42-53.
76. Reitan NK, Thuen M, Goa PE, Davies CdL. Characterization of tumor microvascular structure and permeability: comparison between magnetic resonance imaging and intravital confocal imaging. *J Biomed Opt.* 2010;15:036004-036011.
77. Jürgen KW, Nicholas van B, Ludger MD, Sanjiv SG. Molecular imaging in drug development. *Nat Rev Drug Discov.* 2008;7:591-607.

78. Huang SC, Phelps ME, Hoffman EJ, Sideris K, Selin CJ, Kuhl DE. Noninvasive determination of local cerebral metabolic rate of glucose in man. *Am J Physiol.* 1980;238:E69-82.
79. Phelps ME, Huang SC, Hoffman EJ, Selin C, Sokoloff L, Kuhl DE. Tomographic measurement of local cerebral glucose metabolic rate in humans with (F-18)2-fluoro-2-deoxy-D-glucose: validation of method. *Ann Neurol.* 1979;6:371-388.
80. Day FL, Link E, Ngan S, et al. FDG-PET metabolic response predicts outcomes in anal cancer managed with chemoradiotherapy. *Brit J Cancer.* 2011;105:498-504.
81. Koppenol WH, Bounds PL, Dang CV. Otto Warburg's contributions to current concepts of cancer metabolism. *Nat Rev Cancer.* 2011;11:325-337.
82. Wiebe LI. FDG Metabolism: Quaecumque Sunt Vera …. *J Nucl Med.* 2001;42:1679-1681.
83. Adams V, Kempf W, Hassam S, Briner J. Determination of hexokinase isoenzyme I and II composition by RT-PCR: increased hexokinase isoenzyme II in human renal cell carcinoma. *Biochem Mol Med.* 1995;54:53-58.
84. Higashi T, Tamaki N, Honda T, et al. Expression of glucose transporters in human pancreatic tumors compared with increased FDG accumulation in PET study. *J Nucl Med.* 1997;38:1337-1344.
85. Higashi T, Saga T, Nakamoto Y, et al. Relationship between retention index in dual-phase (18)F-FDG PET, and hexokinase-II and glucose transporter-1 expression in pancreatic cancer. *J Nucl Med.* 2002;43:173-180.
86. Lee JD, Yang WI, Park YN, et al. Different Glucose Uptake and Glycolytic Mechanisms Between Hepatocellular Carcinoma and Intrahepatic Mass-Forming Cholangiocarcinoma with Increased 18F-FDG Uptake. *J Nucl Med.* 2005;46:1753-1759.
87. Amann T, Maegdefrau U, Hartmann A, et al. GLUT1 expression is increased in hepatocellular carcinoma and promotes tumorigenesis. *Am J Pathol.* 2009;174:1544-1552.
88. Rivenzon-Segal D, Rushkin E, Polak-Charcon S, Degani H. Glucose transporters and transport kinetics in retinoic acid-differentiated T47D human breast cancer cells. *Am J Physiol Endocrinol Metab.* 2000;279:E508-519.
89. Higashi T, Tamaki N, Torizuka T, et al. FDG uptake, GLUT-1 glucose transporter and cellularity in human pancreatic tumors. *J Nucl Med.* 1998;39:1727-1735.
90. Yen TC, See LC, Lai CH, et al. 18F-FDG uptake in squamous cell carcinoma of the cervix is correlated with glucose transporter 1 expression. *J Nucl Med.* 2004;45:22-29.
91. Wolf A, Agnihotri S, Micallef J, et al. Hexokinase 2 is a key mediator of aerobic glycolysis and promotes tumor growth in human glioblastoma multiforme. *J Exp Med.* 2011;208:313-326.
92. Patra KC, Wang Q, Bhaskar PT, et al. Hexokinase 2 is required for tumor initiation and maintenance and its systemic deletion is therapeutic in mouse models of cancer. *Cancer Cell.* 2013;24:213-228.
93. Ahn KJ, Hwang HS, Park JH, et al. Evaluation of the role of hexokinase type II in cellular proliferation and apoptosis using human hepatocellular carcinoma cell lines. *J Nucl Med.* 2009;50:1525-1532.
94. Amann T, Maegdefrau U, Hartmann A, et al. GLUT1 Expression Is Increased in Hepatocellular Carcinoma and Promotes Tumorigenesis. *Am J Pathol.* 2009;174:1544-1552.
95. Nakajo M, Kajiya Y, Tani A, et al. 18FDG PET for grading malignancy in thymic epithelial tumors: Significant differences in 18FDG uptake and expression of glucose transporter-1 and hexokinase II between low and high-risk tumors: Preliminary study. *Eur J Radiol.* 2012;81:146-151.
96. Yun J, Rago C, Cheong I, et al. Glucose deprivation contributes to the development of KRAS pathway mutations in tumor cells. *Science.* 2009;325:1555-1559.
97. Zhao Y, Butler EB, Tan M. Targeting cellular metabolism to improve cancer therapeutics. *Cell Death Dis.* 2013;4:e532.
98. Smith TAD. The rate-limiting step for tumor [18F]fluoro-2-deoxy-D-glucose (FDG) incorporation. *Nucl Med Biol.* 2001;28:1-4.
99. Higashi T, Tamaki N, Torizuka T, et al. FDG Uptake, GLUT-1 Glucose Transporter and Cellularity in Human Pancreatic Tumors. *J Nucl Med.* 1998;39:1727-1735.

100. Paudyal B, Oriuchi N, Paudyal P, Higuchi T, Nakajima T, Endo K. Expression of glucose transporters and hexokinase II in cholangiocellular carcinoma compared using [18F]-2-fluro-2-deoxy-D-glucose positron emission tomography. *Cancer Sci.* 2008;99:260-266.
101. Shim HK, Lee WW, Park SY, Kim H, Kim SE. Relationship between FDG uptake and expressions of glucose transporter type 1, type 3, and hexokinase-II in Reed-Sternberg cells of Hodgkin lymphoma. *Oncol Res.* 2009;17:331-337.
102. Ong LC, Jin Y, Song IC, Yu S, Zhang K, Chow PKH. 2-[18F]-2-deoxy-D-glucose (FDG) uptake in human tumor cells is related to the expression of GLUT-1 and hexokinase II. *Acta Radiol.* 2008;49:1145-1153.
103. Mamede M, Higashi T, Kitaichi M, et al. [18F]FDG uptake and PCNA, Glut-1, and Hexokinase-II expressions in cancers and inflammatory lesions of the lung. *Neoplasia.* 2005;7:369-379.
104. Wong K-P, Sha W, Zhang X, Huang S-C. Effects of Administration Route, Dietary Condition, and Blood Glucose Level on Kinetics and Uptake of F-18-FDG in Mice. *J Nucl Med.* 2011;52:800-807.
105. Rodriguez-Enriquez S, Marin-Hernandez A, Gallardo-Perez JC, Moreno-Sanchez R. Kinetics of transport and phosphorylation of glucose in cancer cells. *J Cell Physiol.* 2009;221:552-559.
106. Gerlowski LE, Jain RK. Physiologically based pharmacokinetic modeling: Principles and applications. *J Pharm Sci.* 1983;72:1103-1127.
107. Morris ED, Endres CJ, Schmidt KC, Christian BT, Muzic Jr RF, Fisher RE. Kinetic modeling in positron emission tomography. *Emission Tomography: The Fundamentals of PET and SPECT Academic, San Diego.* 2004.
108. Mager DE, Wyska E, Jusko WJ. Diversity of Mechanism-Based Pharmacodynamic Models. *Drug Metab Dispos.* 2003;31:510-518.
109. DiStefano JJ, 3rd. Noncompartmental vs. compartmental analysis: some bases for choice. *Am J Physiol.* 1982;243:R1-6.
110. Press WH, Teukolsky SA, Vetterling WT, Flannery BP. *Numerical recipes in C: the art of scientific computing*: Cambridge University Press; 1992.
111. Pelizzari CA, Chen GT, Spelbring DR, Weichselbaum RR, Chen CT. Accurate three-dimensional registration of CT, PET, and/or MR images of the brain. *J Comput Assist Tomogr.* 1989;13:20-26.
112. Lassen NA, Perl W. *Tracer kinetic methods in medical physiology*: Raven Press; 1979.
113. Sokoloff L, Reivich M, Kennedy C, et al. The [^{14}C]deoxyglucose method for the measurement of local cerebral glucose utilization; theory, procedure, and normal values in the conscious and anesthetized albino rat. *J Neurochem.* 1977;28:897-916.
114. Reivich M, Alavi A, Wolf A, et al. Glucose metabolic rate kinetic model parameter determination in humans: the lumped constants and rate constants for [18F]fluorodeoxyglucose and [11C]deoxyglucose. *J Cereb Blood Flow Metab.* 1985;5:179-192.
115. Peltoniemi P, Lönnroth P, Laine H, et al. Lumped constant for [18F]fluorodeoxyglucose in skeletal muscles of obese and nonobese humans. *Am J Physiol Endocrinol Metab.* 2000;279:E1122-E1130.
116. Faber TL, McColl RW, Opperman RM, Corbett JR, Peshock RM. Spatial and temporal registration of cardiac SPECT and MR images: methods and evaluation. *Radiology.* 1991;179:857-861.
117. Anderson DH. *Compartmental analysis in Biology and Medicine.* Vol 81. 2 ed: The University of Michigan Press, Ann Arbor; 1986.
118. Anderson DH. Compartmental modeling and tracer kinetics. *Lecture Notes in Biomathematics.* Vol 50: Springer-Verlag; 1983.
119. Wienhard K. Measurement of glucose consumption using [(18)F]fluorodeoxyglucose. *Methods.* 2002;27:218-225.
120. Timurdogan E, Alaca BE, Kavakli IH, Urey H. MEMS biosensor for detection of Hepatitis A and C viruses in serum. *Biosens Bioelectron.* 2011;28:189-194.
121. Ríos Á, Ríos Á, Zougagh M, Zougagh M. Sample preparation for micro total analytical systems (μ-TASs). *TrAC Trends Anal Chem.* 2013;43:174-188.

122. Wu J, Gu M. Microfluidic sensing: state of the art fabrication and detection techniques. *J Biomed Opt.* 2011;16:080901-080901-080912.
123. McDonald JC, Duffy DC, Anderson JR, et al. Fabrication of microfluidic systems in poly(dimethylsiloxane). *Electrophoresis.* 2000;21:27-40.
124. Blow N. Microfluidics: in search of a killer application. *Nat Meth.* 2007;4:665-670.
125. Blow N. Microfluidics: the great divide. *Nat Meth.* 2009;6:683-686.
126. Volpatti LR, Yetisen AK. Commercialization of microfluidic devices. *Trends Biotechnol.* 2014;32:347-350.
127. Beebe DJ, Mensing GA, Walker GM. Physics and applications of microfluidics in biology. *Annu Rev Biomed Eng.* 2002;4:261-286.
128. Qin D, Xia Y, Rogers J, Jackman R, Zhao X-M, Whitesides G. Microfabrication, Microstructures and Microsystems. In: Manz A, Becker H, eds. *Microsystem Technology in Chemistry and Life Science.* Vol 194: Springer Berlin Heidelberg; 1998:1-20.
129. Santiago JG. Electroosmotic Flows in Microchannels with Finite Inertial and Pressure Forces. *Anal Chem.* 2001;73:2353-2365.
130. Wolfe DB, Conroy RS, Garstecki P, et al. Dynamic control of liquid-core/liquid-cladding optical waveguides. *Proc Natl Acad Sci U S A.* 2004;101:12434-12438.
131. Wainright A, Nguyen UT, Bjornson T, Boone TD. Preconcentration and separation of double-stranded DNA fragments by electrophoresis in plastic microfluidic devices. *Electrophoresis.* 2003;24:3784-3792.
132. Ceyssens F, Witters D, Van Grimbergen T, Knez K, Lammertyn J, Puers R. Integrating optical waveguides in electrowetting-on-dielectric digital microfluidic chips. *Sensor Actuat B.* 2013;181:166-171.
133. Huo D-Q, Liu Z, Hou C-J, et al. Recent Advances on Optical Detection Methods and Techniques for Cell-based Microfluidic Systems. *Chinese J Anal Chem.* 2010;38:1357-1365.
134. Yi C, Zhang Q, Li C-W, Yang J, Zhao J, Yang M. Optical and electrochemical detection techniques for cell-based microfluidic systems. *Anal Bioanal Chem.* 2006;384:1259-1268.
135. Ke N, Wang X, Xu X, Abassi YA. The xCELLigence system for real-time and label-free monitoring of cell viability. *Methods Mol Biol.* 2011;740:33-43.
136. Haandbaek N, With O, Burgel SC, Heer F, Hierlemann A. Resonance-enhanced microfluidic impedance cytometer for detection of single bacteria. *Lab Chip.* 2014;14:3313-3324.
137. Vu NT, Yu ZTF, Silverman RW, et al. Performance of an integrated microfluidic chip and position sensitive APD for the detection of beta emitting probes in cell cultures. Paper presented at: Nuclear Science Symposium Conference Record; Oct. 26 2007-Nov. 3 2007, 2007.
138. Fang C, Wang Y, Vu NT, et al. Integrated Microfluidic and Imaging Platform for a Kinase Activity Radioassay to Analyze Minute Patient Cancer Samples. *Cancer Res.* 2010;70:8299-8308.
139. Sha W, Yu Z, Vu N, et al. Optimal design of a new kinetic strategy for extracting FDG transport and uptake information in microfluidic multi-chamber cell culture chip coupled with PSAPD camera. *Ieee Nuclear Science Symposium Conference Record*; 2009:3936-3942.
140. Hak S, Reitan NK, Haraldseth O, Davies CD. Intravital microscopy in window chambers: a unique tool to study tumor angiogenesis and delivery of nanoparticles. *Angiogenesis.* 2010;13:113-130.
141. Sandison J. A new method for the microscopic study of living growing tissues by the introduction of a transparent chamber in the rabbit's ear. *The Anat Rec.* 1924;28:281-287.
142. Ide AG, Baker NH, Warren SL. Vascularization of the Brown Pearce rabbit epithelioma transplant as seen in the transparent ear chamber. *Am J Roentgenol.* 1939;42:891-899.
143. Yuan F, Salehi HA, Boucher Y, Vasthare US, Tuma RF, Jain RK. Vascular Permeability and Microcirculation of Gliomas and Mammary Carcinomas Transplanted in Rat and Mouse Cranial Windows. *Cancer Res.* 1994;54:4564-4568.
144. Koehl G, Gaumann A, Geissler E. Intravital microscopy of tumor angiogenesis and regression in the dorsal skin fold chamber: mechanistic insights and preclinical testing of therapeutic strategies. *Clin Exp Metastasis.* 2009;26:329-344.

145. Simonsen TG, Gaustad JV, Rofstad EK. Development of hypoxia in a preclinical model of tumor micrometastases. *Int J Radiat Oncol Biol Phys.* 2010;76:879-888.
146. Dewhirst MW, Secomb TW, Ong ET, Hsu R, Gross JF. Determination of Local Oxygen Consumption Rates in Tumors. *Cancer Res.* 1994;54:3333-3336.
147. Oishi H, Sunamura M, Egawa S, et al. Blockade of Delta-Like Ligand 4 Signaling Inhibits Both Growth and Angiogenesis of Pancreatic Cancer. *Pancreas.* 2010;39:897-903.
148. Koschwanez HE, Klitzman B, Reichert WM. Percutaneous window chamber method for chronic intravital microscopy of sensor-tissue interactions. *J Diabetes Sci Technol.* 2008;2:977-983.
149. Vestvik IK, Egeland TAM, Gaustad J-V, Mathiesen B, Rofstad EK. Assessment of microvascular density, extracellular volume fraction, and radiobiological hypoxia in human melanoma xenografts by dynamic contrast-enhanced MRI. *J Magn Reson Imaging.* 2007;26:1033-1042.
150. Li CY, Shan S, Huang Q, et al. Initial stages of tumor cell-induced angiogenesis: evaluation via skin window chambers in rodent models. *J Natl Cancer Inst.* 2000;92:143-147.
151. Palmer GM, Fontanella AN, Shan S, Dewhirst MW. High-resolution in vivo imaging of fluorescent proteins using window chamber models. *Methods Mol Biol.* 2012;872:31-50.
152. Laschke MW, Vollmar B, Menger MD. The dorsal skinfold chamber: window into the dynamic interaction of biomaterials with their surrounding host tissue. *Eur Cell Mater.* 2011;22:147-164.
153. Shan S, Lockhart AC, Saito WY, Knapp AM, Laderoute KR, Dewhirst MW. The Novel Tubulin-binding Drug BTO-956 Inhibits R3230Ac Mammary Carcinoma Growth and Angiogenesis in Fischer 344 Rats. *Clin Cancer Res.* 2001;7:2590-2596.
154. Waki A, Fujibayashi Y, Magata Y, et al. Glucose Transporter Protein-Independent Tumor Cell Accumulation of Fluorine-18-AFDG, a Lipophilic Fluorine-18-FDG Analog. *J Nucl Med.* 1998;39:245-250.

2. Materials and Methods for Continuously Infused Microfluidic Radioassay System

The development and validation of a microfluidic radioassay system was one of the main projects of this thesis. In the following chapters 2, 3 and 4, the system is described in detail. The text is from our accepted manuscript [Zhen Liu*, Ziying Jian*, Qian Wang, Tao Cheng, Benedikt Feuerecker, Markus Schwaiger, Sung-Cheng Huang, Sibylle I. Ziegler and Kuangyu Shi. "A Continuously Infused Microfluidic Radioassay System for the Characterization of Cellular Pharmacokinetics." Journal of Nuclear Medicine. (*: co-first author)], with additional details.

In this study, the final version of the Matlab program code for the image processing was done by Dr. Kuangyu Shi, and Dr. Qian Wang wrote the very first version of the Matlab code. All the kinetic modeling program code in both Matlab version and Microsoft Visual C++ version was provided by Dr. Kuangyu Shi. The Monte-Carlo simulation using Geant4 for depth-dependent sensitivity correction of the positron camera was done by Dr. Qian Wang. The qPCR experiments were performed by Ziying Jian and Tao Cheng.

A typical detection process for the CIMR includes: on-chip cell culture, on-chip CIMR measurement and data processing and analysis.

2.1. Microfluidics

2.1.1. Continuously infused microfluidic radioassay (CIMR) system

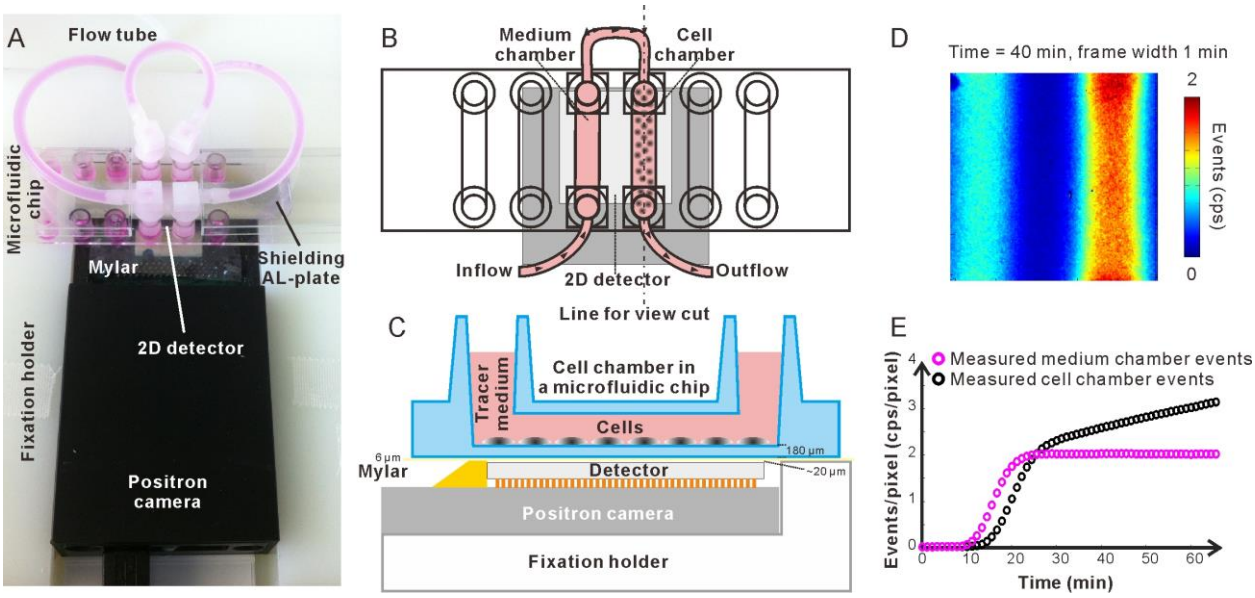

Figure 2.1 Setup of the continuously infused microfluidic radioassay (CIMR) system: (A) a photo of the microfluidic chip in operation; (B) a sketch of the tracer medium flow during the measurement; (C) a side view at the line of view cut on panel b for the cell chamber during the measurement; (D) an example frame from the positron camera during the CIMR measurement; (E) an example of time-course events/pixel curves from the medium chamber (pink) and the cell chamber (black).

The continuously infused microfluidic radioassay system is based on a microfluidic chip (µ-Slide VI0.4, ibidi GmbH, Munich, DE), a flow control unit and a positron camera as shown in Figure 2.1. The microfluidic chip consists of two parallel chambers ($17 \times 3.8 \times 0.4$ mm^3 each), each one with separate inlet and outlet. The two chambers are connected as shown in Figure 2.1B. One of them serves as a medium monitoring chamber and the other as a cell culture chamber. The flow control unit is a programmable syringe pump (Cavro® XLP 6000, Tecan Group Ltd. Männedorf, CH) with connecting flow tubes. The medium with radioactive tracer is driven by the pump from the medium reservoir via the medium monitoring chamber into the cell culture chamber (Figure 2.1B). The medium monitoring chamber and the cell culture chamber were simultaneously measured by a positron camera during the measurements (Figure 2.1C). The positron camera consists of a single-particle counting silicon pixel detector (300 µm thickness, Crypix, Crytur Ltd. Turnov, CZ) bonded to a CMOS readout chip (Timepix, CERN,

CH). The field-of-view of the positron camera is 14 ×14 mm^2 (256 × 256 pixels). Details of the basic performance of this detector for direct positron measurement can be found in [*1*]. Figure 2.1D shows an example frame from the camera during the CIMR measurement, the frame width is 1 min and the time of measurement is 40 min after starting the tracer infusion. In the image, both chambers can be distinguished; the left chamber had less readout events (bright blue color) while the right chamber had a larger number of readout events (red and yellow color). The left chamber is the medium chamber and the right chamber is the cell chamber. The events-per-pixel curves along the time taken from the medium chamber and the cell chamber are shown in figure 2.1E. The medium with radioactivity flows from the medium chamber to the cell chamber, so the medium chamber shows the rise of the signal earlier than the cell chamber. The signal in the medium chamber is constant while the signal is increasing along the time in the cell chamber.

2.1.2. Detection procedure

Cell culture preparation

Two types of human cancer cell lines, Capan-1 (pancreas adenocarcinoma) and SkBr3 (breast adenocarcinoma), were selected for the investigation. Two days before the CIMR measurements, approximately 1.5×10^4 cells in 30 µl single-cell suspension were inoculated into the cell culture chamber of a microfluidic chip using a pipette. Cells formed a homogeneous single layer on the bottom surface of the chamber. The cells were then cultured by DMEM medium (Biochrom GmbH, Berlin, DE) with 25 mM glucose, 4 mM glutamine, supplemented with 10% fetal bovine serum, 100 U/ml penicillin, and 100 µg/ml streptomycin in an incubator (Heraeus Microbiological Incubator Series 6000, Thermo Scientific) with controlled condition of 37 ºC and 5% CO_2.

Measurements with the CIMR system

Before the infusion, the flow control unit was sterilized and cleaned using 70% ethanol and ultrapure water. ^{18}F-FDG was diluted into the cell culture medium to generate a radioactive solution of 0.2-5 MBq/mL with the investigated glucose concentration. The tracer medium solution was pumped through the medium chamber and cell chamber at a constant flow of 1.25 µl/s flow of 1.25 µl/s, which created a small shear stress (< 0.13 dyn/cm2, estimated based on the application note of ibidi GmbH) near the chamber surface. This flow speed leads to a medium refresh rate of 2.5 times per minute, which is sufficient to maintain a constant supply of ^{18}F-FDG in the micro chambers. Positrons emitted both, from the medium chamber and the cell chamber, were measured by the positron camera for 75 min. Measurements were binned into frames of 1 min each. Each measurement was repeated for 6 times.

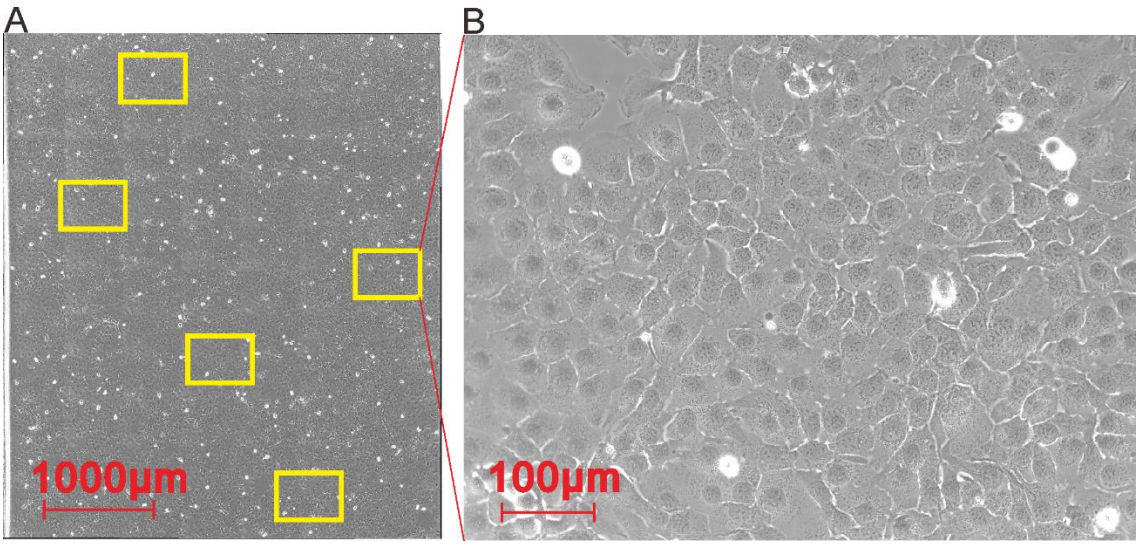

Figure 2.2 Example of microscopic image after CIMR measurement for cell counting: (A) imaging of the cells with a large field-of-view (FOV). The yellow boxes depict the selected small FOVs for cell counting; (B) typical microscopy image with a small FOV (725 µm × 546 µm) for cell counting corresponding to the selected yellow box in (A).

After the CIMR measurements, the cell chamber was imaged using a microscope (BZ-9000, Keyence Co Ltd, JP) with a phase contrast objective lens of 20. Five widely distributed microscopic FOVs were selected for counting the number of cells (see Figure 2.2). The cells imaged in the displayed FOVs are nearly homogeneously distributed. Thus, the average of the cell numbers for 5 widely distributed FOVs is assumed to be representative for the cell number density on the chip. In addition to the proposed method, several other cell counting methods were tested, including (1) trypsin detachment of cells and then counting cell number after trypan blue staining with manual counting as well as machine counting using Invitrogen Countess™ Automated Cell Counter, Beckman Counter Vi-CELL™ and CASY Cell Counter and Analyzer; (2) total protein analysis (BCA protein assay). The proposed method used and described in the study showed the smallest variation for the samples inoculated from the same cell concentration and in the same condition. The average cell number of the 5 FOVs was then normalized to the cell number per detector pixel (55 × 55 µm^2).

2.1.3. Image processing and normalization

The acquired dynamic data was corrected for radioactive decay. For each 1-minute frame, the mean events per pixel (55 × 55 µm^2) within a box region of interest (12 × 3.8 mm^2) in the center of an imaged chamber were calculated separately for the medium chamber and for the cell chamber. Time activity curves (TACs) were generated to describe the changes of mean events

per pixel versus time. The calibrated radioactivity of the medium in the cell chamber was estimated based on the measured TAC of the medium chamber after correction of delay and dispersion. This can be described using the following formula [*2*]:

$$\beta_{cm}(t) = \beta_m(t - \Delta T) * \frac{1}{\tau} e^{-\frac{t}{\tau}}$$

where β_{cm} and β_m denotes, respectively, the event density curves of the medium in the cell chamber and the medium chamber ΔT and τ are coefficients characterizing the delay and dispersion of the FDG activity flowing from the medium chamber to the cell chamber and $*$ represents the convolution operator.

To estimate the delay and dispersion coefficients, the CIMR system was run 6 times without cells in the cell chamber using the same fluidic condition as the real measurements. The coefficients of the decay and dispersion were determined regularly, especially after changes of the settings of the CIMR operating condition.

The microfluidic chamber has a height of 400 µm and the positron camera is placed below the chamber. Thus, the positron camera had lower sensitivity for the positrons emitted from upper layers than from bottom layers in the chamber. This depth-dependent sensitivity profile of the positron camera was corrected in the measurements by multiplying a correction factor of 1.74 (see chapter 2.2.1).

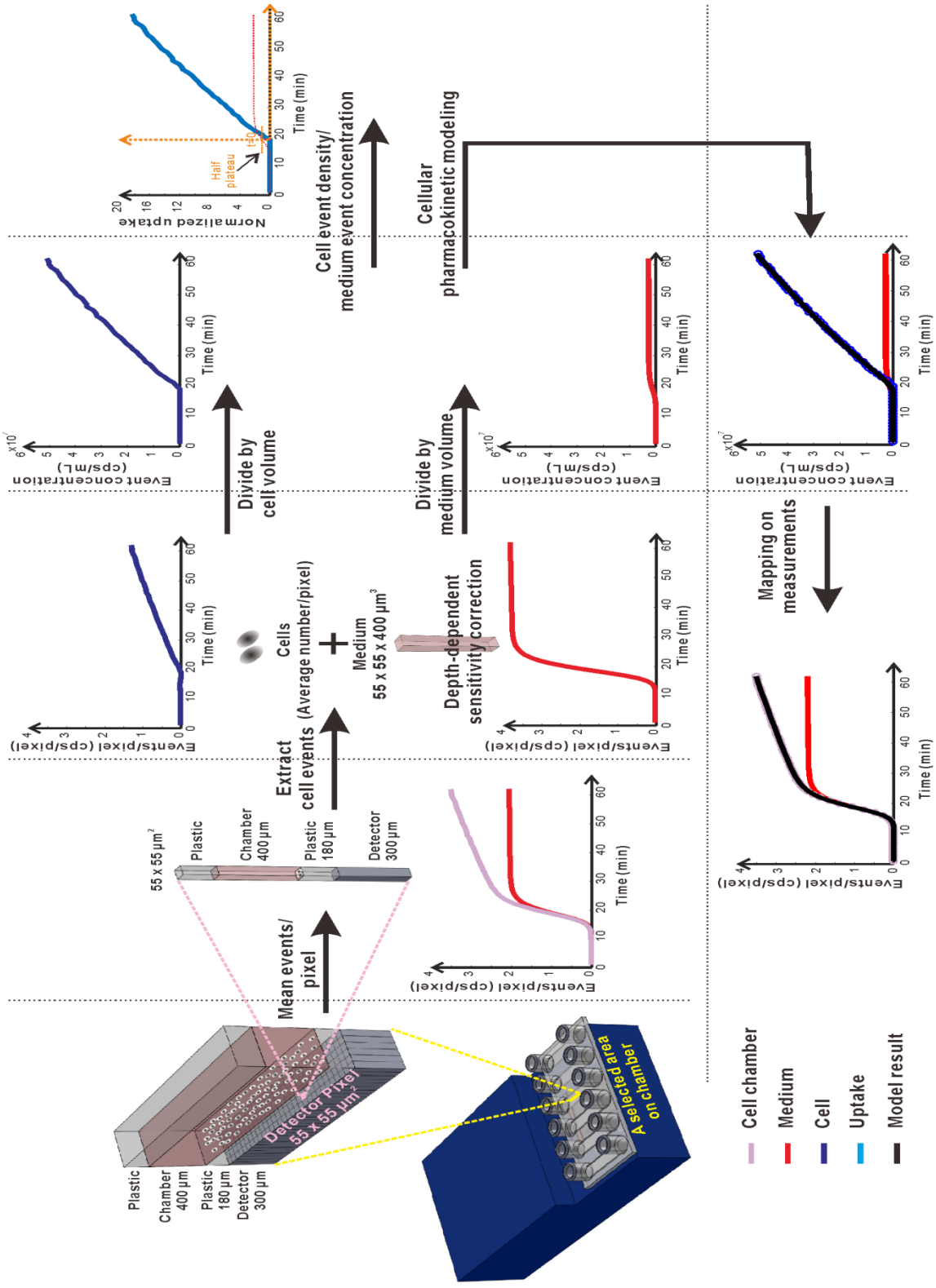

Figure 2.3 Procedure of data processing

The events of the cells in the cell chamber were generated by subtracting the estimated medium events in the cell chamber from the total events of the cell chamber (i.e., the events in the medium was removed from the total measured events in the cell chamber). The FDG concentration in the medium was computed by normalizing to the volume associated with a pixel in the chamber (55 × 55 × 400 μm). The cellular FDG concentration was calculated using an estimated mean cell number and mean cell volume (see Figure 2.3). The mean volume of adherent cells with mean diameter *d* was approximated by the volume of an ellipsoid ($\pi d^3/12$). The cellular uptake was estimated as the ratio of cellular FDG events (cps) per 10^6 cells over the corresponding medium FDG event density (cps/mL) (see Figure 2.3). The r*elative uptake ratios* of CIMR were calculated as the ratios between the normalized uptake TACs of the corresponding culture conditions for each time point. Similarly, the relative uptake ratios for conventional uptake experiment were computed as the ratios between uptake values at the discrete measurement times. In this study, the uptake ratios relative to that with the culture medium of 5 mM were calculated. All the processing was implemented using MATLAB 2012b (The Mathworks, Inc., Natick, MA, USA, Program done by Dr. Kuangyu Shi).

2.1.4. Cellular pharmacokinetic modeling

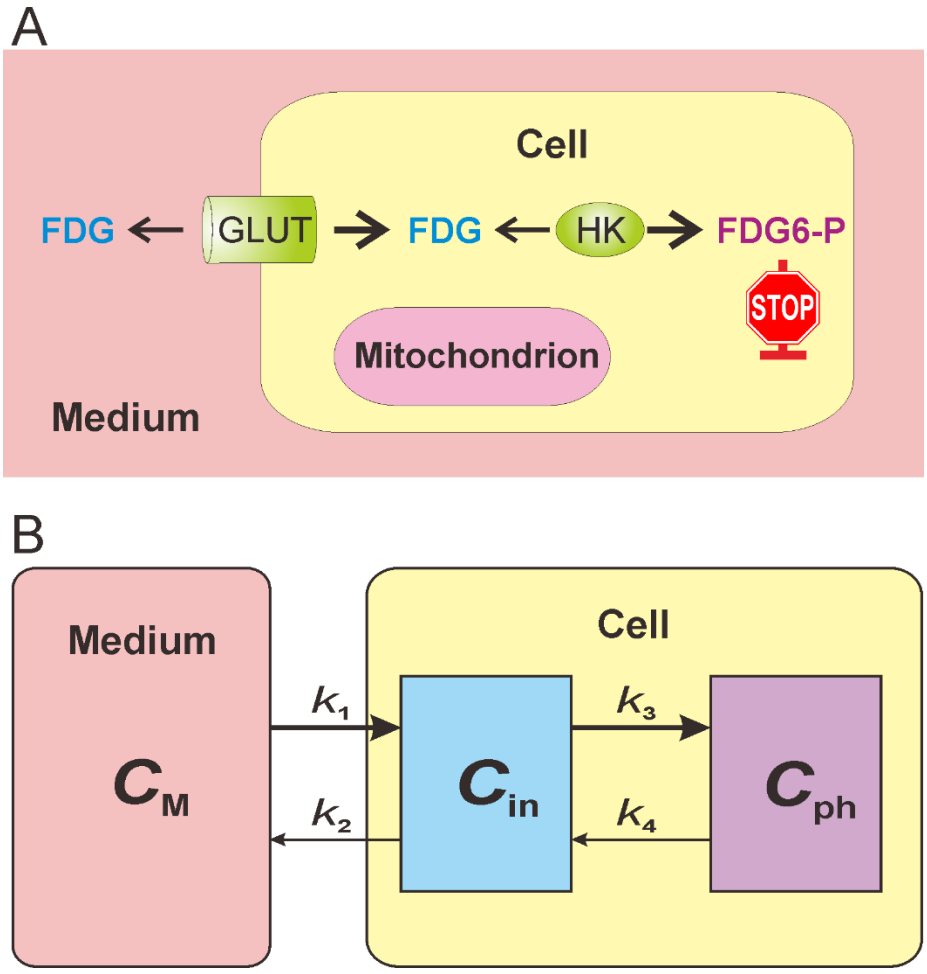

Figure 2.4 Sketches of (A) the procedure of FDG uptake and (B) the corresponding cellular pharmacokinetic modeling.

Based on the TACs obtained from the CIMR measurement, the pharmacokinetic parameters related to GLUT and HK can be estimated. For FDG, the uptake is controlled by the GLUT and HK phosphorylation (Figure 2.4A). A cellular two compartment model was constructed to estimate the kinetic parameters relating to ^{18}F-FDG transport and phosphorylation [*3*] (Figure 2.4B).

Given the medium event density β_{cm}, the free FDG events in cell β_{in} and the phosphorylated FDG events β_{ph} in cell can be described as following

$$\frac{d\beta_{in}(t)}{dt} = k_1\beta_{cm}(t) - k_2\beta_{in}(t) - k_3\beta_{in}(t) + k_4\beta_{ph}(t)$$

$$\frac{d\beta_{ph}(t)}{dt} = k_3\beta_{in}(t) - k_4\beta_{ph}(t)$$

where k_1, k_2, k_3 and k_4 are rate constants. k_1 and k_2 stand for the import and export rate of FDG across the cell membrane respectively. k_3 and k_4 are the phosphorylation and de-phosphorylation rates of FDG inside cell. The parameters were estimated by fitting the TACs derived from CIMR measurements. The model fit was performed by a trust-region algorithm implemented using C++ with Intel Math Kernel Library (MKL).

A Michaelis-Menten equation was applied to interpret the relation between the estimated rate constants (k_1 and k_3) and mRNA expressions of the corresponding enzyme or transporter [*4*]:

$$k \sim \frac{V_{max}}{K_m + C_{endo}}$$

where C_{endo} is the concentration of the endogenous substrate, K_m is the substrate concentration at half maximum reaction rate, and V_{max} is the maximum reaction rate, which is assumed to be proportional to protein expression. Considering that medium glucose concentration was kept constant before and during CIMR, the endogenous glucose concentration was assumed to be the same as the medium glucose concentration. The FDG concentration is negligible compared to the medium glucose concentration. For each cell line, we used fitting of the Michaelis-Menten equation to understand if the Km rate can be the same for culturing with different glucose concentrations. Nonlinear least square fit was applied to fit the cellular pharmacokinetic parameter with the mRNA expressions.

Pearson correlation was applied to compare the relative uptake ratios between CIMR and conventional uptake experiments. The paired Student's t-test was used to further compare the relative standard deviation (std/mean) of the two methods. A significance level of $p<0.05$ was established.

2.2. Calibration and connections

2.2.1. Depth-dependent sensitivity correction

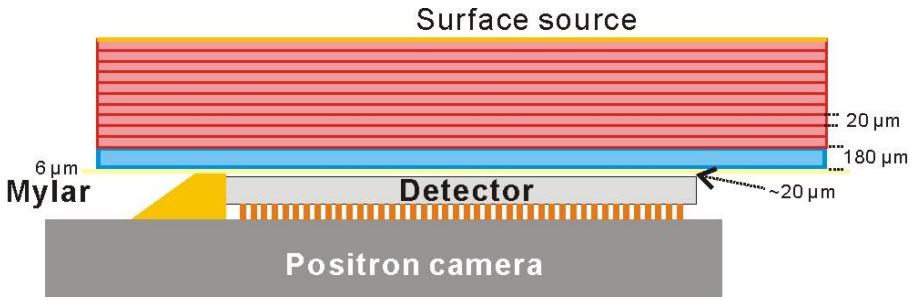

Figure 2.5 Sketch of depth-dependent sensitivity correction

The sensitivity of the positron detector decreases as the distance between the detector and the layer of the medium increases because positrons interact before they reach the detector. The depth-dependent sensitivity profile of the Timepix chip was calibrated by a depth-dependent correction factor, which is estimated based on the Monte-Carlo simulations using Geant4 [Done by Dr. Qian Wang], a toolkit modeling the physical processes of particles passing through matter [*5*]. The simulation of the positron measurement using the Timepix chip was verified in previous studies [*1,6*]. As the Figure 2.5 displays, a surface source emitting ^{18}F positrons arbitrarily from a box region (5 x 5 cm^2) was placed on top of a plastic layer of thickness 180 µm, a mylar layer of 6 µm and an air layer of 20 µm. The energy of the emitted positrons followed the theoretical ^{18}F positron energy spectrum (maximum energy Emax = 633 keV). Then layers of water with thickness of 20 µm were inserted one after each other between the surface source and the plastic layer. Each situation was simulated for the deduction of the depth-dependent sensitivity function. The derived depth-dependent sensitivity profile was derived as:

$$f(x) = -0.00104x + 0.4732\ (cps/Bq)$$

where x denotes the thickness of water between the source and the plastic layer. In the microfluidic study, the medium is diluted with radioactivity. Given an investigated region of area A and a radioactivity concentration of the medium of ρ, the counted events y of the positron detector is a function of the thickness of the medium l,

$$y(l) = \int_0^l f(x)Adx\rho = -0.00052A\rho l^2 + 0.4732A\rho l$$

The correction factor α for a thicker layer (thickness L_2) to a thin layer (thickness L_1) is as following

$$\alpha = \frac{L_2}{L_1} / (\frac{y(L_2)}{y(L_1)}) = \frac{(-0.00052{L_1}^2 + 0.4732L_1)L_2}{(-0.00052{L_2}^2 + 0.4732L_2)L_1}$$

The average diameter of the cell is 45.9 µm and we assume the thickness of the cell is 22.95 µm. Thus, the correction factor α applied is 1.74. So the real radioactivity of ^{18}F-FDG that is taken up into the cells should be corrected by dividing the estimated radioactivity of the cells (Radioactivity of cell chamber – predicted input radioactivity of the cell chamber) by a factor of 1.74.

2.2.2. Influence of sensitivity

The processing of data in this study does not consider the absolute radioactivity concentration. Instead, it estimates the uptake values and the kinetic parameters using event density based on measurements of captured positron events in the positron detector. Assuming the sensitivity of the detector to the cell layer is θ and the medium events have already been corrected for depth-dependent sensitivity to the cell layer (see 3.2.1). For delay and dispersion correction, the measured medium event density in the cell chamber without cells is $\beta_{cm}(t)$ and the measured medium events in medium chamber is $\beta_m(t)$.

$$\beta_{cm}(t) = \beta_m(t - \Delta T) * \frac{1}{\tau} e^{-t/\tau}$$

The absolute activity concentration $C_m(t)$ in the medium chamber is

$$C_m(t) = \frac{\beta_m(t)}{\theta}$$

The absolute activity concentration of medium in cell chamber $C_{cm}(t)$ is

$$C_{cm}(t) = \frac{\beta_{cm}(t)}{\theta} = \frac{\beta_m(t - \Delta T) * \frac{1}{\tau} e^{-t/\tau}}{\theta}$$

As θ is constant during the same measurement, we could derive

$$C_{cm}(t) = C_m(t - \Delta T) * \frac{1}{\tau} e^{-t/\tau}$$

Thus, the delay and dispersion correction are not influenced by the sensitivity and can be applied to event density.

Given the event density of cells in cell chamber $\beta_{cc}(t)$, the normalized uptake

$$\omega(t) = \frac{\beta_{cc}(t)}{\beta_{cm}(t)} = \frac{\beta_{cc}(t)/\theta}{\beta_{cm}(t)/\theta} = \frac{C_{cc}(t)}{C_{cm}(t)}$$

where $C_{cc}(t)$ is the absolute activity concentration of cells in cell chamber. It is equivalent to the normalized uptake using absolute activity concentration.

Further, for the cellular pharmacokinetic modeling, the modeling equation can be derived [*7*]

$$\begin{aligned} \beta_{cc}(t) &= \beta_{in}(t) + \beta_{ph}(t) \\ &= a_1 e^{-b_1 t} * \beta_{cm}(t) + a_2 e^{-b_2 t} * \beta_{cm}(t) \end{aligned}$$

where,

$$\begin{aligned} a_1 &= \frac{k_1(b_1 - k_3 - k_4)}{\Delta} \\ a_2 &= \frac{k_1(b_2 - k_3 - k_4)}{-\Delta} \\ b_1 &= \frac{k_2 + k_3 + k_4 + \Delta}{2} \\ b_2 &= \frac{k_2 + k_3 + k_4 - \Delta}{2} \\ \Delta &= \sqrt[+]{(k_2 + k_3 + k_4)^2 - 4k_2k_4} \end{aligned}$$

As the absolute activity concentration of cells in cell chamber $C_{cc}(t)$

$$\begin{aligned} C_{cc}(t) &= \beta_{cc}(t)/\theta \\ &= \frac{a_1 e^{-b_1 t} * \beta_{cm}(t) + a_2 e^{-b_2 t} * \beta_{cm}(t)}{\theta} \end{aligned}$$

As θ is constant and

$$C_{cm}(t) = \beta_{cm}(t)/\theta$$

Thus, we can derive

$$C_{cc}(t) = a_1 e^{-b_1 t} * C_{cm}(t) + a_2 e^{-b_2 t} * C_{cm}(t)$$

Using the event density is equivalent to using absolute radioactivity concentration in the parameter estimation of cellular pharmacokinetic modeling.

2.3. Comparison with conventional uptake experiments

2.3.1. Relative comparison

One day before the measurements, the medium in the cell chamber was switched to a special medium with 5mM, 2.5mM, or 0.5mM glucose concentration, respectively. The corresponding medium was exchanged every 8 hours until the start of the measurements to sustain stable glucose concentration. At the time of the CIMR measurements, the cells reached approximately 60%-90% confluence inside the cell chamber.

As reference, FDG uptake in cells was studied with the conventional uptake method [*8*] for each of culture conditions used in the CIMR measurements. Two days before the uptake experiment, approximately 6×10^4 cells in 300 µl suspension were inoculated into a well of a 24-well plate. One day before the uptake experiment, the cells were incubated in a medium of one of three glucose concentrations used in the CIMR studies. Medium was refreshed 4 times before the uptake measurement. During the uptake measurement, ^{18}F-FDG solution with the same glucose concentration used in the corresponding CIMR measurements was applied to the cells for 4 different time periods (10, 20, 30 and 40 min). Then the cells were washed twice with ice-cold PBS buffer and dissociated by trypsin/EDTA solution (Biochrom GmbH, Berlin, DE). The radioactivity of the collected cells in each well was measured using a gamma counter (Wallac 1470 Wizard Gamma-Counter, PerkinElmer, MA, USA). Thus, three repeated measurements of FDG uptake for incubation times of 10, 20, 30 and 40 min were obtained for each medium condition. The number of collected cells in each well was counted using the automated cell counter (Countess™, Invitrogen Life Technologies GmbH, Darmstadt, DE). The counted cell numbers of the wells with the same culture condition on the same day were averaged.

2.3.2. Quantitative comparison

The in-culture way of FDG uptake measurements were performed to compare the FDG uptake on-chip and off-chip quantitative.

The FDG uptake on the CIMR system are measured with flushing, 1) flush the tracer at 30 min post FDG infusion (Flush30); 2) flush the tracer at 40 min post FDG infusion (Flush40). Each profile was tested on 3 samples of SkBr3 cultured using medium with 0.5 mM glucose 1 day

before the experiment. The absolute uptake is compared with the conventional FDG uptake, as well as the real time measurement data with CIMR measurement.

2.4. Modeling strategy with square-function infusion profiles

The FDG uptake in SkBr3 cells with 0.5 mM glucose medium are continuous measured on the CIMR system. The same medium without FDG are flushed at 30 min and 40 min after FDG medium infusion (with 3 repeat measurements). These two different square-function infusion profiles are assessed with the kinetic modeling. The kinetics results are compared to the previous step-function infusion profiles (without flushing).

2.5. qPCR

Cells in the same conditions as in the CIMR measurements were cultured for molecular biology assays. Total RNA was extracted from each tumor cell line using the RNeasy Plus Mini Kit (QIAGEN, Limburg, NL); cDNA was prepared from the total RNA isolated with the QuantiTect Reverse Transcription Kit (QIAGEN, Limburg, NL). The sequences of primers for RT-PCR were as follows: GLUT1 [*9*]: Forward: 5'-CAG GAG ATG AAG GAA GAG-3'. Reverse: 5'-TCG TGG AGT AAT AGA AGA C-3'. HK2 [*10*]: Forward: 5'-CAA AGT GAC AGT GGG TGT GG-3'. Reverse: CAA AGT GAC AGT GGG TGT GG-3'. Housekeeping gene: Forward: 5'-CAG ATG GCA AGA CAG TAG AAG -3'. Reverse: 5'- GGC AAA AAT GGA AGC AAT GG-3'. All primers were synthesized by Eurofins Genomics. PCR were performed on Roche Light Cycler480 Instrument I/II (Roche Applied Science, Penzberg, DE) with Light Cycler 480 SYBR Green I Master kit (Roche diagnostics). PCR was performed in a 20 µl reaction mixture consisting of 3 µl PCR-grade water, 10 µl 2× Master Mix, 1 µl each 10× conc. forward and reverse primers. 5 µl cDNA templates was added to run for 45 PCR cycles (95°C for 10 s, 50°C for 20 s, and 72°C for 20 s per cycle). All PCR products were analyzed by 1.5% agarose gels electrophoresis. The calculated number of specific transcripts was normalized to the housekeeping genes β-actin (expressed as number of copies per µl of input cDNA) using the LightCyclerTM480 software version 1.05.0.39 (Roche diagnostics, Penzberg, DE).

1. Wang Q, Tous J, Liu Z, Ziegler S, Shi K. Evaluation of Timepix silicon detector for the detection of 18F positrons. *J Instrument.* 2014;9:C05067.
2. Iida H, Kanno I, Miura S, Murakami M, Takahashi K, Uemura K. Error analysis of a quantitative cerebral blood flow measurement using H2(15)O autoradiography and positron emission tomography, with respect to the dispersion of the input function. *J Cereb Blood Flow Metab.* 1986;6:536-545.
3. Sha W, Yu Z, Vu N, et al. Optimal design of a new kinetic strategy for extracting FDG transport and uptake information in microfluidic multi-chamber cell culture chip coupled with PSAPD camera. *Ieee Nuclear Science Symposium Conference Record*; 2009:3936-3942.
4. Sokoloff L, Reivich M, Kennedy C, et al. The [14C]deoxyglucose method for the measurement of local cerebral glucose utilization: theory, procedure, and normal values in the conscious and anesthetized albino rat. *J Neurochem.* 1977;28:897-916.
5. Allison J, Amako K, Apostolakis J, et al. Geant4 developments and applications. *IEEE Trans on Nucl Sci.* 2006;53:270-278.
6. Wang Q, Liu Z, Ziegler SI, Shi K. Enhancing spatial resolution of (18)F positron imaging with the Timepix detector by classification of primary fired pixels using support vector machine. *Phys Med Biol.* 2015;60:5261-5278.
7. Gunn RN, Gunn SR, Cunningham VJ. Positron Emission Tomography Compartmental Models. *J Cereb Blood Flow Metab.* 2001;21:635-652.
8. Maschauer S, Prante O, Hoffmann M, Deichen JT, Kuwert T. Characterization of 18F-FDG uptake in human endothelial cells in vitro. *J Nucl Med.* 2004;45:455-460.
9. Vaz CV, Alves MG, Marques R, et al. Androgen-responsive and nonresponsive prostate cancer cells present a distinct glycolytic metabolism profile. *Int J Biochem Cell Biol.* 2012;44:2077-2084.
10. Wolf A, Agnihotri S, Micallef J, et al. Hexokinase 2 is a key mediator of aerobic glycolysis and promotes tumor growth in human glioblastoma multiforme. *J Exp Med.* 2011;208:313-326.

3. Results for Continuously Infused Microfluidic Radioassay System

3.1. Reproducibility and stability

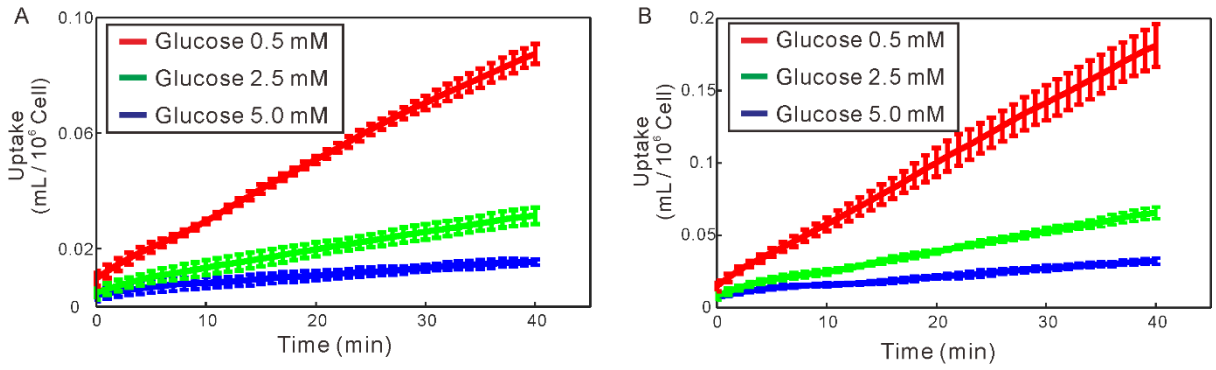

Figure 3.1 Plots of the mean and std of the normalized uptake curves for 6 repeated measurements on CIMR with 3 different culturing conditions for: (A) the cell line SkBr3 (n=6); (B) the cell line Capan-1 (n=6).

Mean and standard deviation of the estimated cellular uptake (mL / 10^6 cells) on CIMR system for 6 repeated measurements are plotted (in Figure 3.1). For the same cell under the same condition, the normalized uptake per cell followed a similar trend. The averaged relative standard deviation of normalized uptake for SkBr3 in the 3 culture media was 18.5% (5 mM), 15.1% (2.5 mM) and 5.4% (0.5 mM) (Figure 3.1A). For Capan-1, the corresponding averaged relative standard deviation was 8.8% (5 mM), 8.0% (2.5 mM) and 9.1% (0.5 mM) (Figure 3.1B).

3.2. Illustration of model fitting

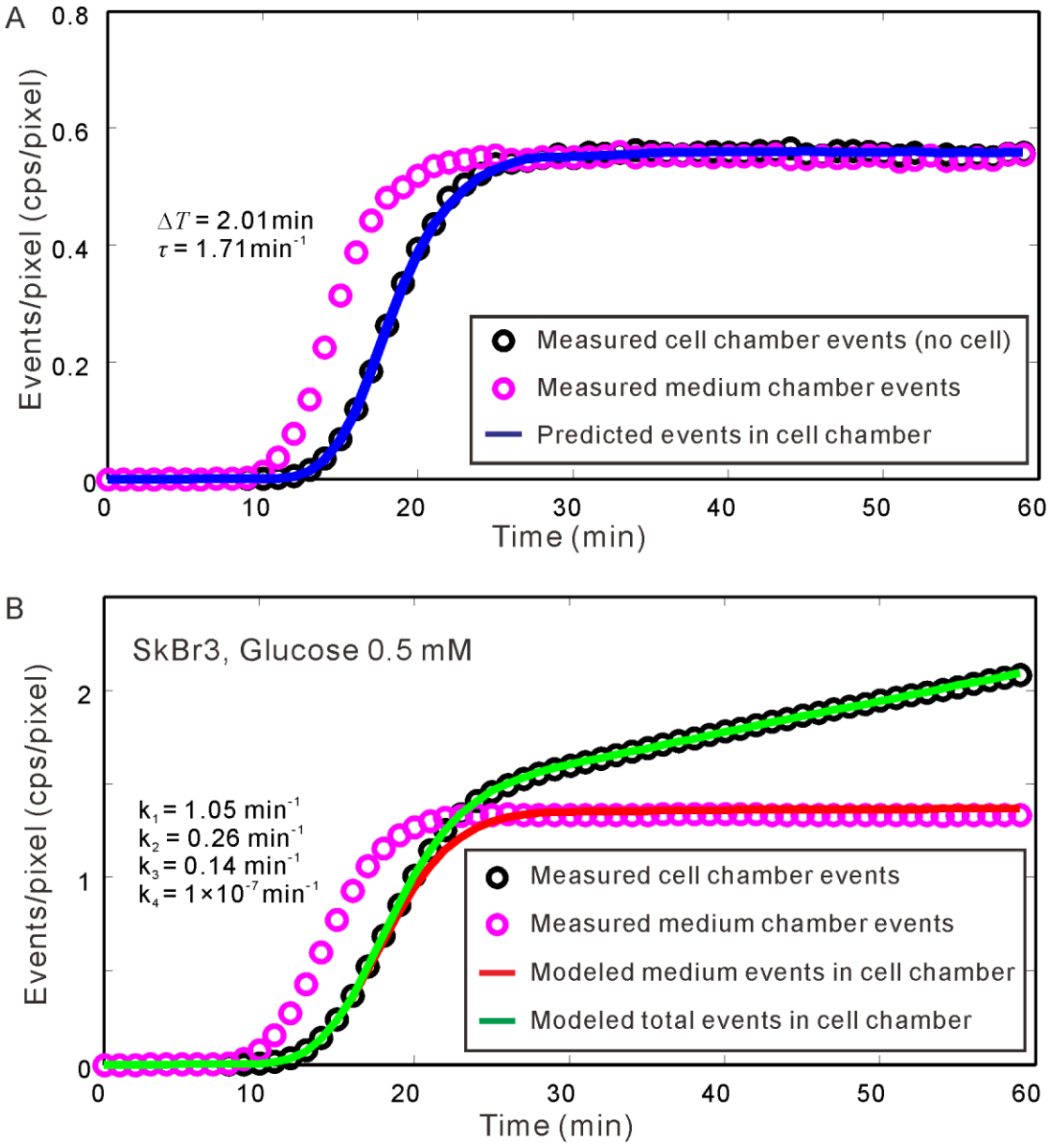

Figure 3.2 Illustration of model fitting: (A) model fitting for delay and dispersion and the predicted curve using the fit results; (B) pharmacokinetic model fitting for cellular uptake of SkBr3 cells cultured with a medium of 0.5 mM glucose.

During the continuous infusion procedure, 1.3-4.5% (3.2±1.7%, n=3) loss of cells were observed for Capan-1 and 0.9-3.5% (1.9±1.4%, n=3) loss of cells were observed for SkBr3. The difference in sensitivity of the medium chamber and the cell chamber with no cells ranged from 0.3 to 1.1% (0.6±0.3%, n=6).

The modeled curves including delay and dispersion could fit the measured curves well for the 6 calibration runs with no cells in the cell chamber (R^2=0.9995±0.0003). One example is shown in Figure 3.2A. The estimated delay ΔT (2.11±0.11 min) and dispersion coefficient τ (1.70±0.11 min^{-1}) have small relative standard deviation (<7%). When the mean delay and dispersion coefficients of the 6 curves were applied to predict the TAC in the cell chamber, the absolute percentage error was 1.3±0.3% for the 6 runs (Figure 3.2A).

The measured data of CIMR were well fitted by the cellular two-compartment model with high fitting quality (R^2>0.9999), for both SkBr3 and Capan-1 under the investigated conditions. Figure 3.2B shows an example of the model fitting for SkBr3 cultured using medium with glucose concentration of 0.5 mM. The predicted medium events in the cell chamber (after correction for delay and dispersion) are plotted as the red curve. After fitting using the cellular two compartment model, the modeled total event curve fitted well to the measured total events in the cell chamber.

3.3. Modeling strategy with square-function infusion profiles

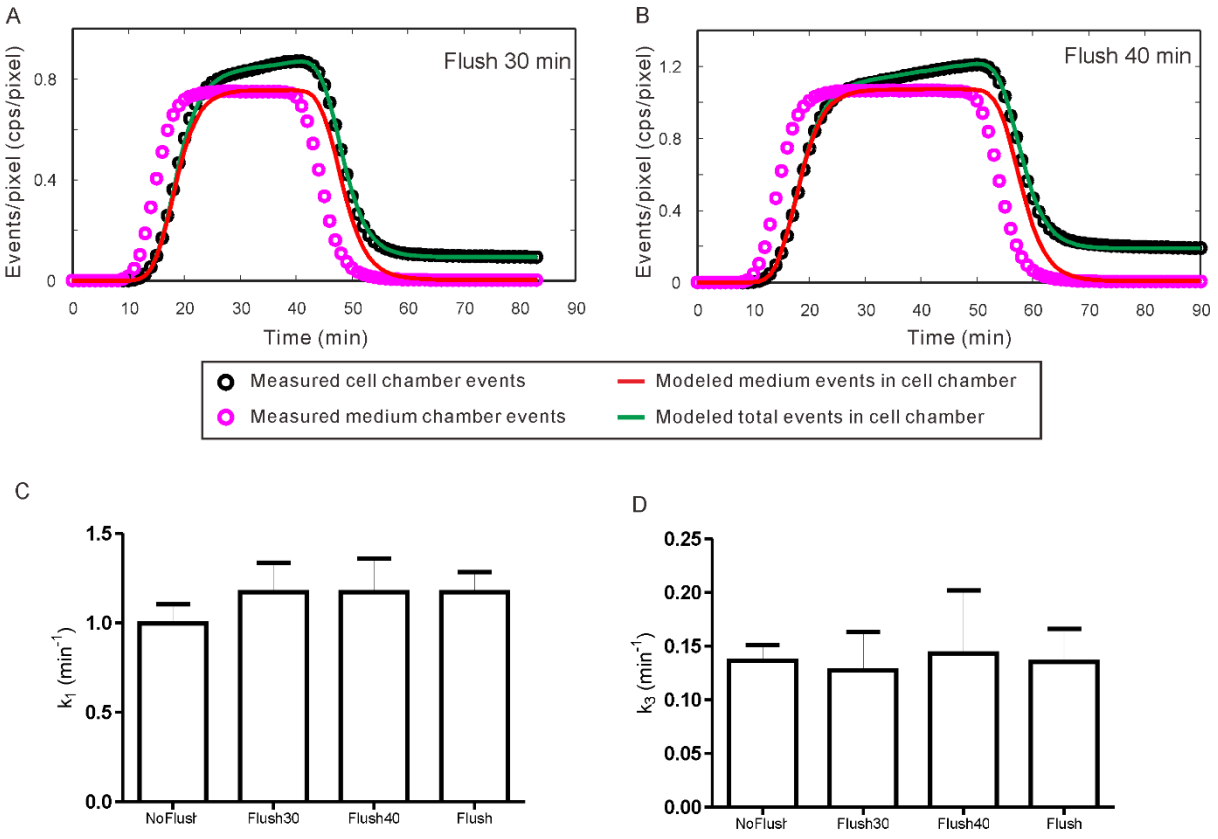

Figure 3.3 A test of CIMR using square function infusion profile: (A) an example measurement with flushing the tracer out at 30 min post infusion and the corresponding curve fitting; (B) an example measurement with flushing the tracer out at 40 min post infusion and the corresponding curve fitting; (C) compare the k_1 parameters using step function (NoFlush, n=6), flushing at 30 min (Flush30, n=3), flushing at 40 min (Flush40, n=3) and the summary of Flush30 and Flush40 (Flush, n=6); (D) compare the k_3 parameters using step function (NoFlush, n=6), flushing at 30 min (Flush30, n=3), flushing at 40 min (Flush40, n=3) and the summary of Flush30 and Flush40 (Flush, n=6);

Figure 3.3A and 3.3B show two examples of results of Flush30 and Flush40. Figure 3.3C and 3.3D compares the kinetic values of the new profiles with the previous step-function profile (n=6). The bar labeled "Flush" is the average of Flush30 and Flush40. Compared with the result of the previous step-function profile without flush, the values of k_1 (1.17±0.27) are slightly higher than that of the previous infusion profile without flush (0.99±0.26). But no significant difference has been observed using non-paired t-test. The values of k_3 using the flush profiles (0.13±0.08) are almost the same as the ones (0.14±0.04) of the previous infusion profile, no significance was observed. The overall variation of k_3 for the square pulse function (n=6) is slightly larger than the results of the step function (n=6).

3.4. Comparison with conventional uptake experiments

3.4.1. Relative comparison

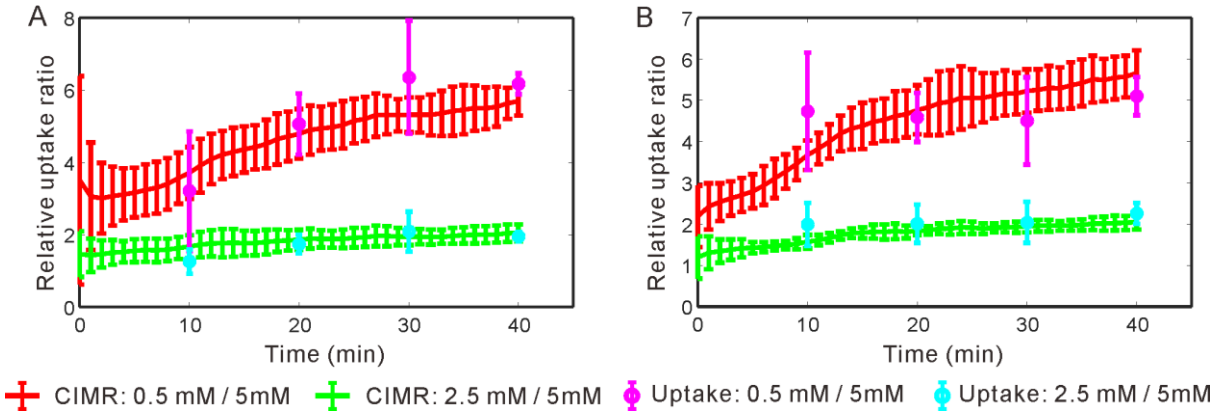

Figure 3.4 Comparison of relative uptake ratio between CIMR uptake TACs and conventional uptake measurements of (A) SkBr3 (n=6) and (B) Capan-1 (n=6). The mean and standard deviation of 6 repeated measurements of each type were plotted.

The relative uptake ratios of CIMR and conventional uptake experiments for the two investigated tumor cell lines were shown (in Figure 3.4). The mean and standard deviation were plotted. Significant correlation had been found between CIMR and conventional uptake experiments for either SkBr3 ($r=0.98$, $p=9\times10^{-6}$) as well as Capan-1 ($r=0.95$, $p=0.0003$). Overall, the CIMR methods gained 11.3% relative standard deviation, which was significantly less ($p=0.004$) than the uptake experiments of 20.8%.

3.4.2. Quantitative comparison

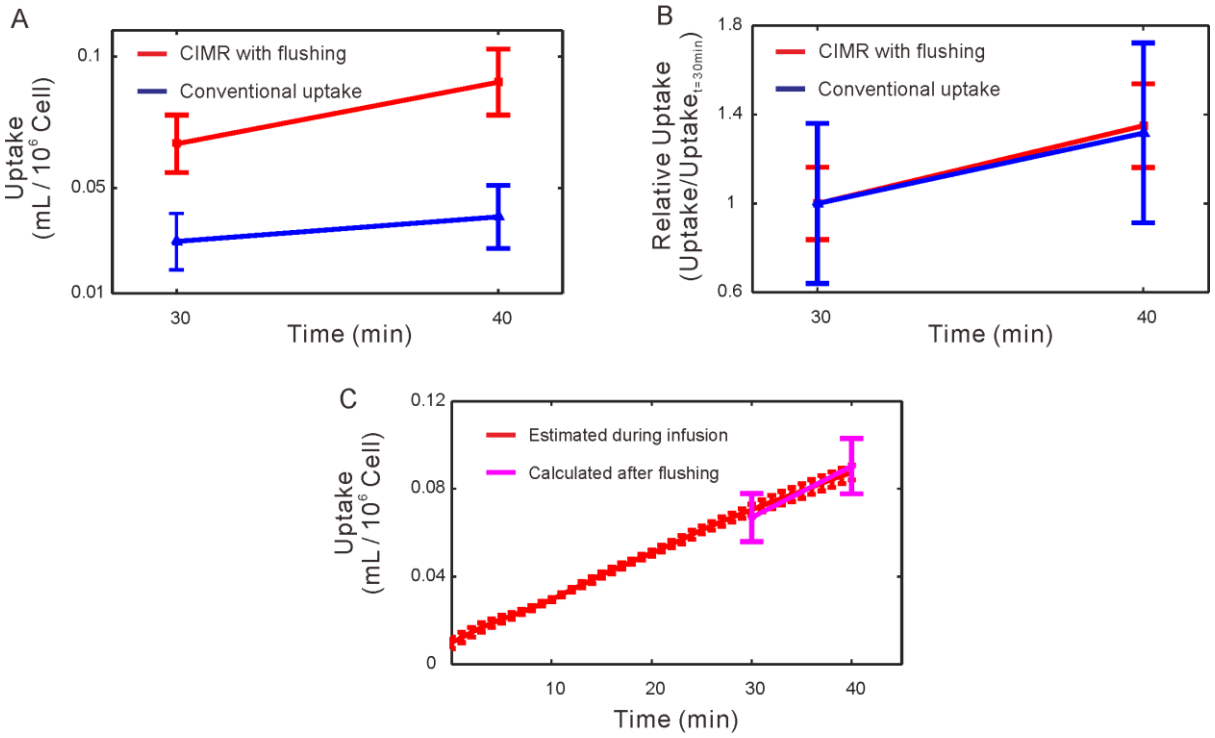

Figure 3.5 Comparison of uptake obtained on CIMR and conventional uptake experiment using well counter: A) compare the estimated uptake between CIMR after flushing the tracer out at 30 and 40 min and conventional ex-culture uptake (n=3); B) compare the relative uptake of A by normalizing each uptake to the mean values to 1 (n=3); C) compare two CIMR uptakes, 1) the estimated real-time uptake values using continuous infusion profile, 2) uptake values after flushing the tracer out at 30 and 40 min (n=3).

Compared with a conventional uptake experiment, the results were still not the same (Figure 3.5A). After normalizing with the mean uptake of flushing at 30 min post infusion, the CIMR absolute uptake and the conventional uptake showed the same increase slope (Figure 3.5B). The CIMR absolute uptake had a smaller variation than that from the conventional uptake experiment. There was observable difference between the in-culture uptake and the conventional ex-culture

uptake after cold PBS flushing and trypsin. The in-culture retention values were always higher than conventional uptake measurements. The influences of sample preparation procedure (wash with cold PBS, dissociate attached cells with trypsin) on cellular uptake are not known and further investigations are necessary to understand the difference between the in-culture and the conventional uptake measurements.

Also, the real-time uptake estimation during continuous infusion with uptake estimation using loading and flushing protocol were compared [*1*]. The uptake values obtained by measuring pure cellular events after flushing were consistent with the continuously measured CIMR uptake (Figure 3.5C). This supports that our CIMR method can reproduce the results as with the previous in-culture method [*1*].

3.5. Correlation of kinetic parameters to qPCR results

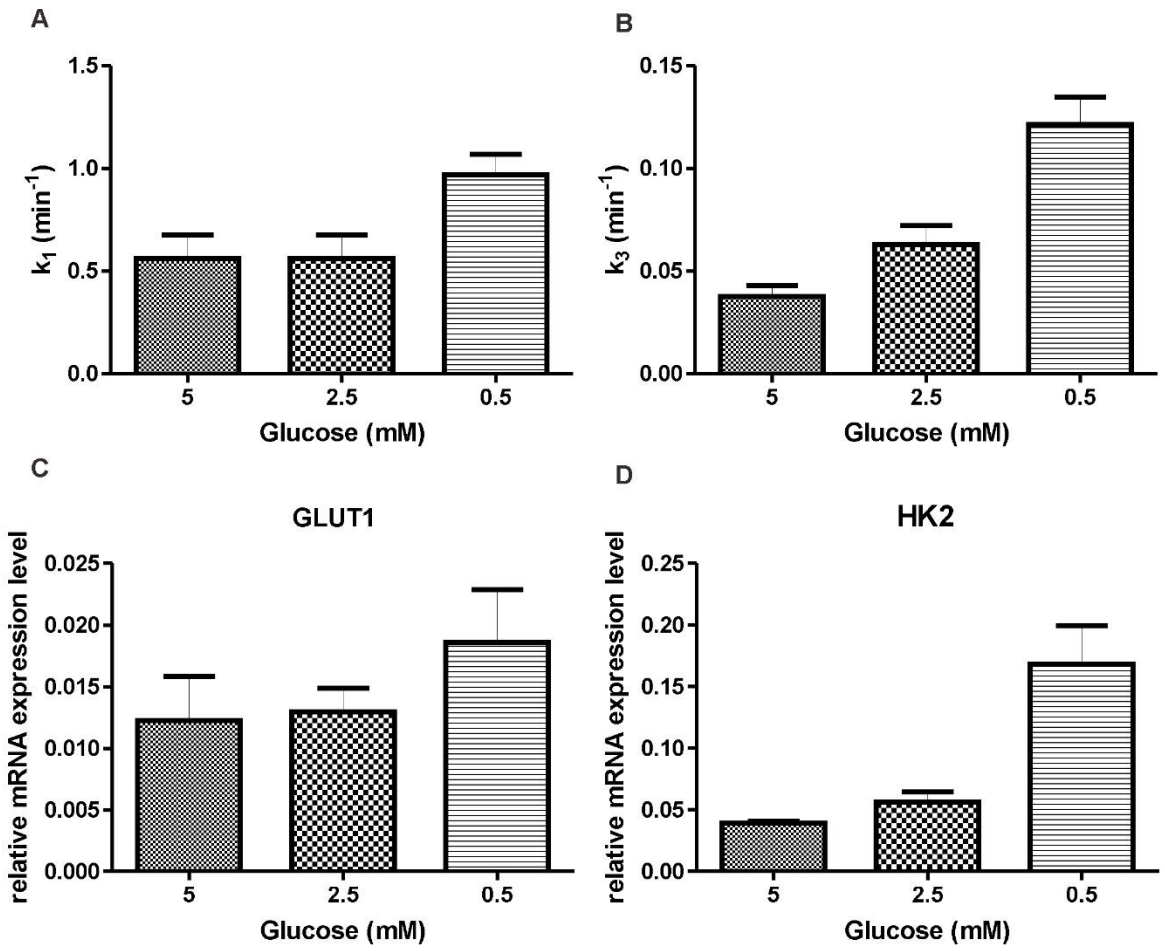

Figure 3.6 Comparison of cellular pharmacokinetics of CIMR and qPCR for SkBr3 with culture medium of different glucose concentration (5 mM, 2.5 mM & 0.5 mM): (A & B) plots of the estimated cellular pharmacokinetics k_1 and k_3 based on CIMR data; (C & D) plots of qPCR measurements of GLUT1 and HK2 for cells with the same culture conditions (n=6).

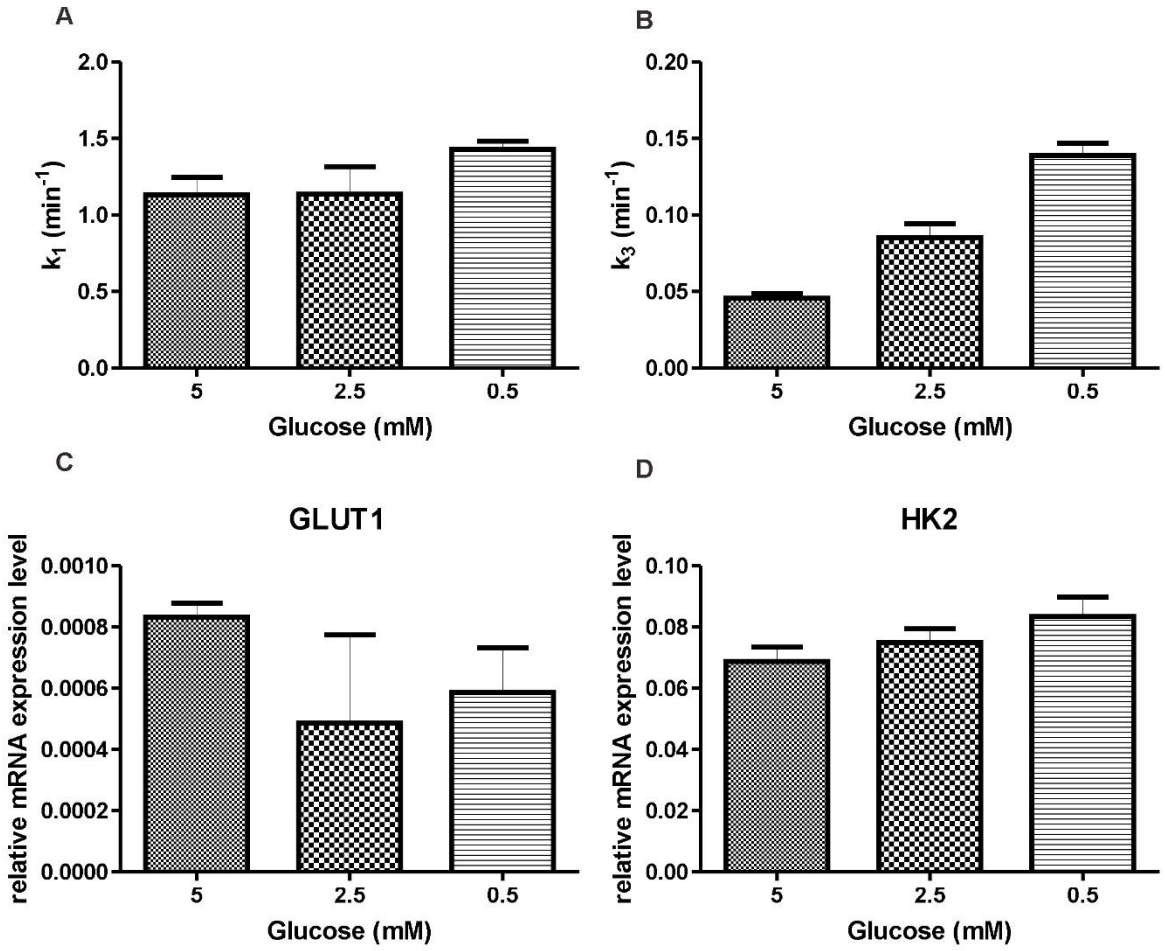

Figure 3.7 Comparison of cellular pharmacokinetics of CIMR and qPCR for Capan-1 with culture medium of different glucose concentration (5 mM, 2.5 mM & 0.5 mM): (A & B) plots of the estimated cellular pharmacokinetics k_1 and k_3 based on CIMR data; (C & D) plots of qPCR measurements of GLUT1 and HK2 for cells with the same culture conditions (n=6).

The k_1 of the SkBr3 cells cultured with 0.5 mM glucose concentration is approximately 75% higher than with glucose concentration of 2.5 mM and 5 mM (Figure 3.6). This is in agreement with the qPCR results of GLUT1 mRNA level, where the GLUT1 expression of cells with medium of 0.5 mM glucose is around 60% higher than for 2.5 mM and 5 mM medium concentrations. Similarly, the k_3 of the cells cultured with glucose concentration of 0.5 mM is

higher than in the case of 2.5 mM or 5 mM. The HK2 mRNA levels of cells with medium of glucose 0.5 mM is larger than 2.5 mM and 5 mM.

The k_1 of the Capan-1 cells cultured with glucose concentration of 0.5 mM is around 25% higher than with glucose concentration of 2.5 mM or 5 mM (Figure 3.7). However, the qPCR results of GLUT1 expression of cells with medium of glucose of 5 mM is higher than for 2.5 mM and 0.5 mM. The k_3 of the cells cultured with glucose concentration of 0.5 mM is more than 60% higher than 2.5 mM and 5 mM. However, only less than 25% increase of the HK2 mRNA levels of Capan-1 cells was observed when the condition of 0.5 mM glucose was compared with that of 2.5 mM and 5 mM glucose.

For SkBr3, the estimated cellular kinetics can be fitted with the mRNA expressions using a fixed K_m with the determinant coefficient (R^2=0.73 for k_1 and R^2=0.97 for k_3). However, for Capan-1, it is not possible to fit the estimated cellular kinetics with the corresponding mRNA levels using a fixed K_m (R^2<0).

1. Vu NT, Yu ZT, Comin-Anduix B, et al. A beta-camera integrated with a microfluidic chip for radioassays based on real-time imaging of glycolysis in small cell populations. *J Nucl Med.* 2011;52:815-821.

4. Discussion for Continuously Infused Microfluidic Radioassay System

Similar to the previous approach Betabox (discontinuous microfluidic radioassay) system [*1*], the proposed continuously infused microfluidic radioassay (CIMR) system allows in-culture measurements. It does not require loading, unloading, and cleaning of the tracer medium in the culture chamber. Thus, the measurements can deliver direct cellular uptake information without introducing additional stress during the medium exchange process. In particular, the continuous measurement of cellular uptake captures the full dynamic course of cellular uptake, enabling the application of pharmacokinetic analysis. The results of these initial tests show that this system can achieve reproducible cellular uptake measurements as well as stable estimations of cellular kinetics. However, the chamber volume of the microfluidic chip in our system is much larger than that in the Betabox system. This increased volume is necessary to obtain sufficient cell uptake signals to distinguish the background medium events during the mixture measurements of cell uptake and medium.

Technically, the following points are important for a successful CIMR measurement: (1) the plane of each micro-chamber is parallel to the plane of the positron camera detector and has the same distance, ensuring that signal sensitivity from both micro-chambers are equal; (2) each micro-chamber of the microfluidic chip has the same physical dimension, and the volume of the chamber is not changed during the fluid infusion; (3) no air bubbles in the tubing and the microfluidic chip during the measurement; (4) the signal is strong enough to be detected by the positron camera, which is related to the bottom thickness of the chip and the distance between the microfluidic chip and the detector; (5) during the operation of liquid handling, the cell culture chamber should always be kept with cell culture medium and shear stress that higher than the infusion shear stress should be avoided; (6) cells are of a type with sufficient adhesiveness to the bottom of the microfluidic chip, not being washed away during the infusion of tracer medium; (7) the radio-nuclide is emitting particles which can be detected by the positron camera.

It is very important to monitor the cell number for the CIMR assay. However, it is not feasible to monitor the cell number with microscopy during positron imaging, as the transmitted light would be shielded by the positron camera. On the other hand, the image FOV of microscopy is too small to cover all the cells in the chamber. An effort has been made by using digital microscope system (DMS1000 from Leica), which enables reflection light detection. Unfortunately, the cells on the bottom of the microfluidic chip were not visible with the digital microscope system. The strategy then went to counting the cell number before and after the

CIMR measurements. In this study, we chose the counting method that averaged the cell number counted on the microscopic images of 5 selected FOVs on the chip directly after the CIMR measurement. The cells are reported to grow uniformly in the cell chamber of our chip [*2,3*].

The medium chamber in the CIMR system monitors the medium events in the cell chamber. However, the measured medium events need to be corrected for delay and dispersion before the TAC can be used to correct the measurement of the cell chamber. The effective volume of the microfluidic chamber is 30 µL, the volume of two connectors is 56.5 µL each, and the volume of the tubing in between is 14.1 µL. Under the experimental flow speed, the theoretical delay between cell chamber and medium chamber is 2.09 min. The estimated delay coefficient $\Delta T = 2.11$ min agrees with the theoretical estimation. Although the volume between the two chambers may slightly vary due to the variability by connecting the chambers with the tubes manually, the small relative standard deviation has little influence (< 2%) on the predicted medium events of the cell chamber and can be ignored for high uptake signals.

The CIMR system is operated in a continuous infusion condition and the fluid shear stress on cells is less than 0.13 dyn/cm^2. In the physiological condition, the interstitial flow shear stress on normal tissues has been demonstrated to be in the order of 0.1 dyn/cm^2 or lower [*4,5*]. Thus the fluid shear stress in our system is similar to that in the physiological conditions. In addition, the low cell loss (<4.5%) during the CIMR measurements shows that this low shear stress does not show significant influence on the adherence of the two investigated cells in the chamber. However, for less adherent cells, even low shear stress may lead to non-negligible cell loss. Further strategies need to be developed to compensate the influence of leached-out cells for those less adherent cells. Otherwise, such cells are not suitable for the CIMR measurements.

The uptake values obtained in CIMR are calculated from event densities measured in the medium chamber and cell chamber, which are not absolute activity concentrations. The sensitivity of the system (calibration of event density to absolution activity concentration) is not considered during the calculation. In this system, we put a mylar sheet (6 µm) between the microfluidic chip and the detector to prevent possible leakage of fluid onto the semiconductor detector during port exchange. The air space between the microfluidic chip and the detector may change for different setups, leading to slightly varying absolute sensitivity. However, in this study, we measured the medium chamber and the cell chamber simultaneously. Thus, the sensitivity change did not affect the calculation of the uptake, nor the estimation of kinetic parameters (proof in 3.2.3). The difference of absolute sensitivity observed between the medium chamber and the cell chamber was less than 1.1% (0.6±0.3%), thus the same sensitivity was assumed for both chambers.

Even after careful calibration and correction, the estimated uptake values were observed to be different from the conventional uptake values obtained from well counter measurements (chapter 3.4.2). This may be explained by the difference between in-culture measurement and conventional ex-culture measurements. The influences of sample preparation procedure (wash with cold PBS, dissociate attached cells with trypsin) on cellular uptake are not known and further investigations are necessary to understand the difference between in-culture measurement and conventional uptake measurements. Nevertheless, the significant correlations between the relative uptake ratios (0.5 mM / 5 mM, 2.5 mM / 5 mM) of the two types of measurements demonstrated the consistency of relative relations between each other. As many studies investigate the relative differences under certain interventions, the systematic bias between CIMR and conventional uptake may not change the results if all the investigations were performed in in-culture measurements [*1*]. Smaller variations were achieved with the in-culture measurement using CIMR, compared with the conventional uptake experiments. Thus, the CIMR provides a stable way to investigate relative changes under interventions.

Furthermore, the uptake values obtained in CIMR are indirect estimations compared with the previous in-culture microfluidic radioassay using a loading and flushing protocol [*1*]. By adapting the infusion profile of CIMR with flushing the tracer, the pure event density of cells can be measured and the calculated uptake values are consistent with the continuously measured CIMR uptake (chapter 3.4.2). This supports the feasibility of the continuous estimation of uptake during the infusion without flushing the tracer.

For the estimation of cellular pharmacokinetics, it is necessary to estimate the concentration (event density) inside and outside of the cells. For the event density inside cells, the cell volume needs to be considered. However, the real cell volume is difficult to measure and was therefore estimated by the diameters of cells in the cell chamber. This may introduce bias for the parameter estimation. Nevertheless, the estimated kinetic parameters are consistent with the data of the same cancer in literature. For glucose concentration of 5 mM (corresponding to the human condition), the fitted phosphorylation rates (k_3) of this study ranged from 0.027 to 0.054 min^{-1} for the breast cancer cell line SkBr3. This is in agreement with the reported parameter range of 0.025 to 0.061 min^{-1} [*6*] and 0.012 to 0.078 min^{-1} [*7*] for dynamic ^{18}F-FDG PET on human breast cancer in literature. Similarly, the fitted k_3 of this study ranged from 0.031 to 0.055 min^{-1} for pancreatic cancer cell line Capan-1 for glucose concentration of 5 mM. This is also in line with a reported k_3 value 0.041 min^{-1} (separating the overall survival between 4 and 6 months) for ^{18}F-FDG PET on human pancreatic adenocarcinoma patients [*8*].

In the current set-up, the infusion protocol (input function) is a step function, which results in short transient response followed by a linear TAC. This may introduce bias in the estimation.

Further constraints can be added by adapting the infusion protocol, such as a square pulse function. In chapter 3.3, two different square function infusion profiles are tested for the estimation of the kinetic parameters on SkBr3 cells cultured using 0.5 mM glucose. Comparing the estimations using square function and step function, the values of k_1 from the square function (1.17±0.27) are slightly higher than that (0.99±0.26) of the previous step function. But no significant difference has been observed using non-paired t-test. The values of k_3 of the square function (0.13±0.08) are almost the same as that (0.14±0.04) of the step function, no significance was observed. The variation with the square function is slightly larger than the step function. There might be bias in the estimation using different infusion profiles (input functions). For the current studies, all the k_4 values are nearly 0. Although the square infusion profile may improve the estimation and reduce the bias compared with the step infusion profile, it does not bring significant difference for the studies without obvious dephosphorylation. However, the square function may bring significant improvement for the investigation of tracers with clear k_4 clearances.

The estimated kinetic parameters of this study cannot directly be linked to underlying physiological behavior. In this study, we employed a quantitative index, the mRNA level of corresponding proteins measured using qPCR, for comparison. However, the expression levels of the corresponding proteins may deviate from the mRNA expression levels [*9*]. The investigated typical glucose transporter GLUT1 and typical phosphorylation enzyme HK2 may not represent the overall function of multiple existing isoforms of GLUT and HK. In addition to protein expressions, the activities of the transporters and enzymes also influence the behavior of the transport and phosphorylation [*10*]. In contrast, the estimated kinetic parameters represent the overall effects of protein expression and activity. Furthermore, it is not always possible to fit the pharmacokinetic parameters with mRNA expressions using the Michaelis-Menten equation [*11*] with a constant K_m (failed for Capan-1). For each cell line, we tried to estimate K_m for various glucose incubation conditions. We used the model fitting to test if it is possible to interpret the relation between the mRNA expression and kinetic parameters using a constant K_m. A change in the value of the rate constant is not expected to match the change in V_{max}, especially, when the concentration of the substrate (glucose level in the present case) was altered, unless the value of K_m is much larger than the substrate concentration. Thus, it is not expected that the mRNA levels agree with the cellular pharmacokinetics of ^{18}F-FDG in all the situations.

All the current CIMR measurements were performed under the condition of normal air, room temperature (ca. 25 ºC) and room humidity, without the use of a dedicated incubator. Although we tried to minimize the measurement time outside of the incubator, this may still introduce stress to cells during the measurements leading to bias of the estimation of cellular uptake. Nevertheless, all the environmental conditions were similar for the various runs performed in

this study. Their variations were small compared to the variabilities due to the many other factors addressed earlier.

The CIMR system can be extended to measure positrons or electrons emitted by other tracers using the same detector in this study [*12,13*]. The measured signal depends on the energy of the emitted positron or electrons. For different tracers with the same positron emitter, i.e. ^{18}F labeled tracer, the proposed methods can be directly transferred. For tracers with different positron emitters like ^{68}Ga, ^{11}C, some correction coefficients, such as decay correction, or depth-dependent sensitivity correction coefficient need to be recalculated.

The pioneering microfluidic radioassay system [*1,14*] needs loading and unloading of the incubating tracers for each assay. Therefore, the measurements are restricted to several discontinuous time points and dynamic acquisition over a time course is still not possible. In addition, the medium exchange procedure needs to compromise between the completeness of the exchange medium and the maintenance of a stable culture environment [*1,14*]. Besides, the residual of tracer medium in the cell chamber is difficult to control. Different from the conventional uptake experiments and microfluidic radioassay systems, the CIMR system introduces a real-time imaging method for measuring the pharmacokinetics between a tracer and the attached cells. This is realized via simultaneously detecting the radioactivity events of a medium chamber and a cell chamber under the constant infusion of tracer medium. A similar method enabling the detection of the cellular retention and uptake kinetics is called ligand tracer technology, which is developed by Bjorke et al. [*15,16*] since 2006 and already commercialized now. The method measures the radioactivity of a fixed area where a rotating cell dish with an angle consecutively delivers cells to a fixed area of the cell dish passes by. In each round of the rotation, the cell area rotates into and out of the liquid radioactivity pool on the lower end of the cell dish, and then goes to the detection area. The ligand tracer technology is simple and it enables a time-resolved characterization of ligand-cell kinetics. Furthermore, a fluorescence detection also developed with this method, broadens the application to affinity assays and ligand-receptor interaction kinetics assays. This spin separation process enables the signals of background and integrated signal to be measured within short consecutive times. As the background and the integrated signal are not measured at the same time, the measurement is time revolved but not a real-time measurement. The tracer pool in the culture dish is a fixed total amount during each circle, the concentration is reduced as cells take up tracer in each round. Similarly to the microfluidic radioassay, the cells in the cell dish undergo a cycle of immersion into the liquid followed by deprivation in each rotation. Thus, cells experience perturbation during each stimulation cycle, which is different from an *in vivo* situation.

1. Vu NT, Yu ZT, Comin-Anduix B, et al. A beta-camera integrated with a microfluidic chip for radioassays based on real-time imaging of glycolysis in small cell populations. *J Nucl Med.* 2011;52:815-821.
2. Kim MJ, Lee SC, Pal S, Han E, Song JM. High-content screening of drug-induced cardiotoxicity using quantitative single cell imaging cytometry on microfluidic device. *Lab Chip.* 2011;11:104-114.
3. http://ibidi.com/fileadmin/support/application_notes/AN03_Growing_cells.pdf.
4. Mitchell MJ, King MR. Computational and experimental models of cancer cell response to fluid shear stress. *Front Oncol.* 2013;3.
5. Mitchell MJ, King MR. Fluid Shear Stress Sensitizes Cancer Cells to Receptor-Mediated Apoptosis via Trimeric Death Receptors. *New J Phys.* 2013;15:015008.
6. Torizuka T, Zasadny KR, Recker B, Wahl RL. Untreated primary lung and breast cancers: correlation between F-18 FDG kinetic rate constants and findings of in vitro studies. *Radiology.* 1998;207:767-774.
7. Tseng J, Dunnwald LK, Schubert EK, et al. 18F-FDG kinetics in locally advanced breast cancer: correlation with tumor blood flow and changes in response to neoadjuvant chemotherapy. *J Nucl Med.* 2004;45:1829-1837.
8. Epelbaum R, Frenkel A, Haddad R, et al. Tumor aggressiveness and patient outcome in cancer of the pancreas assessed by dynamic 18F-FDG PET/CT. *J Nucl Med.* 2013;54:12-18.
9. Shim HK, Lee WW, Park SY, Kim H, Kim SE. Relationship between FDG uptake and expressions of glucose transporter type 1, type 3, and hexokinase-II in Reed-Sternberg cells of Hodgkin lymphoma. *Oncol Res.* 2009;17:331-337.
10. Rodriguez-Enriquez S, Marin-Hernandez A, Gallardo-Perez JC, Moreno-Sanchez R. Kinetics of transport and phosphorylation of glucose in cancer cells. *J Cell Physiol.* 2009;221:552-559.
11. Sokoloff L, Reivich M, Kennedy C, et al. The [14C]deoxyglucose method for the measurement of local cerebral glucose utilization: theory, procedure, and normal values in the conscious and anesthetized albino rat. *J Neurochem.* 1977;28:897-916.
12. van Gastel R, Sikharulidze I, Schramm S, et al. Medipix 2 detector applied to low energy electron microscopy. *Ultramicroscopy.* 2009;110:33-35.
13. Esposito M, Jakubek J, Mettivier G, Pospisil S, Russo P, Solc J. Energy sensitive Timepix silicon detector for electron imaging. *Nucl Instrum Meth A.* 2011;652:458-461.
14. Wang J, Hwang K, Braas D, et al. Fast metabolic response to drug intervention through analysis on a miniaturized, highly integrated molecular imaging system. *J Nucl Med.* 2013;54:1820-1824.
15. Bjorke H, Andersson K. Automated, high-resolution cellular retention and uptake studies in vitro. *Appl Radiat Isot.* 2006;64:901-905.
16. Bjorke H, Andersson K. Measuring the affinity of a radioligand with its receptor using a rotating cell dish with in situ reference area. *Appl Radiat Isot.* 2006;64:32-37.

5. Materials and Methods for Multimodal Intravital Molecular Imaging System

The development and validation of a multimodal intravital molecular imaging (MIMI) system is the second main project of this thesis. The following chapters show preliminary studies of this system. Part of the text is from [Kuangyu Shi, Zhen Liu, Sibylle I. Ziegler and Markus Schwaiger. "System and Apparatus for Multimodality-Compatible High-Quality Intravital Radionuclide Imaging." US 20140121493 A1, 2014].

The MIMI system includes three main parts: a multimodal compatible dorsal skin window chamber, a rat with window chamber tumor model, and multimodality imaging techniques.

5.1. Multimodal compatible dorsal skin window chamber basics

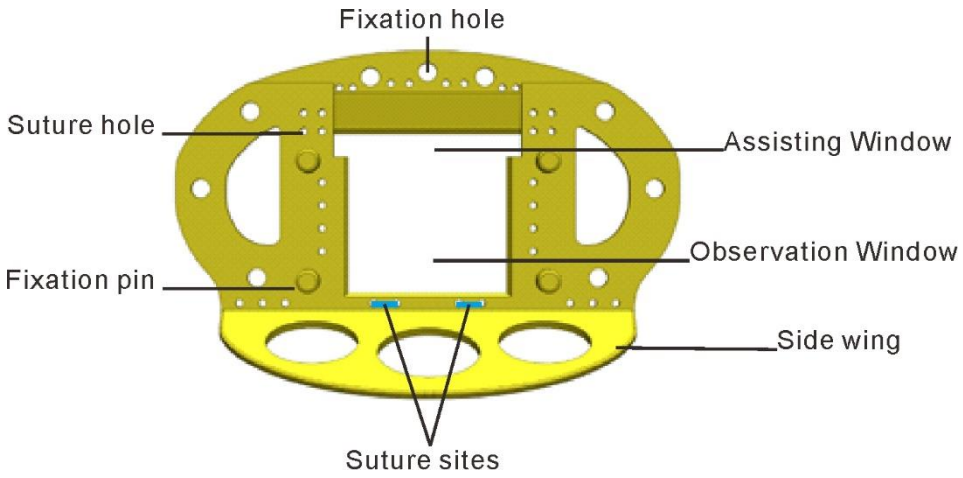

Figure 5.1 Sketch of the multimodal compatible dorsal skin window chamber plate.

The main body of the multimodal compatible dorsal skin window chamber plate, as is shown in Figure 5.1, comprises an observation window for various detectors, an assisting window to allow the insertion of other obligatory non-imaging parts of the positron camera, four fixation pins to allow the window chamber plate to be mounted with a window chamber assisting adapter and connectors for imaging, a side wing to protect the dorsal skin window chamber against tilting, fixation holes to mount fixation screws, a series of suture holes to allow the binding of sutures with the tissues for the fixation of the transparent window chamber (the selected suture sites is denoted in green). The window chamber is made from polyetheretherketone (PEEK), rigid but

flexural, and chemically inactive to a wide range of organic and inorganic chemicals and solvents [*1*]. Besides, owing to the excellent high temperature resist property (the heat distortion temperature is 152 ºC), the window chamber can be autoclaved for sterilization without deformation.

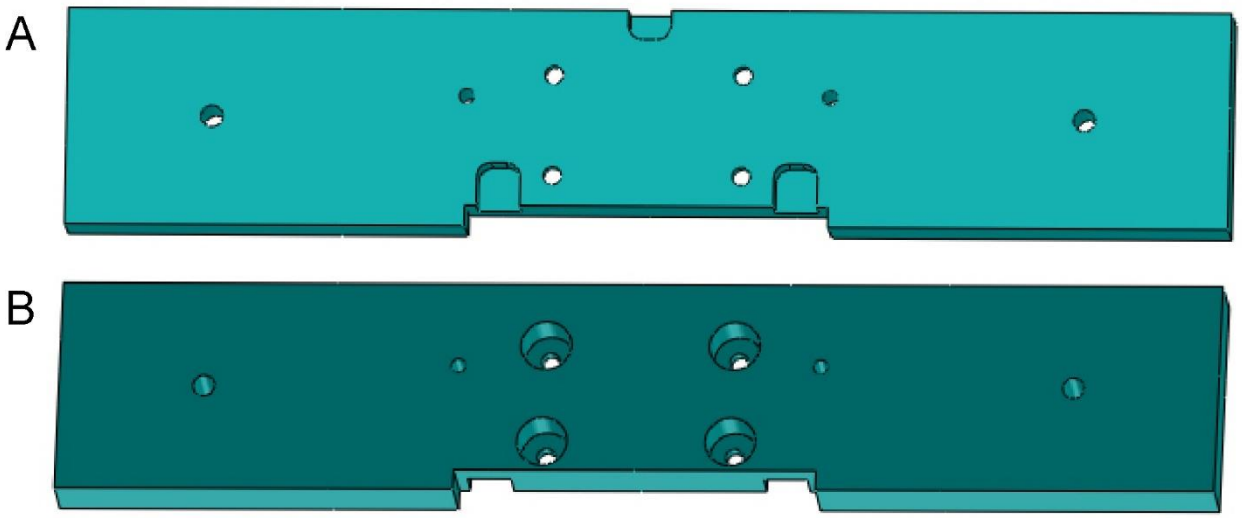

Figure 5.2 Window chamber assisting adapter: (A) the upside of the window chamber assisting adapter; (B) the downside of the window chamber assisting adapter.

The window chamber assisting adapter is used to assist the imaging of the rat tumor model with the window chamber. The upside of the window chamber assisting adapter (Figure 5.2A) can be mounted onto the window chamber, and the downside (Figure 5.2B) can be tightened with screws.

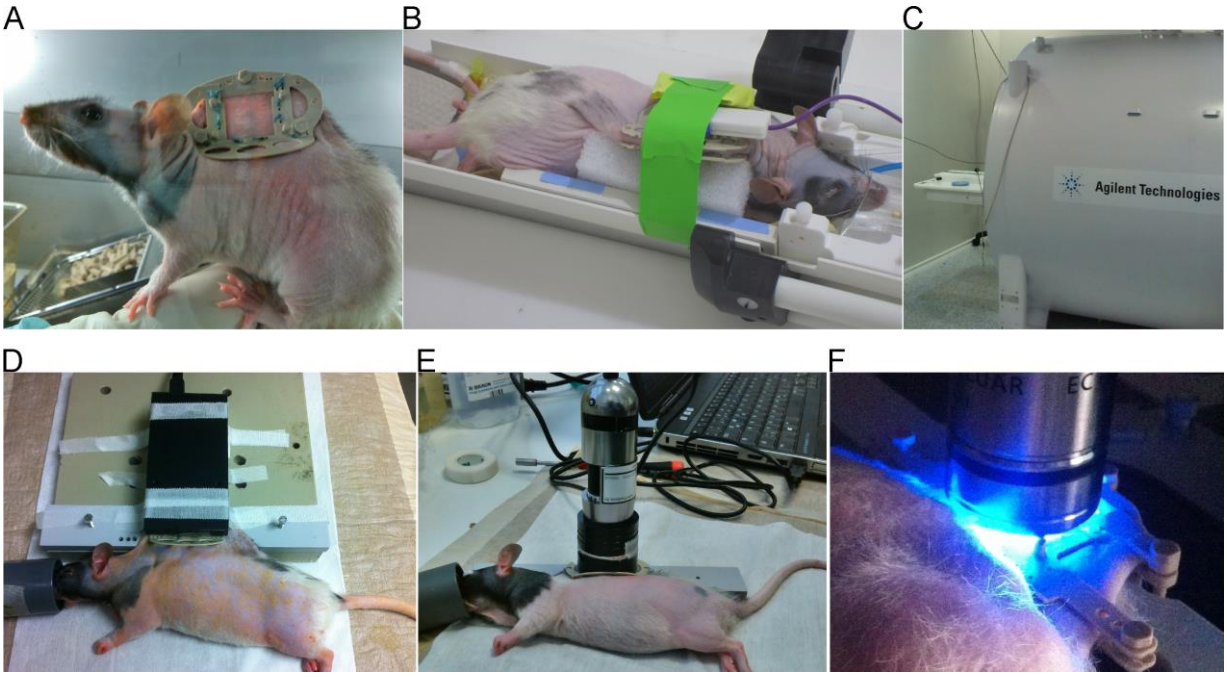

Figure 5.3 Photos of multimodal compatible rat window chamber tumor model: (A) a rat with the multimodal compatible window chamber; (B & C) the MRI imaging setting; (D) the positron imaging setting; (E) the luminance oxygen sensor imaging setting; (F) the fluorescence imaging setting.

An example rat with the multimodal compatible window chamber tumor is shown in Figure 5.3. The photos of different imaging modalities were recorded to show the availability of multimodal imaging methods. Details of the methods will be addressed separately in the following sections.

5.2. Animal and tumor model

Athymic nude rats, RNU Rat Crl: NIH-*Foxn1*^{rnu} (Strain code: 316, homozygous and immunodeficient) were from Charles River. Human colon adenocarcinoma grade II cell line HT-29 was selected for tumor transplantation on the RNU rats [*2,3*]. All the animal studies were approved by the local governmental committee for animal protection and welfare (Tierschutzbehörde, Regierung von Oberbayern, with license protocol number 18-13).

5.2.1. Window chamber implantation

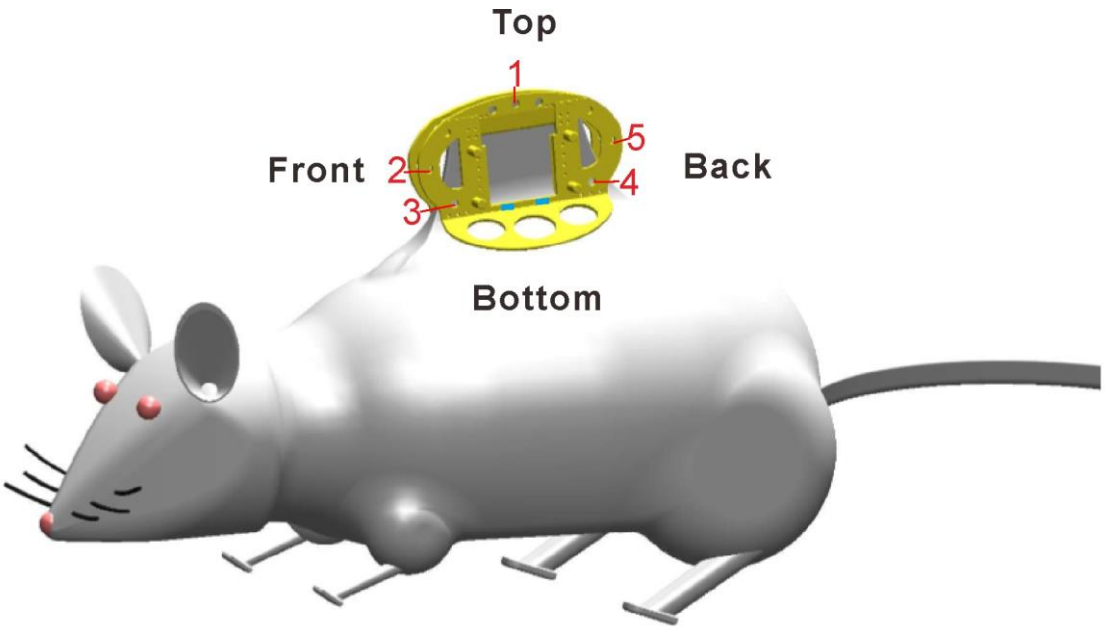

Figure 5.4 Sketch of anatomical location for the dorsal skin window chamber implantation. Numbers in red denote the screw holes used for fixation during surgery, the bright blue line shows where sutures are needed, and the orientations are noted.

The multimodal compatible dorsal skin window chamber was implanted onto the RNU rat as described previously [*4-7*]. A RNU rat of 5 weeks to 7 weeks age with weight of 120 g to 160 g was selected for surgery. Briefly, each rat was anaesthetized with an intramuscular (i.m.) injection of MMF (Midazolam/medetomidine/fentanyl with concentration in mg/ml of 5/1/0.05) [*8*] with dosing according to Table 5.1. An injection dose of 1/3 of the initial volume will be injected to prolong another 30 minutes when anesthesia time went beyond 50 minutes during the surgery operation. The dorsal skin fold of the rat was sterilized and stretched. The hole 1 of the window chamber plate was aligned to the position of ca. 2.5 cm behind the front limbs of the rat, and both the hole 1 and the window area were marked. The skin layer within the window area was cut open, and then was peeled from the body with the scissors. Afterwards, the two layers of skin between the hole 1 were punctured with an ear punch. Then, the pair of the window chamber plates was fixed onto the stretched skin fold via the punctured hole 1 with an 8 mm PEEK screw (the two skin layers between the plates were typically 2 mm to 4 mm in thickness, the fixation should not be too tight). A second PEEK screw was applied to fix the hole 2 of the pair of the window plates without the skin layers in-between, and the width between the two plates was the same as the first screw. Then, the skin fold between the hole 3 was punctured with a gouge of 18G or 16G needle without a needle tip, and fixed with a third PEEK screw.

The same procedure was applied to the hole 5, but the hole 5 was punctured with an ear punch. Hole 4 is optional for fixation. Afterwards, two U-shaped sutures were applied with a straight needle onto the bottom of the window chamber (sites see Figure 5.4 marked with bright blue line). Then, the opened skin in the window area was removed with a pair of scissors along the edge of the window. The bleeding sites were pressed with an applicator for 2-3 minutes. An 18 × 18 mm cover glass placed onto the window and then fixed with a PEEK cover plate. The rat was awaken via intraperitoneally (i.p.) injection of AFN (Atipamezole/ flumazenil/naloxone with concentration in mg/ml of 5/0.1/0.4) according to the Table 5.1. Analgesia drugs were administered following Table 5.2. The window area was checked 1 h after surgery, and the bleeding sites were stopped with an applicator when necessary. The cover glass was cleaned once a day, and changed every two days. All surgery instruments were autoclave sterile or one time disposable, and a heating pad (37 ºC) was applied beneath the animal to keep the body temperature.

Table 5.1 Anesthesia and anti-anesthesia dose

Animal weight (g)	**MMF (ml)**	**AFN (ml)**
100	0.07	0.25
125	0.08	0.31
150	0.1	0.37
175	0.11	0.43
200	0.13	0.49

Table 5.2 Analgesia drugs and their administration

Day	**Buprenorphin (s.c.)**	**Meloxicam (s.c.)**
surgery day (during surgery)	0,05mg/kg ~ 0,05ml/300g	1mg/kg ~ 0,6ml/300g
surgery day (~ 20:00 Uhr)	0,05mg/kg ~ 0,05ml/300g	
Morning, 1day after surgery	0,03mg/kg ~ 0,025ml/300g	0,2mg/kg ~ 0,15ml/300g
Evening, 1day after surgery		
Morning, 2 days after surgery		0,2mg/kg ~ 0,15ml/300g

Evening, 2 days after surgery		
Morning, 3days after surgery		0,2mg/kg ~ 0,15ml/300g

5.2.2. Tumor transplantation

Single-cell suspension of HT29 cells was prepared for tumor transplantation. Briefly, after trypsin digestion and centrifugation, the HT29 cells from the culture flask were suspended with PBS twice in single-cell form. The cell suspension containing 2×10^6 cells in 0.05 ml was prepared in an insulin needle or a 1 ml syringe with 30 G needle on the ice. The RNU rats with window chamber were anesthetized with inhalation of isoflurane in oxygen flow. The isoflurane was administered using Fluovac Anesthesia Systems (Harvard Apparatus, Cambridge, USA). The rat was put into an isolation box with 5% isoflurane in oxygen (2 L/min) for fast anesthesia induction. After the breath become slow and smooth, the rat was moved into inhalation mask with 2% isoflurane in oxygen (2 L/min) for maintenance. The tumor cells were injected subcutaneously (s.c.) into the skin area within the window. The diameter of the tumor was measured on the day 4, and checked every two day afterwards. The tumor volume was calculated with the following formula [*9*]: $V= \pi \times (a \times b^2)/6$, where a and b were the longer and shorter diameters of the tumor, respectively. The doubling time of the tumor was obtained by plotting the tumor volume versus time.

5.2.3. *In vitro* histological staining

After imaging experiments, the rat with window chamber went under euthanasia with 0.5 ml pentobarbital sodium (Narcoren, 16 g/100 ml, Merial GmbH, Germany) via tail vein injection. The skin along the window area was cut and fixed with 4% para-formalin solution for 1 day, then sunk into 70% ethanol for 1-7 days. The fixed tissue block went with paraffin embedding; and cutting for immunohistochemistry staining. A haematoxylin-eosin (H&E) staining was applied to check tumor growth state and tumor microenvironment. The paraffin tissue block went under de-paraffin and rehydrate steps with sinking in xylene solution 5 minutes each 3 times, followed by an ethanol 100% (3 minutes) - ethanol 100% (3 minutes) - ethanol 95% (3 minutes) - ethanol 95% (3 minutes) - ethanol70% (3 minutes) cycle, and then rinsed with distilled water for 5 minutes. For the staining, the tissue block was sunk in hematoxylin for 6 minutes, rinsed with tap water for 20 minutes, differentiated in acid alcohol for 1 to 3 seconds, rinsed in tap water for 5 minutes, blued in 0.2% ammonia water for 30 seconds, rinsed in tap

water for 5 minutes, and counterstained in eosin for 15 seconds. In the last, the stained tissue block went under dehydrate 4 steps: ethanol 95 % (3 minutes, discard waste each time) - ethanol 95% (3 minutes) - ethanol 100 % (3 minutes) - ethanol 100 % (3 minutes). After cleared in xylene for 5 minutes twice, the tissue block was mounted with coverslips.

The whole window chamber slice on the stained slide was recorded using a fluorescence microscopy (BZ-9000, KEYENCE), with a setting of a bright field, an objective 4 ×, and an image merge mode.

5.3. MRI imaging

The RNU rat was anesthetized with 2% isoflurane in oxygen flow (2 L/min), and a tail vein catheter was prepared in a preparation room. After 1 ml of physiological saline i.p. administration, the rat was transferred into a 7T MR scanner room immediately. The rat was fixed onto a specified rat MR bed with an air heating unit to keep the animal body temperature stable. Its head was fixed into an anesthesia inhalation mask, and a breathing pad was placed under the rat (RAPID Biomedical GmbH). A 1 Channel MiniFlex Coil (Diameter of 30 mm, RAPID Biomedical GmbH) was placed on top of the window of the window chamber, and fixed. A foam of 8 cm × 1.5 cm × 1.5 cm was placed on the other side of the window chamber plate to stabilize the fixation. A set of 0.2 ml PCR tubes one filled with 1 mmol/L gadolinium-diethylenetriamine penta-acetic acid (Gd-DTPA) solution and one filled with saline, were used as references. The reference tubes were placed one top of the MiniFlex coil and fixed. Contrast agent Gd-DTPA (MAGNOGRAF, 0.5 mmol/ml, Marotrast GmbH, Jena, Germany) was diluted in 0.9% saline to a final concentration of 0.05 mmol/ml. The contrast agent solution was filled into a 3 ml disposable syringe (B|Braun), and then further be filled into two proset paediatric connection tubing (0.5 × 2.35 × 1500 mm, B. Braun, Melsungen, Germany) combined together. The tubing was connected to the rat with a tail vein catheter. The whole set can be accommodated into a mouse body gradient coil. During MR measurements, the electrocardiogram heart rate, breathing rate and body temperature were all monitored (RAPID Biomedical GmbH). According to the breathing rate, the isoflurane was adjusted from 0.7% to 1.5% to keep the breathing rate around 50-70 times per minute. Imaging was obtained with a 7T preclinical MRI system (Agilent Technologies, Santa Clara, USA). After positioning using a triplanar (tripilot) sequence, two T1-weighted and T2-weighted MRI scans pre and post the Gd-DTPA solution administration was acquired. A syringe pump (Pump Elite 11, Harvard Apparatus, Cambridge, USA) was applied for the Gd-DTPA solution injection. The pump speed was set to 160 ml/hr, the injection volume was set according to the body weight of the rat (5.0 mL/kg (i.e., 0.25 mmol/kg)) plus 0.09 ml which was a volume left in the catheter. Some parameters, such as slice number, FOV

etc. were the same as the localization. Other parameters were set specifically: T1 weighted images (TR=300 ms, TE=1 ms, 192 × 192 matrix, 1 mm slice thickness, 4 cm × 4 cm FOV, NEX = 4. Flip angle 60), T2 weighted images (TR=3000 ms, TE=35 ms, 192 × 192 matrix, 1 mm slice thickness, 4 cm × 4 cm FOV, NEX =4. Flip angle 60). After imaging, 2 ml Ringer-Lactate solution was supplied to rat i.p. The animal was awaken afterwards, and kept on the heating pad for 10 minutes.

5.4. Positron imaging of ^{18}F-FDG

The RNU rat was anesthetized with 2% isoflurane in oxygen flow (2 L/min) using Fluovac Anesthesia Systems (Harvard Apparatus, Cambridge, USA). A tail vein catheter was prepared. ^{18}F-FDG of ca.150 MBq/kg body weight was prepared in ca. 0.5 ml saline solution and injected into the tail vein with a bolus injection in 5 s, followed by 1 ml physiological saline flush. Then the rat was awaken and put behind a shielding wall. The rat was anesthetized again 35 minutes later. The window chamber plate with intact skin was fixed with window chamber assisting adapter, and then fixed to a positron imaging stage. A Mylar sheet (6 μm) was placed on top of the window to prevent possible leakage of tissue fluids that may defect the detector. A positron camera was carefully mounted onto the four fixation pins (fiducial marker) on the window chamber. A layer of tape was applied for fixation. The positron imaging was recorded 50 minutes after the ^{18}F-FDG injection, and 10 minutes of acquisition was performed at 1 frame/s.

A dynamic imaging protocol is listed here. To realize the dynamic positron imaging, a syringe pump (Pump Elite 11, Harvard Apparatus) was applied for the tracer injection. Positron imaging was recorded 15s before the pump injection, ca. 15 MBq/kg body weight was injected inside the animal body. A 3-ml disposable syringe (B|Braun) was used to contain 0.7 ml ^{18}F-FDG saline solution, and the pump was set to drive 0.54 ml at a speed of 160 ml/h, in which 0.09 ml of tracer solution left in the catheter. The positron imaging was acquired at 1 frame/s for 15 minutes. To correctly evaluate the blood input function, a dynamic PET measurement was performed under the same pump administration protocol. The imaging was performed on a micro-PET system (Inveon, SIEMENS Preclinical Solutions, Erlangen, Germany). Three seconds after PET measurement, the pump started via rat tail vein administration. Three rats were tested. Each rat was imaged twice with a 3 days break in between each scan.

5.5. Luminance oxygen sensor imaging

The 2D oxygen map of the window area was measured with a mini-optical oxygen sensor (VisiSens™ system, PreSens, Regensburg, Germany) plus oxygen Sensor Foils (SF-RPSu4,

PreSens, Regensburg, Germany). The rat with window chamber was anaesthetized with isoflurane. The window chamber assisting adapter was placed beneath the window chamber plate with intact skin to provide a stable detection condition. A piece of oxygen sensor foil (18 × 18 mm) was placed onto the surface of the tissue inside the window chamber, with the dull white side contact to the tissue surface, ensuring that there was no air bubble in-between. The VisiSens detector with a specified adapter (see Figure 5.3) was mounted onto the window chamber. The specified adapter can isolate the surrounding light and keep the same detection condition. Then, the room light was turned off, and the surrounding environment was kept in dark. After initialization of the VisiSens detector, the image around the tumor was adjusted in focus, and 10 consecutive oxygen imaging maps were recorded every 2 seconds. Afterwards, a calibration experiment was performed in the same environment with the same detection settings. Calibration with oxygen-free water was prepared 1-2 h before the experiment, which referred to cal. 0. Surrounding air was referred as cal. 100, as the oxygen in the surrounding air was taken as 100% saturation. The oxygen-free water [*10*] was prepared with dissolving 0.5 g of sodium sulfite (Na_2SO_3, Sigma) and 25 µL of cobalt nitrate ($Co(NO_3)_2$) standard solution ($\rho(Co) = 1000$ mg/L; in nitric acid 0.5 mol/L, Westlab, Australia) in 50 mL water, and sealed in a 50 ml falcon tube. Oxygen imaging maps with oxygen free water and with air were recorded, respectively.

5.6. Fluorescence imaging

The tumor vessel network was imaged with a fluorescence microscopy (Imager. M2, Zeiss, Germany) equipped with a black/white CCD camera (AxioCam MRm, Zeiss, Germany), and an image acquisition software (AxioVision, Zeiss, Germany). Fluorescein isothiocyanate–dextran (FITC-dextran) with an average molecular weight of 2,000,000 (Sigma Aldrich, St. Louis, MO, USA) was used as a dye to delineate the blood vasculature. The rat was anesthetized with MMF. A tail vein catheter was prepared with an I.V. catheter with wings (24G, BD, Utah, USA) and sealed with a stopper (B|Braun). The window chamber was fixed onto the window chamber assisting adapter, further fixed onto a plastic plate, and then the whole set was fixed on the microscopy stage with a long clamp. Once secured, all the settings were not touched to maintain the same positron for sequential images from the microscopy. The body temperature of the rat was maintained using two sealed gloves with 40 ºC water surrounding the rat. The objective of 1.25× magnification was applied for imaging. After focus adjustment, the field-of-view of tumor microenvironment was found. A bright field image and a fluorescence image with GFP filter were recorded. Then, a fluorescence imaging movie was recorded with exposure time of 50 ms for 6 minutes, and three layers in z-direct were recorded with 1000 µm interval. The FITC-dextran (50 mg/ml in physiological saline) was injected into the tail vein 15s after the start of the video recording, with a bolus of 0.5 ml injected in 5s. After the movie recording, the

objective lens was moved away temporally. Then, a transparent plastic plate with reference pattern (Figure 5.5) was mounted to the window chamber, and a fluorescence image was recorded afterwards. The rat was awakened with corresponding AFN dose after supplement of 1ml of ringer lactate solution i.p.

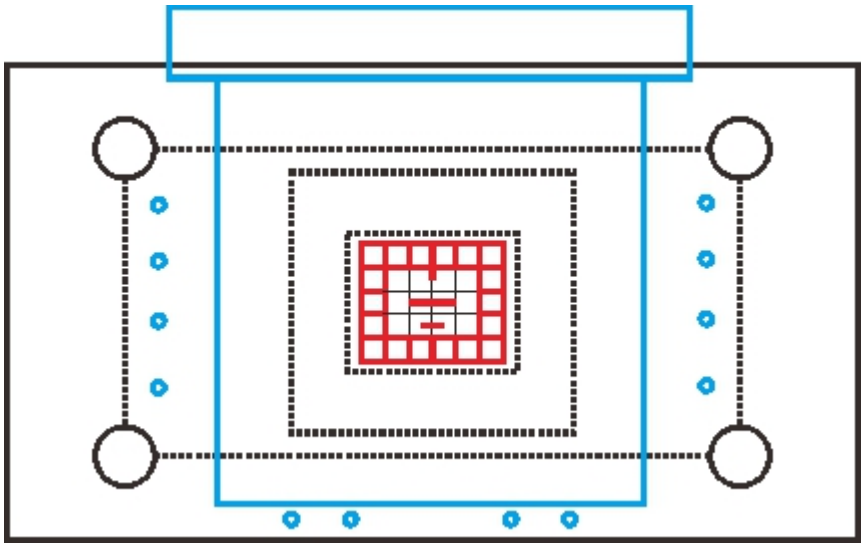

Figure 5.5 Transparent plastic plate with reference pattern for localization of the fluorescence field-of-view on the window chamber tissue. The blue drawing delineates the location of the window chamber; the black circles are the mounting sites of the transparent plastic plate onto the window chamber; the dashed line rectangles from outside to the inside denote an auxiliary circuit for the green circle location, the opening area of the window chamber adapter, and the FOV of the fluorescence microscopy with an objective lens of 1.25, separately; the red lines are used for locating the imaging area of the tumor, each square has an area of 1 mm × 1 mm.

5.7. Data processing

All the primary data from different imaging modalities were converted to RAW files, which were subsequently imported to PMOD (PMOD technologies ltd, Zürich, Switzerland) according to the image resolution, image store size, and the digital form of image data storage. All the imported imaging data was saved as NIfTl file (image suffix, .nii) for further data analysis in PMOD. For the images co-registration, the MRI image was set as the default image, and all the other modalities images were aligned with the MRI anatomy images using the fiducial markers of the window chamber. The transformation information of the co-registration was saved. All the co-registration data of the tumor microenvironment in window chamber was integrated for analysis.

1. Gaustad JV, Brurberg KG, Simonsen TG, Mollatt CS, Rofstad EK. Tumor vascularity assessed by magnetic resonance imaging and intravital microscopy imaging. *Neoplasia.* 2008;10:354-362.
2. Marchal F, Tran N, Marchal S, et al. Development of an HT29 liver metastases model in nude rats. *Oncol Rep.* 2005;14:1203-1207.
3. Vogel I, Shen Y, Soeth E, et al. A human carcinoma model in athymic rats reflecting solid and disseminated colorectal metastases. *Langenbecks Arch Surg.* 1998;383:466-473.
4. Papenfuss HD, Gross JF, Intaglietta M, Treese FA. A transparent access chamber for the rat dorsal skin fold. *Microvasc Res.* 1979;18:311-318.
5. Laschke MW, Vollmar B, Menger MD. The dorsal skinfold chamber: window into the dynamic interaction of biomaterials with their surrounding host tissue. *Eur Cell Mater.* 2011;22:147-164.
6. Palmer GM, Fontanella AN, Shan S, Dewhirst MW. High-resolution in vivo imaging of fluorescent proteins using window chamber models. *Methods Mol Biol.* 2012;872:31-50.
7. Gregory MP, Andrew NF, Siqing S, et al. In vivo optical molecular imaging and analysis in mice using dorsal window chamber models applied to hypoxia, vasculature and fluorescent reporters. *Nat Protoc.* 2011;6:1355-1366.
8. Henke J, Baumgartner C, Roltgen I, Eberspacher E, Erhardt W. Anaesthesia with midazolam/medetomidine/fentanyl in chinchillas (Chinchilla lanigera) compared to anaesthesia with xylazine/ketamine and medetomidine/ketamine. *J Vet Med A Physiol Pathol Clin Med.* 2004;51:259-264.
9. Tomayko MM, Reynolds CP. Determination of subcutaneous tumor size in athymic (nude) mice. *Cancer Chemother Pharmacol.* 1989;24:148-154.
10. Tschiersch H, Liebsch G, Stangelmayer A, Brisjuk L, Rolletschek H. *Microsensors*; 2011.

6. Results for Multimodal Intravital Molecular Imaging System

In the following sections, the images of the MRI imaging, positron imaging, fluorescence imaging and *in vitro* histological staining were from the same rat, while the luminance oxygen sensor image was from a different rat as the imaging modality was added in the late development of this work. In sections 6.1 to 6.5, each imaging modality is addressed in detail to show the feasibility of the imaging method separately. In section 6.5, the information from multimodal imaging modalities of the same animal was integrated and compared.

6.1. MRI imaging

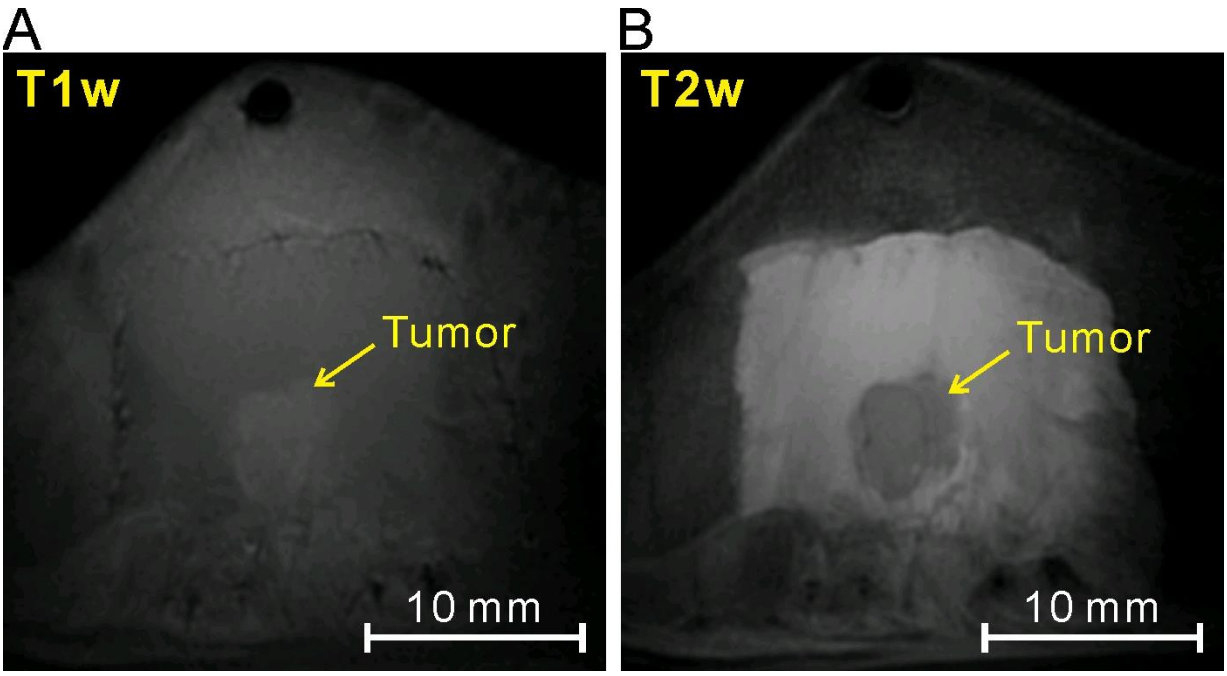

Figure 6.1 T1 weighted (A) and T2 weighted (B) MRI images of the window chamber.

T1 and T2 weighted MRI images of the slice number 14 on a tumor in the window chamber are compared in Figure 6.1. From both images, the tumor can be easily distinguished from the surrounding tissues. The tumor in the T1 weighted image was brighter compared with the surrounding tissue, and darker in the T2 weighted image. The tumor area is 6.14 mm × 4.91 mm in length and width, respectively. Here, the original MRI FOV was 4 cm × 4 cm, and only the

window chamber area is cropped. The spatial resolution of the image was 156 μm. The structure and profile of the window chamber can be distinguished from both images.

6.2. Positron imaging

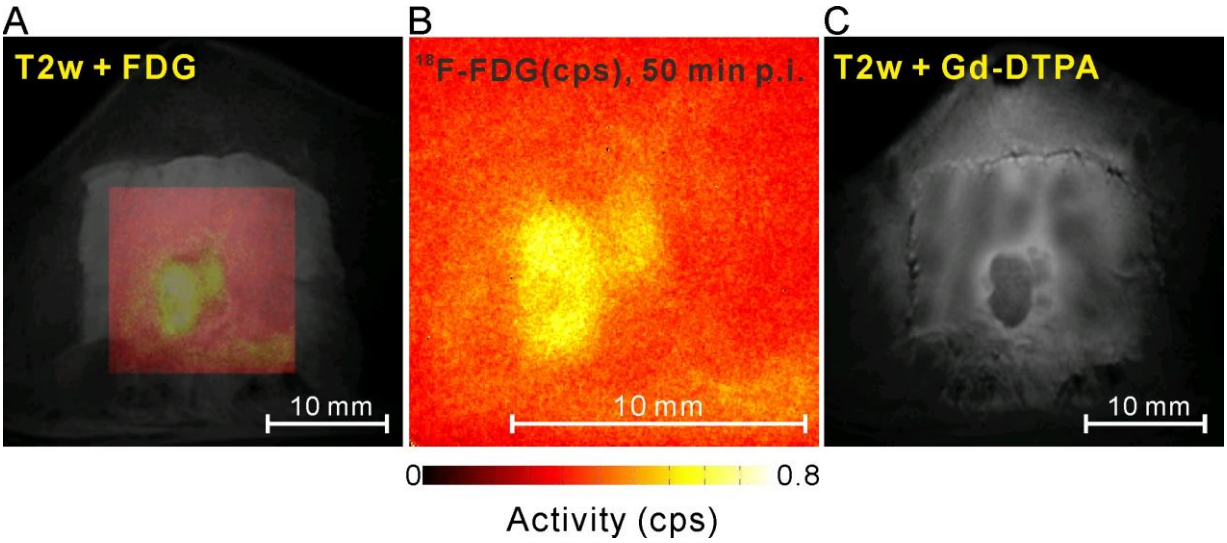

Figure 6.2 Positron imaging of the window chamber: (A) a merged image of the T2 weighted MRI image and ^{18}F-FDG uptake map of the positron image; (B) an ^{18}F-FDG map imaged 50 minutes after the ^{18}F-FDG injection, and the color bar beneath indicates color range versus radioactivity in counts per second (cps); (C) a T2 weighted MRI image after the contrast agent Gd-DTPA injection.

The ^{18}F-FDG uptake map from positron imaging was precisely located onto the T2 weighted MRI image (see Figure 6.2A) with the aid of the four fixation pins (fiducial markers) on the window chamber. The location of the positron image is always fixed with reference to the four fixation pins, as the positron camera is mounted onto the window chamber with four holes around its detector. The ^{18}F-FDG uptake of the tumor was obviously higher than the surrounding tissue, which confirms the Warburg effect of increased glucose uptake in tumors. Not all the tumor area depicted here has a higher ^{18}F-FDG uptake, which is because the signal of the positron image comes more from the surface of the tumor, and the MRI image was from a slice not very close to the surface of the tumor. An MRI image more close to the surface of the tumor is shown in Figure 6.3C. The anatomy of the tumor structure was much clearer after the contrast agent injection. From the positron imaging (see Figure 6.2B), the tumor had higher ^{18}F-FDG uptake than the surrounding tissue. The image was an averaged map from a 10 minutes measurement.

6.3. Luminance oxygen sensor imaging

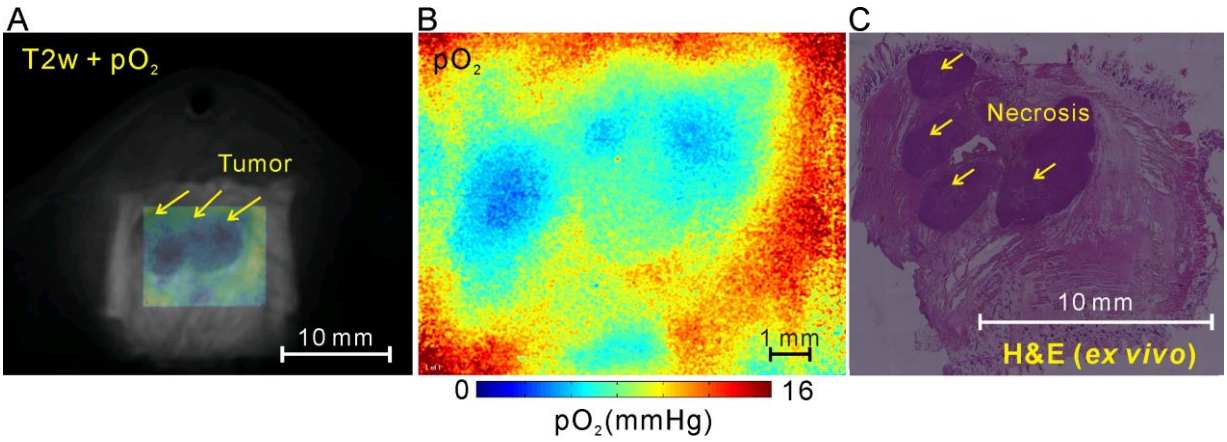

Figure 6.3 Luminance oxygen sensor imaging of the window chamber, note that these images are from a different rat: (A) a merged image of a T2 weighted MRI image and an oxygen map of the luminance sensor image, yellow arrows denote the tumor blocks; (B) the oxygen map of the window chamber, the color bar beneath indicates color range versus pO_2 in mmHg; (C) a H&E staining slice of the tumor and periphery tissues in the window area, which gives confirmation information of the tumor and surrounding tissues located approximately in the window chamber area, note that the image cannot be precisely compared with the *in vivo* images here.

The luminance oxygen sensor map was precisely located on a T2 weighted MRI image of a window chamber (see Figure 6.3A). The co-registration was accomplished with the aid of the luminance sensor adapter that connected the window chamber with the luminance sensor. The merged image indicates that the tumor area has lower oxygen levels compared to the surrounding tissue. The tumor blocks depicted with yellow arrows on the T2 weighted image are darker than the surrounding tissue. The diameter of the largest tumor block is 10.34 mm. The tumor surface pO_2 of the window chamber was measured with the luminance oxygen sensor. The oxygen partial pressure map in mmHg is shown in Figure 6.3B. From the color bar, the area in blue depicts lower oxygen levels while the area in yellow to red denotes higher oxygen levels. Note that the oxygen map was scaled to show a gradient change around the tumor blocks. The centers of the tumor blocks have the lowest oxygen levels. The histological staining of the tissue in the window chamber area is shown in the Figure 6.3C, confirming the tumor blocks' locations.

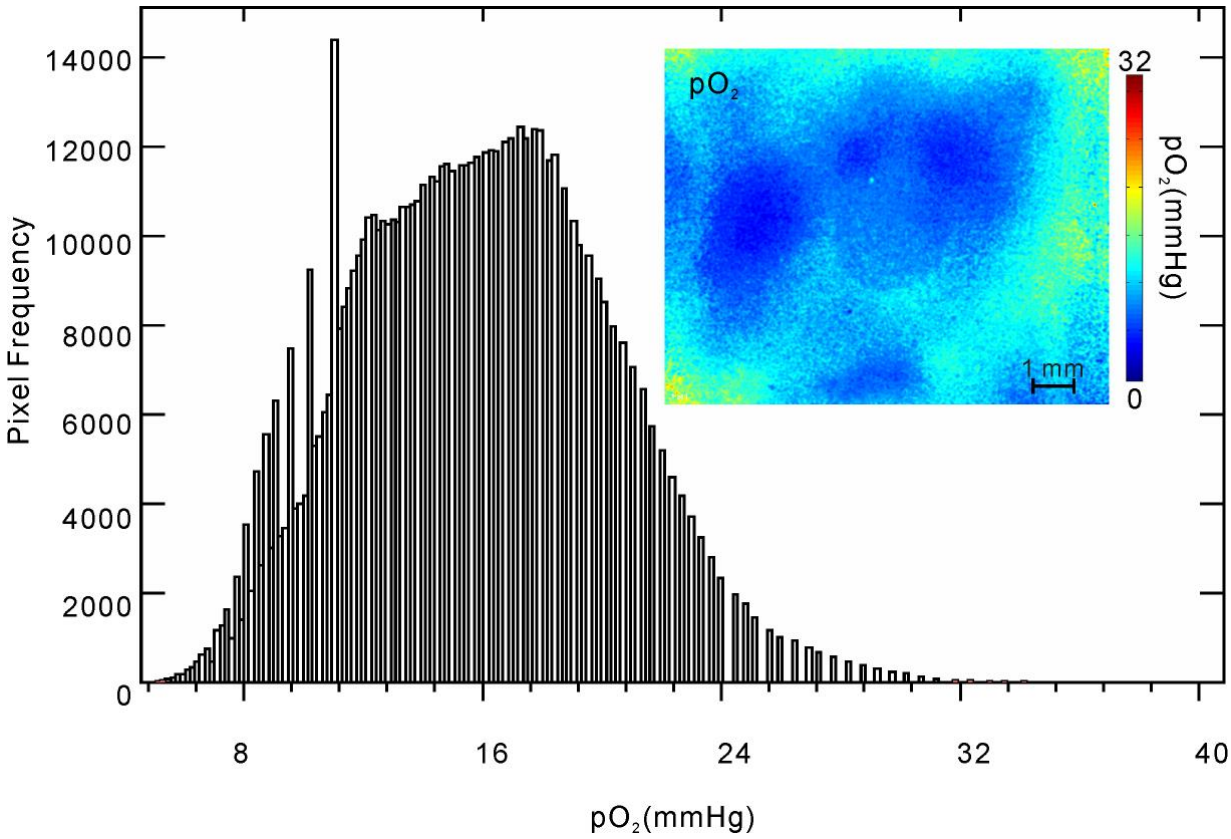

Figure 6.4 Luminance oxygen sensor image and its pixel-pO_2 histogram. The color bar indicates color range versus pO_2.

The luminance oxygen sensor image is shown in Figure 6.4, along with its pixel-pO_2 histogram. The pO_2 frequency of the whole oxygen map is shown in the histogram, which was drawn using a software called VisiSens AnalytiCal 1 from the oxygen sensor company, and the unit of the pO_2 was converted from the [%] air saturation into the mmHg. The tumor areas in the oxygen map have an average of 11.67 mmHg, a maximum of 20.99 mmHg and a minimum of 4.67 mmHg. The necrosis area has an average of 7.46 mmHg, a maximum of 10.73 mmHg and a minimum of 4.67 mmHg. The whole FOV of the oxygen map has an average of 14.62 mmHg, maximum of 39.19 mmHg, and a minimum of 4.67 mmHg. So the surrounding tissue has an average of 17.07 mmHg.

6.4. Fluorescence imaging

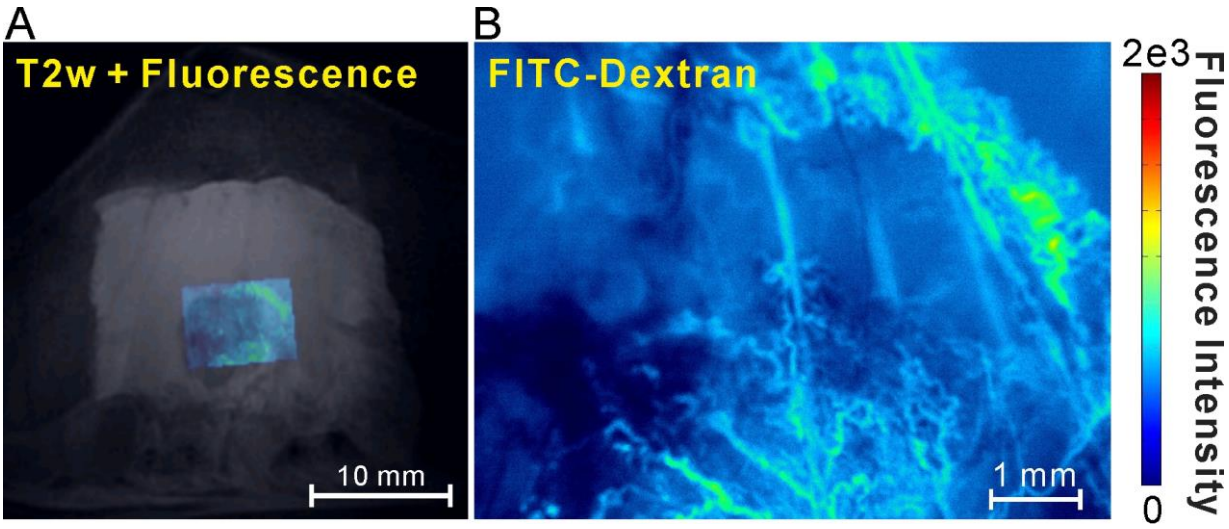

Figure 6.5 Fluorescence imaging of the window chamber: (A) a merged image of the T2 weighted MRI image and a fluorescence image with FITC-dextran (mw: 2e6, 250mg/kg); (B) a fluorescence FITC-Dextran image of the window chamber to visualize the blood vasculature around the tumor tissue. The color bar indicates color range versus fluorescence intensity.

The location of the FITC-dextran fluorescence image is shown in the T2 weighted MRI image of the window chamber (see Figure 6.5A). The precise co-registration was accomplished with the aid of the transparent plastic plate with reference pattern (refer to Figure 5.6). From the merged image, the microvessels around the tumor are non-homogenous. Some areas were highly vascularized, some areas in adjacent were poorly vascularized, and more blood vessels were condensed around the tumor edges. The FITC-dextran fluorescence image of the FOV is shown in Figure 6.5B. The fluorescence intensity was condensed in the larger blood vessels. The resolution of the fluorescence image was 5.16 µm.

6.5. *In vitro* histological staining

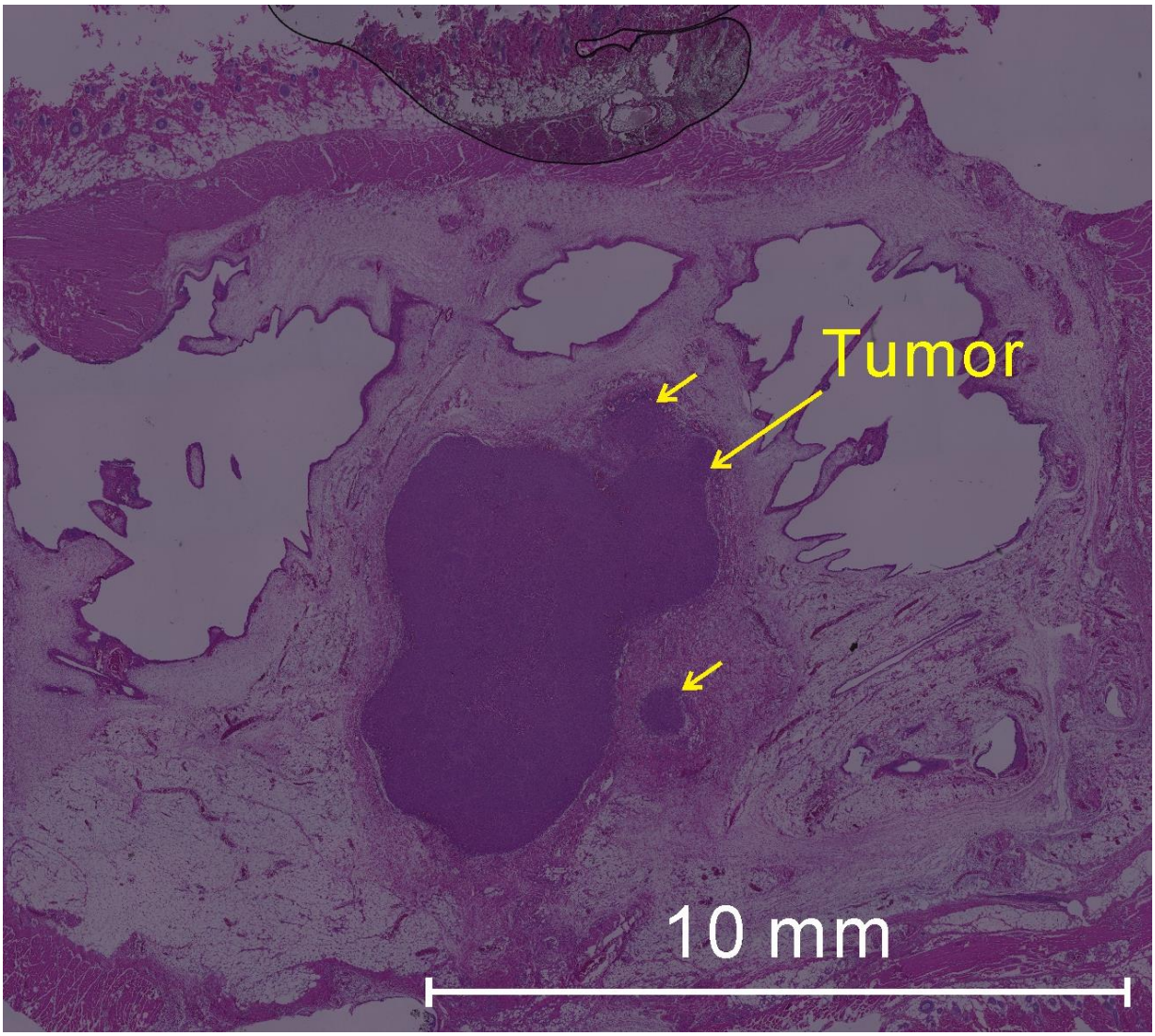

Figure 6.6 H&E staining of the tissue sample taken from the window chamber area after the sacrifice of the rat. Yellow arrows depict the tumor locations in the tissue.

The H&E staining of the tissue in the window chamber is shown in Figure 6.6. The whole tissue section was recorded by combing each microscopy FOV of the tissue section. The areas condensed with purple color depict the tumor tissues. From the H&E staining image, three tumor blocks can be visualized. The biggest tumor block is 6.11 mm × 4.84 mm in length and width, and the two smaller ones with diameters of about 0.7-0.8 mm.

6.6. Integrated tumor microenvironment imaging

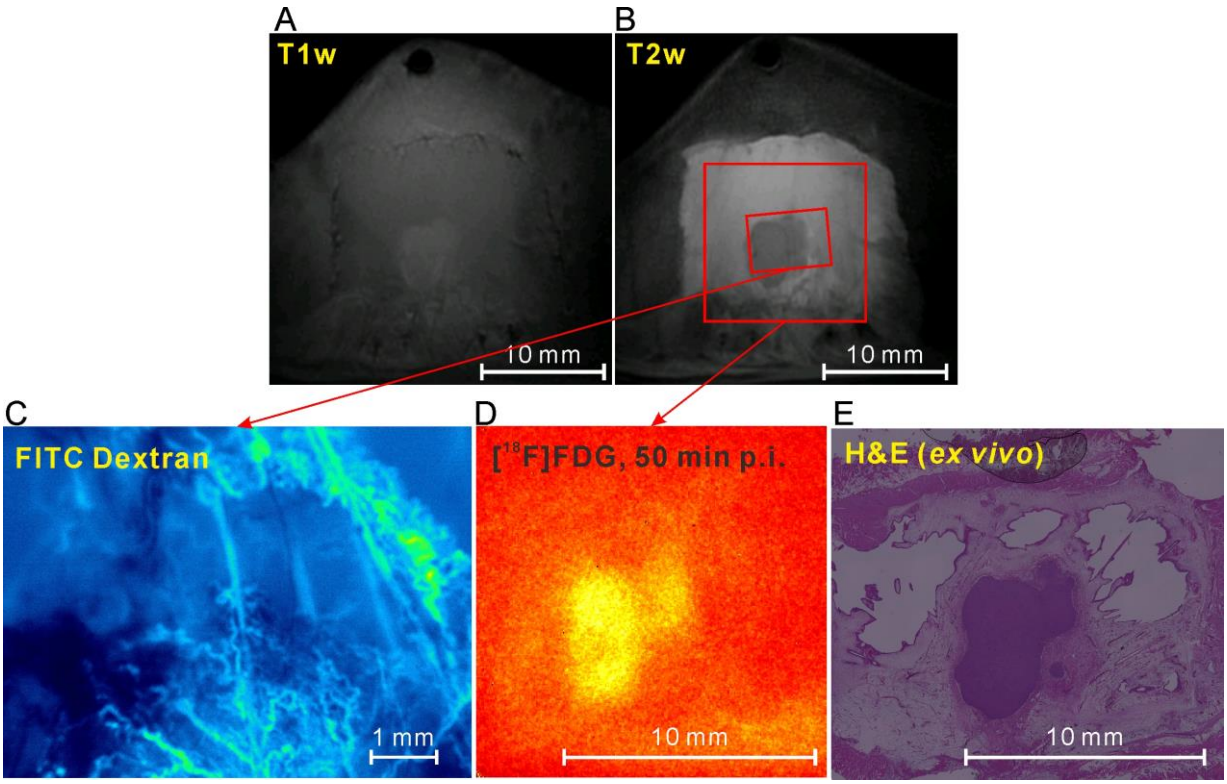

Figure 6.7 Multimodal intravital imaging of a tumor microenvironment within the window chamber: (A) a T1 weighted MR image, (B) a T2 weighted MR image, (C) a FITC-Dextran fluorescence image, (D) an ^{18}F-FDG positron image, the locations of the images were delineated with the red boxes linked with red arrows separately; and (E) a H&E staining slice of the tumor and periphery tissue. Note that the H&E image is an *ex vivo* image, only gives confirmation of the location of the tumor and surrounding tissue, and cannot be precisely compared with the *in vivo* images listed here.

Multimodal intravital imaging of a tumor in the window chamber was integrated to provide various information about the tumor microenvironment (see Figure 6.7). The tumor tissue was darker than the surrounding tissue in the T2 weighted map, whereas whiter in the T1 weighted map. The H&E staining image confirmed the location and shape of the tumor. The FITC-dextran fluorescence image of a smaller FOV inside the tumor showed a detailed blood vessel network in micrometer range. The complexity of the tumor network shown in the fluorescence was consistent with the MRI observation. The positron imaging map showed that the ^{18}F-FDG is accumulated and trapped inside the tumor area, which is consistent with the Warburg effect.

7. Discussion for Multimodal Intravital Molecular Imaging System

As the preliminary study with the MIMI system is in an establishment stage, more details of the discussion will be focused on the methods and techniques of the system.

7.1. Implantation with multimodal compatible window chamber

The design of the final version of the multimodal compatible window chamber went through two versions' update during development, and the second version was patented [*1*]. The second version of the window chamber has minimal invasiveness to the rat as the fixation of the window chamber plates do not penetrate the tissues, however, the clamp way of the fixation design is not as friendly as expected to the animal. The rat with the window chamber showed unbearable behaviors two or three weeks after the implantation, such as bites and clawing, trying to get rid of the window chamber. This is because the tight fixation hinders the blood flow of the tissues in between, especially when the animal grows larger and furs grow thicker. Besides, the extruded fixation part of the window chamber sometimes hinders the animal from free moving, and the animal may be stuck into a food shelf in the cage. Thus, the window chamber has position shifts over time, and could not attain the purpose of accurate co-registration of images obtained over days and weeks. The latest version fixed this problem with a fixation using three screws penetrating the rat skin tissue, and the stability is much improved. Furthermore, the dimension is reduced. The rat carrying the window chamber can move freely in the cage. Thus, the window chamber showed better ergonomics.

The suture's position and tightness of the window chamber are the key for a successful implantation. Although there are many suture sites designed on the window chamber, not all the suture sites are required. If all the suture sites are sewed, the blood flow of the tissue inside the window will be hindered, leading to edema around the window area and tissue inflammation and necrosis. Thus, tumor cells cannot be successfully transplanted. As noted in chapter 5.2.1, only the sites at the bottom of the window are required to be sewed to avoid the bottom skin being stretched away from the window area. And the suture is not supposed to be very tight to ensure a well perfused blood flow.

The window of the chamber is designed with a rectangular shape, instead of the conventional round shapes [*2*]. This is necessary to fix the positron camera for a close contact imaging position. The window chamber can be mounted onto the positron camera, a mini optical sensor and

microscopes with the fixation pins (fiducial marker) and the window chamber assisting adapter. The physical fiducial marker allows direct and precise co-registration of images from the above mentioned imaging modalities plus MRI and PET.

7.2. Animal tumor model

There is an alternative way to perform the window chamber implantation and tumor transplantation in compare to literatures [*3-6*]. Normally, window chamber is implanted first and after 3 days, a tumor is transplanted either with a tumor tissue block or tumor cells suspension. Alternatively, the sequence can be performed reversely. The tumor cells suspension is first injected in the dorsal skin layer of the rat, and the injection site is where the window of the window chamber will be placed. In this way, not only the time for a rat bearing the window chamber is shortened, but also a highly successful rate of the tumor transplantation is ensured. For the HT-29 tumor cell line, the tumor is then measured from the day 4, when the tumor is visible. The window chamber is implanted when the tumor grows to the required size. During the operation, the skin layer without tumor will be cut and excluded, the tumor tissue inside the window chamber should kept as intact as possible, and the blood vessels in the fascia should be carefully preserved. In the early time after surgery, regular checking to stop bleeding and cleaning of the screening liquids are necessary.

7.3. MRI imaging

The preclinical MRI imaging has a spatial resolution of around 100 µm. Most of the anatomical structures of the tumor and surrounding tissue can be clearly distinguished, as shown in the T1 and T2 weighted images. This is important for the multimodal imaging, because the fiducial markers on the window chamber can be precisely located. Furthermore, the MRI images have the largest FOV (4 cm × 4 cm) compared with other imaging modalities applied, and all the information of the window chamber can be collected up. In addition, the MRI imaging is a 3D imaging technique, and the MRI slice in the Z direction can be located. Thus, T1 and T2 weighted images are set as the default images for the image co-registration.

7.4. Positron imaging

Positron imaging is mainly based on contact imaging. However, the tumor inside the window is not a real flat plane as tumor grows in 3D direction. Thus, the contact between the tumor surface and the detector plane of the positron camera could be uneven, especially when the tumor

volume grows larger. This is a challenge for the detection as the positron imaging is very sensitive to the imaging distance [*7*]. The closer the tissue approaches to the detector of the positron camera, the more enhanced position signal is detected. Besides, the breathing of the animal may lead to a variation in the distance between the positron camera and the window chamber. Thus, it is crucial to have a fixation setting to ensure an even and stable contact between the tissue plane and the positron camera. Here, the window chamber and the window chamber assisting plate was mounted onto a fixation stage, which reduces the vibration from the animal breathing. And to avoid the liquids screened from the tissue destroying the positron camera, it is suggested to place the positron camera on top of the window chamber. In further, a layer of Mylar foil (6-µm-thick) was placed in-between to protect the positron camera. The tumor uptake of the ^{18}F-FDG was visible with exposures of 8 seconds, which is consistent with the results reported by Zhonglin Liu et al. [*8*]. However, in the averaged image (the cps map) of the 10 minutes' measurements, the microvessels of the tumor are still not distinguishable.

In the method description, a dynamic positron imaging protocol is proposed, which is useful for kinetic modeling analysis to elucidate the underlying pharmacokinetics. However, it is very hard to extract the blood input function (the time course radioactivity of the tracer in blood) of the dynamic positron imaging since the arterioles cannot be distinguished from the positron images. Hence, the quantitative analysis and kinetic modeling are not applicable yet, unless the blood input function of the tracer can be captured. One possible solution is to perform a dynamic PET imaging, where the heart or aorta of the rat is used to access the blood input function. By using the same administration program with a syringe pump, the blood input function is transferable from the dynamic PET into the dynamic positron imaging approximately. In total, an average of six measurements should be enough for the assessment. The second way to measure the blood input function of the animal can be performed with the aid of a tubing that connecting the femoral artery of the rat with the femoral vein, where the radioactivity of the circulation blood can be measured with a detect machine. However, there are a lot of technological and animal welfare issues to be solved for this method. A simple and maybe effective solution is to perform the positron imaging and PET measurement simultaneously, using the same pump administration protocol. In this way, only a single tracer injection is needed, and both, the positron imaging of the window chamber, and the PET imaging focusing on the heart can be performed. Unfortunately, this is not yet feasible with the current setting of the window chamber and the size of the positron camera, which cannot be accommodated into the field-of-view of a preclinical PET scanner. Furthermore, the camera located inside the PET scanner may hinder part of the signal acquisition of the rat, introducing a problem for the image reconstruction of the PET data.

7.5. Luminance oxygen sensor imaging

The oxygen sensor foil can be used either with or without peeling off the protection layer. From the technical note of the company, the imaging resolution is increased from 100 µm to 25 µm when the protection layer is peeled off. However, when the protection layer is kept, the reproducibility of the measurement was better from our test experiments. This is because the sensitivity of the measurement was much increased along with the increased imaging resolution. Since the tumor and the surrounding tissue inside the window area is not an absolute flat plane, the increased sensitivity may introduce more noise than the real signal, especially when the tumor grows larger in a 3D direction way. Thus, the protection layer of the oxygen sensor foil was kept during the measurements.

The pO_2 value of the luminance oxygen sensor image is determined with the calibration of the surrounding oxygen levels in air and oxygen free values. So the detection and calibration should be performed under the same environment and with the same detection setting. Although the adapter of the luminance oxygen sensor shadows the surrounding light away, it is still important to avoid the daylight or room light during the calibration and measurement, ensuring a stable measurement conditions all the time. Before each measurement, it is necessary to initiate the oxygen sensor for an auto adjustment of the sensor itself.

The oxygen partial pressure of the air is considered to be 160 mmHg at the sea level and at room temperature, which equals to 21.1% of the oxygen in the air [*9*]. Here, the partial pressure in Munich is considered to be 155.5 mmHg for 21.1% oxygen in the air, which is a converter factor suggested from the sensor company. The tumor has an average of 11.67 mmHg pO_2 value measured from the oxygen map. The critical pO_2 in tumors is proposed to be 8-10 mmHg [*10*]. However, there is strong inter-tumor variability of the oxygenation pattern from different tumor samples. The averaged mean pO_2 was ranging from 13 to 59 mmHg in a breast cancer study measured with an oxygen electrode method [*11*], and the median pO_2 was ranging from 0 to 54 mmHg with 28 tumor samples measurements [15]. Apart from an absolute comparison of tumor pO_2 values, pO_2 value is always lower in the tumor than in the respective normal tissue, which is the true definition of hypoxia [*12*]. Here, the pO_2 of the surrounding tissue has an average of 17.07 mmHg, 5.4 mmHg higher than the tumor tissue. The tumor necrosis area that was proved from the HE staining shows an averaged pO_2 value of 7.46 mmHg, and the lowest value of 4.67 mmHg, which is consistent with the observation that the pO_2 value lower than 8 mmHg has detrimental changes of tumors (ATP depletion, intracellular acidosis, apoptosis…) [*12*].

The tumor measured in a window chamber with the oxygen sensor is a special situation, since the tumor is in the sub-cutis layer of the skinfold on the rat. In a study of human skin pO_2

measurement with microelectrodes, the pO_2 increased with the increase of the depth of the skin, the pO_2 was 8.0 ± 3.2 mmHg in the superficial region of the skin (5-10 μm), the pO_2 was 24.0 ± 6.4 mmHg in dermal papillae (45-65 μm), and the pO_2 was 35.2 ± 8.0 mmHg at the surface of the sub-papillary plexus (100-120 μm) [*9*]. So the way of contact imaging of the skin layers may also affect the measured pO_2 values, which is confirmed by pioneer studies with a rat window chamber [*13*]. They proved that there are significant differences of the pO_2 values between fascial and tumor surfaces [*13*]. The tumor pO_2 map was measured with phosphorescence lifetime imaging using a Pd-meso-tetra-(4-carboxyphenyl)-porphyrin [*13-15*]. The luminance oxygen sensor foil applied in our study is also a similar porphyrin product, however, has a contact on the surface of the tumor tissue. As the fascia layer is closely connected with the tumor surface, the measured signal is a combination of the fascia layer and the tumor surface. Our averaged pO_2 data cannot be directly compared to the median pO_2 values presented in those studies, however, the pO_2 range in the studies is broader than ours [*13,15*]. This is in consistent to the decreased sensitivity in the measurement without peeling off the protection layer of the oxygen sensor foil.

7.6. Fluorescence imaging

Fluorescence imaging has the highest resolution but the smallest imaging field-of-view compared to other imaging modalities, introducing a challenge for the images co-registration. The coordinate of the microscopic image cannot be precisely located only with the fiducial markers of the window chamber. Here, the introduction of the transparent plastic plate solved this problem. It has a connection with both microscopy imaging and fiducial markers of the window chamber, so that the field-of-view of the microscopy is orientable in the window chamber. Furthermore, the microscopically differentiable pattern of the transparent plastic plate supplies reference of the length and orientation, assisting the localization of the tumor in the window chamber. The stable fixation of the window chamber onto the microscopy was accomplished with the aid of the window chamber assisting adapter, a plastic base and a large clamp. The whole setting also ensured the skin fold tissue inside the window chamber to be parallel to the lens of the microscopy, avoiding a blurred image.

7.7. Multi-modality imaging

The multi-modal imaging gives various information about the same tumor microenvironment, however, there are biological and technical issues to be considered. First, the animal goes under anesthesia in every single imaging modality measurement. It takes 10 minutes for the luminesce

oxygen sensor imaging, 1h for the MR imaging, 20 minutes for the positron imaging, and 45 minutes for the fluorescence imaging. The total anesthesia time will be a burden for the animal if these four or more imaging modalities are performed together. Spreading the imaging into different days gives the animal certain recovery time, but in contradiction, the images from different days or weeks may not be comparable. Thus, it is important to appropriately arrange the imaging time and sequences. Here we propose an integrated imaging protocol in consideration of both animal welfare and the effectiveness of each imaging modality for comparison. The MRI imaging is scheduled first and will take 45 to 60 minutes with isoflurane anesthesia. In following, the luminance oxygen sensor imaging is scheduled immediately, which takes 10 minutes. Afterwards, the animal will be waken up for resting and recovery for about 2 hours, in a cage with heating pad underneath and an oxygen flow supply. Then, the rat is anesthetized with MMF to perform fluorescence imaging which costs about 45 minutes, followed by 1-hour recovery. Last, the positron imaging is set with isoflurane anesthesia. The rat will go under 10 minutes' anesthesia for the tracer injection, then awake for 40 minutes for resting, and then 10 minutes' anesthesia for the positron imaging acquisition. Afterwards, if the rat is sacrificed, the tissue inside the window chamber will be cut and kept into a 4% para-formalin solution for further immunohistochemistry operations. Second, the orientation and coordinate for image co-registration have to be considered. The application of several tools, such as the window chamber assisting plate, luminance sensor adapter, and the transparent plastic plate, aided the co-registration in different aspects. The details were discussed separately in each section. Some pattern with orientation information can be added onto the next generation window chamber, making it easier to find the anatomical orientation among different images from the multimodality imaging.

1. Shi K, Liu Z, Ziegler SI, Schwaiger M, Shi K, Liu Z, Ziegler SI, Schwaiger MShi K, Liu Z, Ziegler SI, Schwaiger Ms; US 20140121493 A1, assignee. System and Apparatus for Multimodality-compatible High-quality Intravital Radionuclide Imaging, 2014.
2. Hak S, Reitan NK, Haraldseth O, Davies CD. Intravital microscopy in window chambers: a unique tool to study tumor angiogenesis and delivery of nanoparticles. *Angiogenesis.* 2010;13:113-130.
3. Papenfuss HD, Gross JF, Intaglietta M, Treese FA. A transparent access chamber for the rat dorsal skin fold. *Microvasc Res.* 1979;18:311-318.
4. Laschke MW, Vollmar B, Menger MD. The dorsal skinfold chamber: window into the dynamic interaction of biomaterials with their surrounding host tissue. *Eur Cell Mater.* 2011;22:147-164.
5. Palmer GM, Fontanella AN, Shan S, Dewhirst MW. High-resolution in vivo imaging of fluorescent proteins using window chamber models. *Methods Mol Biol.* 2012;872:31-50.
6. Gregory MP, Andrew NF, Siqing S, et al. In vivo optical molecular imaging and analysis in mice using dorsal window chamber models applied to hypoxia, vasculature and fluorescent reporters. *Nat Protoc.* 2011;6:1355-1366.
7. Wang Q, Tous J, Liu Z, Ziegler S, Shi K. Evaluation of Timepix silicon detector for the detection of 18F positrons. *J Instrument.* 2014;9:C05067.
8. Liu Z, Chen L, Barber C, et al. Direct positron and electron imaging of tumor metabolism and angiogenesis in a mouse window chamber model. *JNM Meeting Abstracts.* 2012;53:1146.
9. Wang W, Winlove CP, Michel CC. Oxygen partial pressure in outer layers of skin of human finger nail folds. *J Physiol.* 2003;549:855-863.
10. Höckel M, Vaupel P. Biological consequences of tumor hypoxia. *Semin Oncol.* 2001;28:36-41.
11. Hohenberger P, Felgner C, Haensch W, Schlag PM. Tumor oxygenation correlates with molecular growth determinants in breast cancer. *Breast Cancer Res Treat.* 1998;48:97-106.
12. Carreau A, El Hafny-Rahbi B, Matejuk A, Grillon C, Kieda C. Why is the partial oxygen pressure of human tissues a crucial parameter? Small molecules and hypoxia. *J Cell Mol Med.* 2011;15:1239-1253.
13. Erickson K, Braun RD, Yu D, et al. Effect of Longitudinal Oxygen Gradients on Effectiveness of Manipulation of Tumor Oxygenation. *Cancer Res.* 2003;63:4705-4712.
14. Dewhirst MW, Ong ET, Braun RD, et al. Quantification of longitudinal tissue pO2 gradients in window chamber tumours: impact on tumour hypoxia. *Brit J Cancer.* 1999;79:1717-1722.
15. Cárdenas-Navia LI, Mace D, Richardson RA, Wilson DF, Shan S, Dewhirst MW. The Pervasive Presence of Fluctuating Oxygenation in Tumors. *Cancer Res.* 2008;68:5812-5819.

8. Summary

Molecular imaging has been extensively used to investigate tumor metabolism and the tumor microenvironment. However, systematic linking of the imaging with the tumor physiology is still limited, due to the complexity of tumor metabolism and the heterogeneity of the tumor microenvironment. This thesis makes the following contributions in new methodological developments: (I) a novel imaging method and system (CIMR system) is developed for tumor cells' metabolism *in vitro*, which can be extended to investigate the interactions between a radiolabeled molecule and the cells; (II) a novel multimodal intravital molecular imaging system and method (MIMI system) is developed for measuring physiological features of tumor microenvironment *in vivo*.

The CIMR system provides an innovative imaging method that imaging in a fluids infusion condition, in which a medium chamber and a cell chamber were imaged simultaneously to extract the real-time uptake of the radioactive tracer for adherent cells. Cellular pharmacokinetic modeling can be achieved based on the dynamic measurements. The estimated cellular kinetic parameters were verified by comparing with the mRNA expression levels. In particular, the developed CIMR system has the following methodological contributions:

- For the first time, an in-culture continuous measurement system was developed to online imaging the uptake signals of radioactive tracer with minimum disruption and easy operation
- A high-resolution positron camera based on single-particle counting silicon pixel detector Timepix was proposed to obtain high-quality measurements of radioactive signals.
- A method was developed to distinguish the medium signal and the cellular uptake signal via simultaneously recording an additional reference medium chamber during infusion.
- A cellular compartmental model was introduced to estimate the underlying pharmacokinetics.
- A mathematical model was developed to correct the delay and dispersion of radio activities between the medium chamber and cell chamber.
- A depth-dependent sensitivity correction method was developed to compensate the influence of distance to the detector on the imaging sensitivities.
- A cell counting method for microfluidic chip was selected after exploring different strategies to achieve a robust and precise measurement of small cell population (~10^4) with smallest variation and highest precision.

The initial experiments demonstrated the reproducibility, stability and feasibility of capturing pharmacokinetic differences of the CIMR system. It provides a platform for convenient quantitative investigation of cellular physiology and pharmacokinetics.

The easy and robust in-culture real-time measurements of the developed CIMR system provides the potential for several applications for future work:

- Several other tracers and cell lines may be investigated. For example, the clearance of amino acid tracer ^{18}F-fluoroethyl-L-tyrosine (^{18}F-FET) in malignant glioma cells can be investigated in-depth by the system.
- The CIMR system may be further extended by integrated with other monitoring methods such as florescence microscopy or luminescence sensor imaging.
- The real-time monitoring of cellular changes with drug interventions may be achieved by advanced modeling on the online measurement data.
- More complex topology of fluid paths and chambers can be extended to simulate vessel network and organ interactions to investigate advanced pharmacokinetics and pharmacodynamics.

The MIMI system provides an imaging tool combining four imaging modalities (positron imaging, MRI, fluorescence imaging and luminescence sensor imaging). The accurate co-registration of images among the imaging modalities ensures a comprehensive understanding of the tumor microenvironment. This system can bridge the discrepancies between macroscopic and microscopic images and between *in vivo* and *in vitro* images and provides a tool for the regional investigation and longitudinal observation of underlying physiology within an intact tumor tissue. Several methodological contributions have been made during the development of this system:

- A special dorsal skin chamber was designed to provide a dedicated window for the investigated multimodal imaging.
- A tumor model was investigated and prepared for intravital investigation.
- Special biocompatible materials for window chamber was investigated and selected for robust and multimodal compatible imaging.
- A particular fiducial coordination system was developed to allow precise physical co-registration among different imaging modalities.
- A dedicated positron imaging protocol was established for Timepix detector.

The preliminary test results demonstrated that the dorsal skin window chamber tumor model was feasible for multimodal intravital imaging. The multimodal imaging provided rich

information about the tumor microenvironment, which may be useful to investigate the physiological principles of molecular imaging as well as efficient drug screening with in-depth knowledge of underlying changes of tumor microenvironment.

List of Abbreviations

^{18}F-FDG	2-Deoxy-2-(^{18}F)fluoro-D-glucose
^{18}F-FET	^{18}F-fluoroethyl-L-tyrosine
AFN	Atipamezole/ flumazenil/naloxone
AIF	Arterial input function
ATP	Adenosine 5´-triphosphate
BLI	Bioluminescence imaging
BST	Blood supply time
CCD	Charged-coupled detector
CIMR	Continuously infused microfluidic radioassay
CLSM	Confocal laser scanning microscopy
CMOS)	Complementary metal oxide semiconductor
$Co(NO_3)_2$	Cobalt nitrate
cps	Counts per second
CT	Computed tomography
DCE-MRI	Dynamic contrast-enhanced magnetic resonance imaging
DNA	Deoxyribonucleic acid
dNTPs	Deoxynucleoside triphosphates
EOF	Electro-osmotic flow
FITC-dextran	Fluorescein isothiocyanate–dextran
FMT	Fluorescence molecular tomography

FOV	Field-of-view
FRI	Fluorescence reflectance imaging
Gd-DTPA	Gadolinium-diethylenetriamine penta-acetic acid
GFP	Green fluorescent protein
GLUT1	Glucose transporter-1
GLUTs	Glucose transporters
H&E	Haematoxylin-eosin
HIF-1	Hypoxia induced factor -1
HK2	Hexokinase-II
HKs	Hexokinase
IVM	Intravital microscopy
LDH	Lactate dehydrogenase
MCT	Monocarboxylate cotransporter
MEMS	Microelectromechanical systems
MIMI	Multimodal intravital molecular imaging
MKL	Math Kernel Library
MMF	Midazolam/medetomidine/fentanyl
MP	Multiphoton
MR	Magnetic resonance
MRA	Magnetic resonance angiography
MRI	Magnetic resonance imaging

mRNA	Messenger ribonucleic acid
MRS	Magnetic resonance spectroscopy
mw	Molecular weight
Na_2SO_3	Sodium sulfite
NEX	Number of excitation
NIR	Near-infrared
OFDI	Optical frequency domain imaging
PCR	Polymerase chain reaction
PD	Pharmacodynamics
PDMS	Polydimethylsiloxane
PEEK	Polyetheretherketone
PET	Positron emission tomography
p.i.	post injection
PK	Pharmacokinetics
PLI	Phosphorescence life time imaging
pO_2	Oxygen partial pressure
PSAPD	Position sensitive avalanche photodiode
qPCR	Quantitative real-time polymerase chain reaction
RNA	Ribonucleic acid
s.c.	Subcutaneously
SPECT	Single photon emission computed tomography

TACs	Time activity curves
TRICKS	Time-resolved imaging of contrast kinetics
μ-TASs	Micro total analytical systems

Acknowledgements

I would like to thank my supervisor Prof. Dr. Sibylle Ziegler for giving me the opportunity to do my PhD research in her lab and always support for my PhD project. She always tries to make time to solve my problems no matter how busy she is. Whenever I have difficulties, she is always by my side. She encourages me to face the difficulties of the project and forgives me of the mistakes I made during the studies. At the same time, her conscientious attitude to the scientific research sets a good example, which leads me to do the research strictly. The rigorous as well as relaxed research atmosphere in her lab allows me to finish my study in a pleasant way. Prof. Dr. Ziegler also fully understands the difficulties I may encounter in daily lives as a foreigner in Germany, and she is always willing to offer a hand, these feelings of warmth will surely become my precious memories for years to come.

I would like to thank for my tutor Dr. Kuangyu Shi's guidance, and I am really appreciated to his support from the provision of software to hardware. Dr. Shi directs me in almost every aspect of the PhD studies. Whenever I have problems in techniques or suffer from bad experimental results, I would turn to him for help, and he would kindly solve them with me together through countless of tries and tests. This thesis would definitely be impossible if without his efforts and dedication. Besides, he also offers me many useful suggestions in the daily life issues. I would like to express my sincere thankfulness to you for all the kindness in both academic and daily routine.

I would like to thank my thesis committee mentors Prof. Dr. Gabriele Multhoff, Prof. Dr. Markus Essler and Prof. Dr. Gil Westmeyer. They provided me with a lot of valuable suggestions, the friendly and relaxed communication are impressive to me and encourages me to fulfill my study.

I would like to thank Prof. Dr. Markus Schwaiger. He is a great leader of prospective vision. Without his support for the devices and other important investments, the PhD project would not happen or proceed so smoothly. His critical viewpoints lead a clear way to the constant upgrade of the systems we are developing. Prof. Dr. Schwaiger allows researchers to try and error in various new technologies and fresh research ideas. And he is lenient to me for the mistakes I made during the exploration of new studies until I made some steps forward. I really appreciate.

I would like to thank Prof. Sung-Cheng (Henry) Huang for his guide and help regarding to the kinetic modeling and the microfluidic system studies in both TUM and UCLA. His conscientious and modest attitude is highly admirable. I would also like to thank Dr. Koon-Pong Wong for the assistance and help for my short time study in UCLA.

I would like to thank co-workers Dr. Qian Wang, Tao Cheng, Ziying Jian for the experiments and data analysis supports. I would like to mention that Tao Cheng and Ziying Jian also helped the second sub-project especially about the optimization of the luminance oxygen sensor imaging protocol and the images co-registration. I would like to thank Dr. Christof Seidl and Dr. Benedikt Feuerecker for helping me translate my English abstract into the German version.

I would like to thank Dr. Geoffrey Topping and Dr. Franz Schilling for setting the MRI acquisition parameters, testing and establishing most of the MRI protocols with me. I would like to thank Stephan Düwel, Christian Hundshammer, Eugen Kubala and Dr. Giorgio Pariani for helping me exploring some MRI imaging protocols and doing some MRI experiment with me. I would like to thank you all for the guide of the MRI knowledge and many useful discussions with me. I would like to thank Aayush Gupta for helping me with some MRI measurements. I would like to thank our MRI technician Michael Michalik for helping of some MRI experiments' preparation.

I would like to sincerely thank Sibylle Reder and Markus Mittelhaeuser for helping of PET and positron measurement. Without their supports and help, it is not possible for me to finish my experiments. I would like to thank Michael Herz for supporting and help of tracer production and radio analysis techniques. I would like to thank Reinhold Klitfch and Marina Schenk for supporting and help of tracer production.

I really appreciate all the help Dr. Liang Song and Dr. Detian Yuan gave when I was searching for a reliable cell counting method. It is Dr. Song's suggestion that led us to find the best method for assessing cell numbers on a chip with a small population.

I would like to thank Dr. Sabine Schwamberger, Dr. Anne-Kathrin v. Thaden, Susanne Swirczek and Miriam Mohring for helping animal experiments and taking care of the animals. I would like to thank workers from Klinikaustauschraum and ZPF. I would like to thank Dr. Katja Steiger for supporting of pathology check for the stained slides.

I would like to thank for Dr. Ian Somlai and Andreas Seiler for helping fabricate of imaging platform. I would like to thank Dr. Iina Laitinen, Birgit Blechert, Birgit Meißner, Christine Koppenhöhl, Katja Steiger, Sabine Pirsig, Manja Thorwirth for their help and support.

I would like to thank Dr. Armin Bieser (iBidi GmbH) for the support and help all aspects of knowledge about the ibidi chips and Dr. Jan Tous (CRYTUR, spol. s r.o.) for supports related to the positron camera.

I would like to thank Dr. Stefan Stangl, Dr. Christine Bayer for helping of immunofluorescence staining and fluorescence microscopy. I would like to thank Aayush Gupta and Franziska Hanus

for guide of BCA protein assay, and helpful discussion with Dr. Benedikt Feuerecker and Nahid Yusufi.

I would like to thank Sybille Reder, Dr. Christof Seidl, Dr. Franz Schilling for helping me handle some daily lives problem in Germany. I would like to thank Dr. Christof Seidl for many helpful discussions.

I would like to express respects to Sibylle Reder and Michael Herz, they are really diligent colleagues in the Nuclear Medicine. They have done excellent jobs, they take care of every details and people can fully trust the work they do. They showcase the genuine German technician and radiochemist spirits.

I would like to thank the former Consul Jiqiang Dai and Consul Prof. Dr. Chongling Huang from Chinese Consulate-General in Munich. They offered me a lot of help and opportunities during my stay in Germany.

I would like to thank Dr. Katrin Offe and Desislava Zlatanova for their support and help, they did a great job in coordinating our academic activities, and they always answer my questions and solve my problems quickly and sufficiently.

I would like to thank all of my colleagues: Dr. Xiaoyin Cheng, Dr. Qian Wang, Dr. Florian Schneider, Dr. Ian Somlai, Tao Cheng, Ziying Jian, Lina Xu, Sasa Cheng for the discussion and help in both academic and daily life.

I would like to thank all my friends in Germany. Dr. Yu Wang, Dr. Jun Zhao, Dr. Shenghan Wang, Yamin Zhao, Baocai, Yin Li, Dr. Xin Bian, Shaoxia Jin, Jialin Yen, Rong Li, Haifeng Yu, Ying Ouyang, Lei Bao, Simin Hu, Jiachen Shen, Chengxi Lin, Christian Agsteiner, Tobias Rmk Meyer, Fabian Franke, Alex Bazhenov, Beni, Ferdinand Rupp, Hazel Han, Marcos Falcon, Martin Sälzle, Dr. Joachim Pircher, Dr. Maxim Barenboim, Dr. Xiaoyin Cheng, Dr. Qian Wang, Dr. Wentao Song, Dr. Florian Schneider, Dr. Ian Somlai, Tao Cheng, Ziying Jian, Xiaopeng Ma, Lina Xu, Sasa Cheng, Gang Yuan, Dr. Liang Song, Dr. Bo Kong, Prof. Dr. Gang Zhao, Dr. Xiaoling Liang, Dr. Zhoulei Li, Dr. Yuchen Xia, Dr. Xiaoming Cheng, Dr. Yun Zhang, Dr. Lianpan Dai, Dr. Detian Yuan, Dr. Chenyu Zou, Dr. Meng Chun, Dr. Shanshan Luo, Dr. Jingjing Xia, Lunda Gu, Miao Lu, Jiaoyu Ai, Zhifen Chen, Chuan Shan, Huaiyuan Zheng, Juan Liu, Xinyi Dai, Kai Li, Wei Wu, Jing Cao, Shuo Zhao. I can’t imagine six years’ life without you.

I am thankful for China Scholarship Council (CSC) and SFB824 for the support.

Finally the last, I would express my deepest appreciation to my parents, my wife Dr. Limin Yang and my sister. Without your unconditional love, kind understanding and endless support, I can barely finish this study. Thank you all!

Publications and Conferences

Papers:

- **Zhen Liu***, Ziying Jian*, Qian Wang, Tao Cheng, Benedikt Feuerecker, Markus Schwaiger, Sung-Cheng Huang, Sibylle I. Ziegler and Kuangyu Shi. "A Continuously Infused Microfluidic Radioassay System for the Characterization of Cellular Pharmacokinetics." Accepted 08.02.2016 by Journal of Nuclear Medicine. (*: co-first author).
- Qian Wang, **Zhen Liu**, Sibylle I. Ziegler and Kuangyu Shi. "Enhancing Spatial Resolution of 18F Positron Imaging with the Timepix Detector by Classification of Primary Fired Pixels Using Support Vector Machine." Physics in Medicine and Biology 60, no. 13 (2015): 5261.
- Qian Wang, **Zhen Liu**, Sibylle I. Ziegler and Kuangyu Shi. "A Reaction-Diffusion Simulation Model of ^{18}F-FDG Pet Imaging for the Quantitative Interpretation of Tumor Glucose Metabolism." In Computational Methods for Molecular Imaging, edited by Fei Gao, Kuangyu Shi and Shuo Li, 22, 123-137: Springer International Publishing, 2015.
- Xiaoyin Cheng, Zhoulei Li, **Zhen Liu**, Nassir Navab, Sung-Cheng Huang, Ulrich Keller, Sibylle I. Ziegler and Kuangyu Shi. "Direct Parametric Image Reconstruction in Reduced Parameter Space for Rapid Multi-Tracer PET Imaging." IEEE Transactions on Medical Imaging 34, no. 7 (2015): 1498-1512.
- Qian Wang, Jan Tous, **Zhen Liu**, Sibylle I. Ziegler and Kuangyu Shi. "Evaluation of Timepix Silicon Detector for the Detection of 18f Positrons." Journal of Instrumentation 9, no. 05 (2014): C05067.

Conference talks

- **Zhen Liu**, Benedikt Feuerecker, Stephan Düwel, Tao Cheng, Geoffrey Topping, Katja Steiger, Rickmer Braren, Markus Schwaiger, Sibylle Ziegler and Kuangyu Shi. "A Multimodal Intravital Molecular Imaging System Based on Dorsal Skin Window Chamber Tumor Model." Journal of Nuclear Medicine 56, no. supplement 3 (2015): 59.
- **Zhen Liu**, Kuangyu Shi, Wei Sha, Sabine Pirsig, Sung-Cheng Huang, Markus Schwaiger and Sibylle Ziegler. "Factors Influencing Cellular ^{18}F-FDG Kinetics of Tumor Cell Lines as Assessed by a Real-Time Radioassay System." Journal of Nuclear Medicine 53, no. supplement 1 (2012): 9.

Patent:

- Kuangyu Shi, **Zhen Liu**, Sibylle I. Ziegler and Markus Schwaiger. "System and Apparatus for Multimodality-Compatible High-Quality Intravital Radionuclide Imaging." US 20140121493 A1, 2014.